Properties of Weak Values

Mira Weißl

München 2016

Properties of Weak Values

Mira Weißl

Master Thesis
Department of Physics
Ludwig–Maximilians–Universität
München

handed in by
Mira Weißl

Munich, December 21, 2016

Supervisor: Prof. Dr. Harald Weinfurter

Eigenschaften von Weak Values

Mira Weißl

Masterarbeit
Fakultät für Physik
Ludwig–Maximilians–Universität
München

vorgelegt von
Mira Weißl

München, den 21.12.2016

Gutachter: Prof. Dr. Harald Weinfurter

Abstract

The concept of the weak value, introduced in 1988 by Aharonov, Albert and Vaidman [4], has been subject to controversies about its interpretation ever since, despite that it has proven useful for various problems. This thesis aims to shed light on the question about the physical meaning of the weak value. This is accomplished by the comparison with standard quantities as the eigenvalue and the expectation value. In particular the distance between the respective pointer states associated with these quantities, expressed in terms of the respective Bures angle, serves as a criterion for similarity. In [47] we have shown that the Bures angle between the states associated with a weak value and an eigenvalue scales differently than the Bures angle between the states associated an expectation value and an eigenvalue, if the interaction strength between object and pointer system is varied. This indicates a stronger similarity of weak values to eigenvalues, than to expectation values. This comparison is experimentally implemented by an interference experiment which comprises the quantum states under study in the respective interferometer arms. The interaction is modelled by a birefringent element, which couples the observable of the object system, the photon polarization, and the observable of the pointer system, the spatial degree of freedom. In this thesis the interferometer for the experimental realization is set-up and optimized to meet the requirements needed to enable the comparison to the theoretical expressions of the Bures angle. Despite of imperfect experimental conditions the results can resolve the fitted expressions in the available range of interaction strength and the difference in the scaling behaviour is clearly demonstrated. These results are discussed and evaluated in conclusion.

Contents

List of Figures

1 Introduction

One of the peculiar features of quantum mechanics is that a measurement of a physical system usually irrevocably changes its quantum state [38, 24]. It leaves the measured system in an eigenstate of the measured observable, which is independent of the state beforehand. The corresponding eigenvalue is considered to be the outcome of the measurement. Non-ideal or weak measurements represent processes where the standard paradigm of quantum measurement is modified. There the coupling between the quantum system and the measurement device is weak in the sense that only little information about the quantum system can be extracted in a single measurement. Besides having the drawback that many identically prepared systems are needed to precisely extract the expectation value of an observable of the quantum system, one major advantage of weak measurements is that the state of the system is almost left undisturbed by the weak measurement, i.e., it does not 'collapse' into an eigenstate. With the introduction of the so-called weak value in 1988, Aharonov, Albert and Vaidman combined the idea of measuring the quantum system only weakly with the idea of selecting a particular final state [4]. In contrast to classical mechanics, the initial and final boundary conditions of a closed quantum system can be chosen freely, because the initial state does not determine the final one and vice versa. In particular identical measurements on identically prepared systems can yield different results, which follows from the superposition principle.

From the first experiment that implemented the weak value 25 years ago [37] its concept was henceforth fruitfully applied to various fields of research. Its unusual properties provide a novel approach to extract information about a quantum system. A recent experiment implemented the concept to measure the transverse spatial wave function of a single photon in a direct way [29]. Another example concerns the famous double slit experiment, where it was accomplished to determine the average momenta of particles arriving at a given, postselected position and thereby to reconstruct the average propagation of photons through the slit without destroying the interference pattern [23]. Furthermore the weak value is used to address fundamental questions in quantum mechanics, among them the test of the assumption of macroscopic realism [17, 32, 48]. Its most practical application is its use as a metrological technique for its potential in amplifying small signals if certain types of noise are present [28, 11].

Despite the fact that the concept of weak values has proven useful for many purposes, its interpretation is still disputed in the science community. Therefore the research question arises: What is the physical meaning of the weak value? We investigate the quantity from an operational point of view, in how it interacts with other systems, i.e., the measurement device. In particular we are interested in how its behaviour compares with standard quantities as the eigenvalue and the expectation value of an observable of a quantum system.

This is analysed by the comparison of the respective quantum state of the measurement device, henceforth called the pointer system. The pointer state is fundamental to extract information about the properties of the quantum system under study, which is henceforth called the object system. This thesis is concerned with the experimental quantitative analysis of this comparison, which is implemented in an interference experiment. In particular, one arm of the interferometer prepares the object state corresponding to an eigenvalue, while the other one comprises a state, which is described by a weak value, and a modified state, which is described by an expectation value. Our criterion for similarity is the closeness of the respective pointer quantum states, which translates to the ability to interfere. This research is based on the theoretical analysis of the scaling of the distance between the respective states, when the interaction strength between object and pointer system is varied. In [47] we have shown that the distance between the states associated with a weak value and an eigenvalue scales differently as the distance between the states associated with an expectation value and an eigenvalue. This shows a stronger similarity of weak values to eigenvalues, than to expectation values. The interaction is experimentally implemented by a birefringent element, which weakly couples the observable of the object system, in our case the photon polarization, and the observable of the pointer system, realized by the spatial degree of freedom. The strength of interaction is varied by tilting the birefringent crystal, which introduces a spatial separation of the two polarization components of the laser beam. This lowers the coherence of the interfering states, which alters the visibility, which is experimentally obtained by measuring the resulting intensity modulation. The aim is to experimentally determine the scaling behaviour of the visibility in dependence of the interaction strength for both cases of interest. In the course of this thesis the interferometer needed for the comparison of states was set-up and optimized. The results obtained enabled the comparison to the theory and verified the predicted difference in the scaling behaviour.

The thesis is structured in the following way. Chapter 2 explains the basic principles, both regarding the quantum mechanical description of the standard measurement process and the relevant optical processes underlying the experimental realization. Chapter 3 introduces the notion of the weak value, explains its main idea and discusses its properties and associated applications. The underlying theoretical expressions for the Bures angle are presented, followed by the analysis of the conceptual implementation of the comparison. In chapter 4 the experimental set-up is described and the methods applied are illustrated. Furthermore the measurement protocol of the interference experiment and the associated data evaluation is outlined. The main chapter, 5, analyses the requirements for a successful experimental realization and summarizes the measurements performed. The results of the interference experiment are discussed and compared to the theory. A conclusion of this thesis and an outlook is given in the last chapter.

2 Basics

This chapter provides the basic principles for this thesis, both the quantum mechanical description as well as the underlying optical processes.

2.1 Quantum mechanics

Some aspects of the quantum mechanical theory will be summarized briefly by means of a polarization-based model system, which will be further used for the experimental confirmation of the theoretical claim, while a more in-depth discussion can be found in standard textbooks on quantum mechanics. The standard measurement process will be introduced in more detail because it is fundamental for describing the weak value formalism (see chapter 3).

2.1.1 Polarization based model system

The electric field of a photon moving in free space oscillates in the plane perpendicular to the propagation axis, which is illustrated in Fig. 2.1. The polarization state describes the orientation of the electric field oscillations over time. To span this polarization state two orthogonal basis vectors are needed.

In quantum mechanics the physical state of a system is represented by a state vector in a Hilbert space $\mathcal{H}$, which is in general infinite-dimensional and complex. In the case of the polarization degree of freedom the Hilbert space is reduced to two dimensions, i.e., it is spanned by two orthonormal vectors, in Dirac notation $|H\rangle$ and $|V\rangle$, denoting horizontal and vertical polarization states, respectively. Any normalized linear combination of the two basis states constitutes another valid state according to the quantum superposition principle [31]:

$$|\psi\rangle = a|H\rangle + b|V\rangle = a\begin{pmatrix} 1 \\ 0 \end{pmatrix} + b\begin{pmatrix} 0 \\ 1 \end{pmatrix} \tag{2.1}$$

Here a, b are complex numbers, which are called amplitudes. They must satisfy the normalization condition $|a|^2 + |b|^2 = 1$. $|\psi\rangle$ contains the maximal possible information about the physical state. Measurable quantities, so-called observables, correspond to Hermitian operators $\hat{O}$. According to the projection postulate an ideal measurement of $\hat{O}$ on a system in state $|\psi\rangle$ will project the system state onto one of the eigenstates, say $|o_n\rangle$, of that observable and the result will be the corresponding real-valued eigenvalue o_n. In the standard interpretation this is referred to as the postulate of the reduction of the wave function, which is irreversible. The expectation value of $\hat{O}$ with respect to state $|\psi\rangle$ is given by $\langle\psi|\hat{O}|\psi\rangle$.

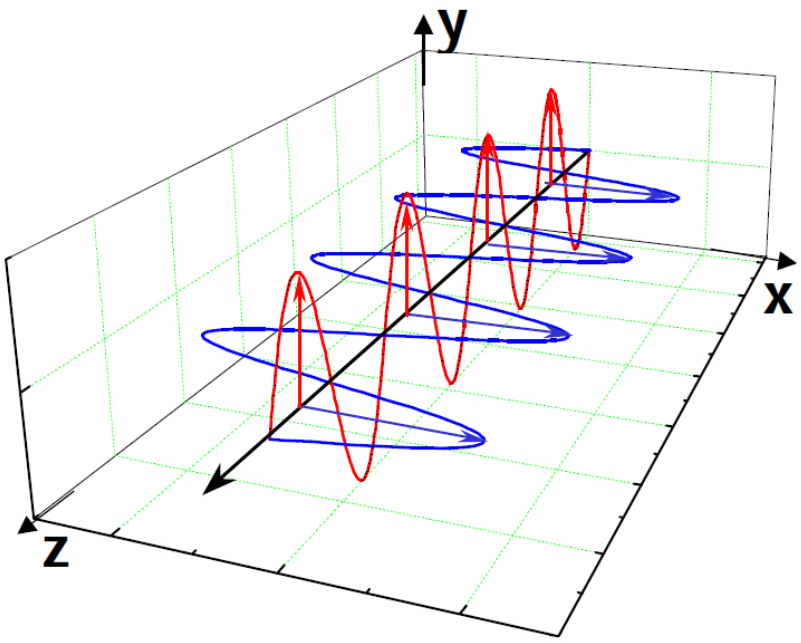

Figure 2.1: Linear polarised light propagating in z direction with the electric field oscillation in blue and the magnetic field oscillation in red from [19].

The probability for some particular eigenstate to occur is $|\langle o_n|\psi\rangle|^2 = \langle\psi|o_n\rangle\langle o_n|\psi\rangle$, with $|o_n\rangle\langle o_n|$ being the projector onto the eigenstate of the observable. In the two-level-system of polarization the eigenvalues of an observable are either +1 or -1 corresponding to the two orthogonal eigenvectors. A visualization of the two-dimensional quantum state is provided by the geometric representation of (2.1). Without any loss of generality it can be rewritten as

$$|\psi\rangle = \cos\left(\frac{\theta}{2}\right)|H\rangle + \mathrm{e}^{i\varphi}\sin\left(\frac{\theta}{2}\right)|V\rangle \tag{2.2}$$

where an irrelevant global phase is omitted and $\theta \in [0,\pi], \varphi \in [0,2\pi]$ are real numbers, which can be identified with the angles of spherical coordinates [31]. Due to the homomorphism of the two-dimensional special unitary group SU(2) to O(3), any $|\psi\rangle \in \mathcal{H}$ uniquely maps to a point with coordinates $(\langle\psi|\hat{\sigma}_x|\psi\rangle,\ \langle\psi|\hat{\sigma}_y|\psi\rangle,\ \langle\psi|\hat{\sigma}_z|\psi\rangle)$ on the surface of the real unit sphere in Euclidean space, the so-called Bloch sphere (see Fig. 2.2), where the Pauli spin matrices are given by

$$\hat{\sigma}_x = \begin{pmatrix} 0 & 1 \\ 1 & 0 \end{pmatrix} \qquad \hat{\sigma}_y = \begin{pmatrix} 0 & -i \\ i & 0 \end{pmatrix} \qquad \hat{\sigma}_z = \begin{pmatrix} 1 & 0 \\ 0 & -1 \end{pmatrix}. \tag{2.3}$$

The polarization vectors $|H\rangle$ and $|V\rangle$ are defined as eigenstates of the $\hat{\sigma}_z$ operator and lie on the upper and lower pole, respectively. On the equator one finds the eigenstates of the $\hat{\sigma}_x$ operator, namely $|P\rangle$ and $|M\rangle$ corresponding to $\pm 45°$ linear polarization, respectively, and the eigenstates of the $\hat{\sigma}_y$ operator, denoted by $|R\rangle$ and $|L\rangle$ for right and left circular

polarization, respectively.

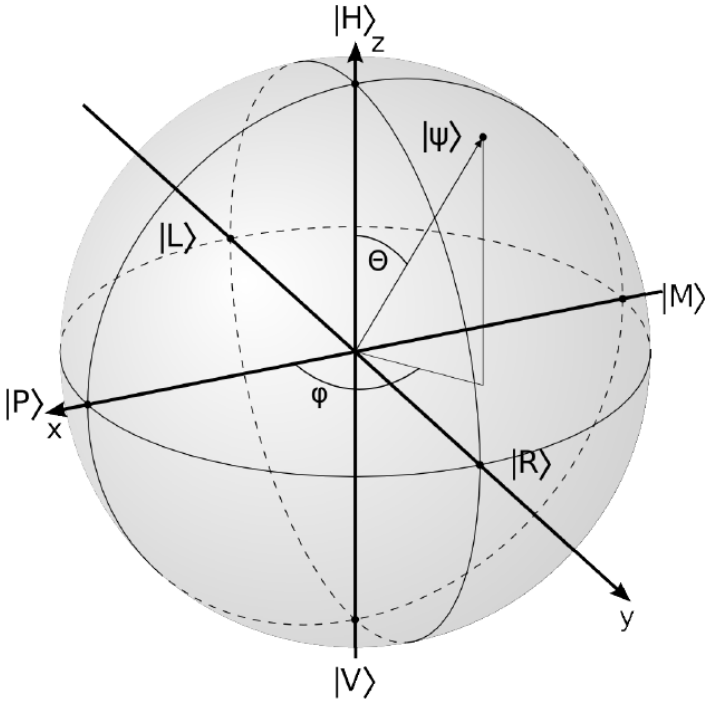

Figure 2.2: Bloch sphere from [12] as visualization of a two-level quantum state, which can be expressed in terms of the eigenstates of the $\hat{\sigma}_z$ operator, $|H\rangle$ and $|V\rangle$, as $|\psi\rangle = \cos\left(\frac{\theta}{2}\right)|H\rangle + \mathrm{e}^{i\varphi}\sin\left(\frac{\theta}{2}\right)|V\rangle$. The eigenstates of the Pauli matrices $\hat{\sigma}_x, \hat{\sigma}_y, \hat{\sigma}_z$ lie on the axes x, y, z respectively. Pure states reside on the surface of the sphere, while mixed states lie within, with the completely incoherent mixture in the center.

$$\hat{\sigma}_z|H/V\rangle = \pm|H/V\rangle \tag{2.4}$$

$$\hat{\sigma}_x|P/M\rangle = \hat{\sigma}_x\left(\frac{1}{\sqrt{2}}(|H\rangle \pm |V\rangle)\right) = \pm|P/M\rangle \tag{2.5}$$

$$\hat{\sigma}_y|R/L\rangle = \hat{\sigma}_y\left(\frac{1}{\sqrt{2}}(|H\rangle \pm i|V\rangle)\right) = \pm|R/L\rangle \tag{2.6}$$

In a two-level system any measurement operator can be built from a combination of the identity operator $\mathbb{I}$ and the three Pauli operators. Not only for the considered polarization model system, but for any two-level quantum mechanical system - also called qubit - the Bloch sphere serves as a geometrical representation of the state space. The points on the surface of the sphere correspond to the pure states of the system (completely

polarized), whereas the interior points correspond to mixed states (partially polarized with the unpolarized state in the center). The latter cannot be written in terms of the bra–ket notation like pure states, but are expressed by means of the density matrix $\hat{\varrho}$, which is capable of describing incoherent mixtures of quantum states. Its diagonal elements denote the probabilities or populations of the respective states, while possible coherence terms are off-diagonal.

2.1.2 Standard measurement process via indirect scheme

In practice the quantum system - in the following referred to as object system - is usually measured indirectly by bringing it into interaction with a measurement device, what results in the so-called pre-measurement. The measurement device, hereafter named pointer system, is then read off, i.e. projectively measured [24], [42]. One way to model such an indirect measurement is based on the scheme by von Neumann, treating both, the object and the pointer system, quantum mechanically, which effectively constitutes a projective measurement of the object system for an ideal interaction. The Hilbert space of the total system is then composed of the direct product $\mathcal{H}_{\text{total}} = \mathcal{H}_{\text{object}} \otimes \mathcal{H}_{\text{pointer}}$. The total Hamiltonian reads $\hat{H}_{\text{total}} = \hat{H}_{\text{object}} + \hat{H}_{\text{pointer}} + \hat{H}_{\text{int}}$, where 'int' is abbreviated for interaction. For simplicity the evolution of the free Hamiltonians of the subsystems $\hat{H}_{\text{object}}, \hat{H}_{\text{pointer}}$ can be neglected, if the interaction time is assumed to be small compared to the internal time evolution of the respective subsystems, i.e. the interaction is instantaneous [26] [42]. Then the object observable under study, say $\hat{A}$, does not change during the measurement, i.e. $[\hat{A}, \hat{H}_{\text{int}}] = 0$ [8].

General description

Let $\hat{A} \in \mathcal{H}_{\text{object}}$ be the observable of interest, having discrete and non-degenerate eigenvalues. We choose some observables $\hat{X}$ and $\hat{M}$ of the pointer's Hilbert space, which do not commute with each other. This means $[\hat{M}, \hat{X}] \neq 0$, which in a given state is associated with the uncertainty relation $\Delta M \Delta X \geq \frac{1}{2}|\langle[\hat{M}, \hat{X}]\rangle|$, where Δ denotes the standard deviation of the respective probability distributions, e.g. $\Delta X = \sqrt{\langle \hat{X}^2 \rangle - \langle \hat{X} \rangle^2}$. $\hat{X}$ acts as the input observable, being involved in the interaction, while $\hat{M}$ is the output observable, which is chosen to be read off thereafter. At time t = 0 the object system is prepared, i.e. preselected, in the pure state $|\psi\rangle = \sum_{i=1}^{d} |a_i\rangle\langle a_i|\psi\rangle = \sum_{i=1}^{d} c_i |a_i\rangle$, which is a superposition of eigenstates of $\hat{A}$ with d being the dimension of $\mathcal{H}_{\text{object}}$, while the initial pointer state is given by $|\phi_0\rangle$, which is a superposition of eigenstates $|m_k\rangle$ of $\hat{M}$.

The two independent subsystems then interact with each other during a small time interval ϵ via a unitary time evolution operator $\hat{U}(\epsilon, 0) = \exp\left(-\frac{i}{\hbar}\int_0^\epsilon \mathrm{d}t\, \hat{H}_{int}\right)$, where the integral may be substituted by $\epsilon \hat{H}_{int}$ since the impulsive interaction Hamiltonian is time

independent. It is given by

$$\hat{H}_{int} = g\hat{A} \otimes \hat{X}, \tag{2.7}$$

with the real-valued interaction constant g. The joint initial state of the total system, namely the uncorrelated product state $|\tau_0\rangle$, is transformed by $\hat{U}$ according to [42]

$$\begin{aligned} |\tau_0\rangle := |\psi\rangle \otimes |\phi_0\rangle \xrightarrow{\hat{U}} \hat{U}\left(|\psi\rangle \otimes |\phi_0\rangle\right) &= \mathrm{e}^{-\frac{i\epsilon g}{\hbar}\hat{A}\otimes\hat{X}} \left(\sum_{i=1}^{d} c_i |a_i\rangle \otimes |\phi_0\rangle\right) \\ &= \sum_{i=1}^{d} c_i |a_i\rangle \otimes \mathrm{e}^{-\frac{i\epsilon g}{\hbar}a_i\hat{X}} |\phi_0\rangle =: \sum_{i=1}^{d} c_i |a_i\rangle \otimes |\phi_i\rangle =: |\tau\rangle, \end{aligned} \tag{2.8}$$

which constitutes the so-called pre-measurement, illustrated in Fig. 2.3. Here $|\phi_i\rangle = \mathrm{e}^{-\frac{i\epsilon g}{\hbar}a_i\hat{X}} |\phi_0\rangle$ denote the pointer states, correlated to the system. As a consequence the object and the pointer system are in an entangled state, i.e. they cannot be written as a product state of two single states.

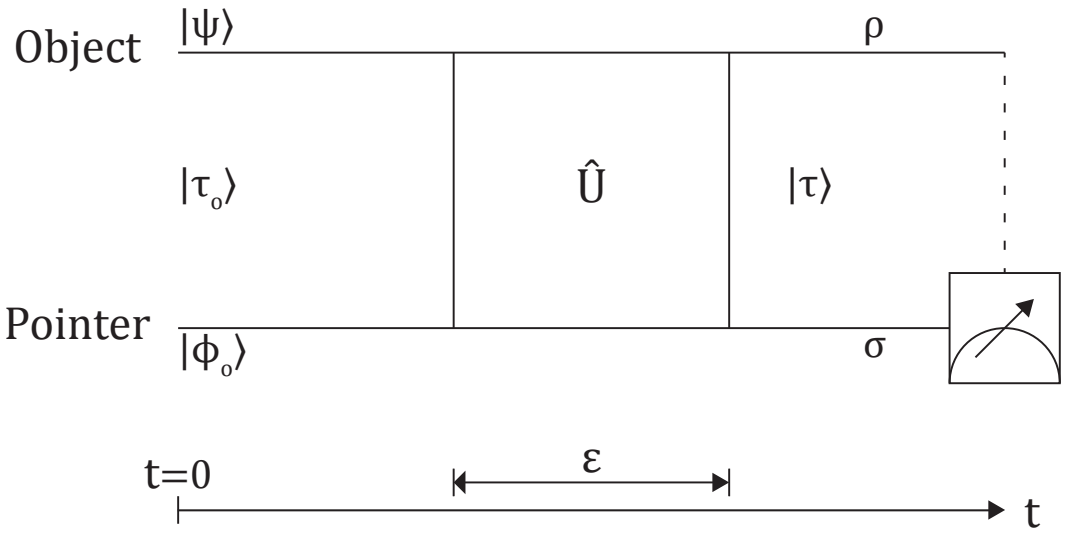

Figure 2.3: Standard measurement process in the indirect scheme. The object system couples to a pointer system via a unitary interaction $\hat{U}$, which lasts a small time interval ϵ. Thereby the product state $|\tau_0\rangle$ is transformed to the entangled state $|\tau\rangle$, which means the systems are correlated. The pointer can then be read off to extract information about the object observable.

In particular, each object state $|a_i\rangle$ is correlated with a corresponding pointer state $|\phi_i\rangle$, which is in general not an eigenstate of the pointer operator $\hat{M}$, but a superposition of those. The states $|\phi_i\rangle$ are normalized, but in general they do not form a complete set in $\mathcal{H}_{\text{pointer}}$. The pointer system is now superposed proportional to the object system [9]. By taking the partial trace of the total density matrix over the non-interesting degrees of freedom, one

can obtain an expression for the state of each of the systems. The corresponding density matrix of the joint state $|\tau\rangle$ reads [42]

$$\hat{\tau} = |\tau\rangle\langle\tau| = \sum_{i,j} \left(|a_i\rangle \otimes |\phi_i\rangle\langle a_i|\psi\rangle\langle\psi|a_j\rangle\langle a_j| \otimes \langle\phi_j|\right) = \sum_{i,j} \left(\hat{\Lambda}_{a_i}|\psi\rangle\langle\psi|\hat{\Lambda}_{a_j}|\phi_i\rangle\langle\phi_j|\right) \tag{2.9}$$

with the abbreviation $\hat{\Lambda}_{a_i} = |a_i\rangle\langle a_i|$. From this the separate density matrix of the object system $\hat{\varrho}$ is computed by summing over the pointer's basis states [42]:

$$\hat{\varrho} = \mathrm{Tr}_{\mathrm{pointer}}[\hat{\tau}] = \sum_k \langle m_k|\hat{\tau}|m_k\rangle = \sum_{k,i,j} \langle m_k|\phi_i\rangle\hat{\Lambda}_{a_i}|\psi\rangle\langle\psi|\hat{\Lambda}_{a_j}\langle\phi_j|m_k\rangle = \sum_{i,j} \hat{\Lambda}_{a_i}|\psi\rangle\langle\psi|\hat{\Lambda}_{a_j}\langle\phi_j|\phi_i\rangle \tag{2.10}$$

Thus, the system density matrix depends on a possible overlap of the pointer states $\langle\phi_j|\phi_i\rangle$, which is the crucial element in the distinction of ideal and so-called weak measurements, which is to be defined below.
The pointer density matrix is given by [42]

$$\hat{\sigma} = \mathrm{Tr}_{\mathrm{object}}[\hat{\tau}] = \sum_i \langle a_i|\hat{\tau}|a_i\rangle = \sum_i |\phi_i\rangle\langle a_i|\psi\rangle\langle\psi|a_i\rangle\langle\phi_i| = \sum_i |c_i|^2|\phi_i\rangle\langle\phi_i|$$
$$\text{with matrix elements} \quad \langle m_k|\hat{\sigma}|m_l\rangle = \sum_i \langle m_k|\phi_i\rangle|c_i|^2\langle\phi_i|m_l\rangle \tag{2.11}$$

The readout is then performed by a projective measurement of $\hat{M}$ via the projector $\hat{\Lambda}_{m_k} = |m_k\rangle\langle m_k|$ on the pointer system only, which yields an eigenvalue m_k with probability $\mathrm{prob}(m_k) = \mathrm{Tr}\left[(\hat{I}_{\mathcal{S}} \otimes \hat{\Lambda}_{m_k})\hat{\tau}\right] = \sum_i \left(|\langle\phi_i|m_k\rangle|^2 \, |\langle\psi|a_i\rangle|^2\right)$ [42]. The probability distributions of a_i and m_k will only be correlated uniquely if all pointer wave functions $|\phi_i\rangle$ do not overlap. According to the Heisenberg equations of motion the time-dependence of the expectation value of $\hat{M}$ is given by [8]

$$\frac{d\hat{M}}{dt} = \tfrac{i}{\hbar}\epsilon g\hat{A}[\hat{X}, \hat{M}]. \tag{2.12}$$

Integrating and taking the expectation value of both sides of the equation yields

$$\langle\hat{M}\rangle - \langle\hat{M}\rangle_0 = \tfrac{i}{\hbar}\epsilon g\langle\hat{A}\rangle\langle[\hat{X}, \hat{M}]\rangle_0, \tag{2.13}$$

where the subscript 0 always denotes the initial state $|\phi_0\rangle$. As can be seen, the shift in the expectation value of the output observable reveals the expectation value of $\hat{A}$ in linear dependence of ϵg. The outcome is real because the average value of a commutator of two Hermitian operators must be imaginary [34], [18]. The pointer system can indeed be seen as a measurement device for the observable $\hat{A}$ because the probability distribution of the pointer observable $\hat{M}$ evolves proportional to the expectation value of $\hat{A}$. Due to the entanglement, this local measurement on the pointer system will also influence the object state. The back-action on its state again depends on the possible overlap of different $\phi_i(m_k)$s [42].

After projecting the pointer system onto $|m_k\rangle$ the composite state becomes un-entangled

and reads [42]

$$|\tau(|m_k\rangle) = \frac{\sum_i c_i \langle m_k|\phi_i\rangle|a_i\rangle}{\sqrt{\text{prob}(m_k)}} \otimes |m_k\rangle \tag{2.14}$$

This can also be understood in terms of the measurement operator $\hat{\Omega}_k = \sum_i \langle m_k|\phi_i\rangle \hat{\Lambda}_{a_i}$, defined in the Hilbert space $\mathcal{H}_{\text{object}}$, acting on the object state $|\psi\rangle$. Thereby the joint state can be rewritten as

$$|\tau(|m_k\rangle) = \frac{\hat{\Omega}_k|\psi\rangle}{\sqrt{\langle\psi|\hat{\Omega}_k^\dagger\hat{\Omega}_k|\psi\rangle}} \otimes |m_k\rangle \tag{2.15}$$

where the product $\hat{\Omega}_k^\dagger\hat{\Omega}_k$ is referred to as an element of a so-called positive-operator valued measure. These operators are capable of modelling generalized measurements, involving both unitary and non-unitary parts [50]. However, the further description will consider the operations used above.

Canonically conjugate pointer observables

The observables of the pointer's Hilbert space are often chosen to be canonically conjugate, such as the operators of position $\hat{Q}$ and momentum $\hat{P}$, which have continuous spectra. We will consider one-dimensional free motion and position of particles, such as photons in a laser beam, where the commutation relation reads $[\hat{Q}, \hat{P}] = i\hbar$. $\hat{P}$ replaces $\hat{X}$ in the interaction Hamiltonian and $\hat{M}$ is substituted by $\hat{Q}$, which we can identify with the position of a pointer on a measurement device, indicating the measurement outcome on a scale [8]. Likewise $|m_k\rangle$ is substituted by $|q\rangle$, therewith the initial pointer state can be expanded as [42]

$$|\phi_0\rangle := \int \mathrm{dq}\, |q\rangle\langle q|\phi_0\rangle = \int \mathrm{dq}\, |q\rangle\phi_0(q) \qquad \text{with} \qquad \phi_0(q) = \left(\frac{1}{\sqrt{2\pi\sigma_q^2}}\, \mathrm{e}^{-\frac{q^2}{2\sigma_q^2}}\right)^{\frac{1}{2}}, \tag{2.16}$$

for simplicity chosen to be a real-valued wave function Its probability density $|\phi_0(q)|^2$ is a Gaussian distribution centred around 0 with the standard deviation σ_q. For this specific choice of wave function σ_q coincides with the standard deviation of the position operator ΔQ. According to the uncertainty relation, which is minimal for Gaussian wave packets, the momentum operator has a standard deviation of $\Delta P = \frac{\hbar}{2\Delta Q}$, equal to the standard deviation σ_p of its Gaussian probability density $|\phi_0(p)|^2$. The entangled state after the unitary transformation from Eq. (2.8) can be rewritten as [42]

$$\begin{aligned} |\tau\rangle &= \mathrm{e}^{-\frac{i\epsilon g}{\hbar}\hat{A}\otimes\hat{P}} \int \mathrm{dq} \sum_{i=1}^{d} c_i|a_i\rangle \otimes \phi_0(q)|q\rangle = \int \mathrm{dq} \sum_{i=1}^{d} c_i\, \mathrm{e}^{-\frac{i\epsilon g}{\hbar}a_i\hat{P}}\, |a_i\rangle \otimes \phi_0(q)|q\rangle \\ &= \int \mathrm{dq} \sum_{i=1}^{d} c_i|a_i\rangle \otimes \phi_0(q - \epsilon g a_i)|q\rangle = \int \mathrm{dq} \sum_{i=1}^{d} c_i|a_i\rangle \otimes \phi_i(q)|q\rangle. \end{aligned} \tag{2.17}$$

where $\phi_i(q) = \left(\frac{1}{\sqrt{2\pi\sigma_q^2}}\,\mathrm{e}^{-\frac{(q-\epsilon g a_i)^2}{2\sigma_q^2}}\right)^{\frac{1}{2}}$ are the correlated pointer states, corresponding to different a_i. The last step in the Eq. (2.17) comes about because $\hat{P}$ generates translations in the complementary $\hat{Q}$ space. The corresponding probability density of q is

$$\mathrm{prob}(q) = \frac{1}{\sqrt{2\pi(\Delta Q_0)^2}} \sum_{i=1}^{d} |c_i|^2\, \mathrm{e}^{-\frac{(q-\epsilon g a_i)^2}{2(\Delta Q_0)^2}} \tag{2.18}$$

which is a superposition of d Gaussian distributions. Its expectation value in state $\hat{\sigma}$ is given by [42]

$$\langle \hat{Q} \rangle = \int \mathrm{d}q\, q\, \mathrm{prob}(q) = \langle \hat{Q} \rangle_0 + \epsilon g \langle \hat{A} \rangle \tag{2.19}$$

As a consequence of the pre-measurement it is shifted by $\epsilon g \langle \hat{A} \rangle$ with respect to the initial one, which - although assumed zero in our case - appears in the equation for the sake of completeness. Therefore, a measurement of $\hat{Q}$ on the pointer system via some projector $|q\rangle\langle q|$ will reveal information about the system observable $\hat{A}$. The variance of the position operator in this state is given by [42]

$$\begin{aligned} \mathrm{Var}(\hat{Q}) = (\Delta Q)^2 &= \langle \hat{Q}^2 \rangle - \langle \hat{Q} \rangle^2 = \langle \hat{Q}^2 \rangle_0 - \langle \hat{Q} \rangle_0^2 + \epsilon^2 g^2 \left(\langle \hat{A}^2 \rangle - \langle \hat{A} \rangle^2 \right) \\ &= \mathrm{Var}(\hat{Q})_0 + \epsilon^2 g^2\, \mathrm{Var}(\hat{A}) = (\Delta Q_0)^2 + \epsilon^2 g^2 (\Delta A)^2, \end{aligned} \tag{2.20}$$

where the spread is quadratically dependent on ϵg. These results are exact and hold for arbitrary values of ϵg and ΔQ_0. Note, that the corresponding quantities for the momentum operator stay unchanged by this standard measurement scheme.

Ideal setting

An ideal measurement of $\hat{A}$ is considered projective and complete, in the sense that the state before and after the measurement are independent from each other. To be resembled by the indirect measurement scheme via a pointer system the pointer states ϕ_i should be mutually orthogonal in $\mathcal{H}_{\mathrm{pointer}}$, i.e., $\langle \phi_i | \phi_j \rangle \to 0$ for $i \neq j$ with $i, j \in [1, d]$, which implies that the dimension of the pointer system has to fulfil $d_{\mathrm{pointer}} \geq d$. In this case the pre-measurement assigns every basis state $|a_i\rangle$ of the object superposition state, corresponding to a non-degenerate eigenvalue of $\hat{A}$, in a unique way to a pointer state $|\phi_i\rangle$ [42]. As can be seen from Eq. (2.10) the object's density matrix $\hat{\varrho}$ then has diagonal elements only, which signifies a completely incoherent, i.e., mixed superposition state. Because there is no overlap between different pointer wave functions $\phi_i\rangle$, the associated probability distribution contains spatially separated peaks corresponding to the eigenvalues of the observable $\hat{A}$. Due to this one-to-one correspondence of the distributions the probability to obtain an eigenvalue a_i is therefore only dependent on the initial object state $|\psi\rangle$, in particular $|c_i|^2$,

which requires the following relation to be fulfilled [24]:

$$\frac{\epsilon|g|}{\hbar}\delta a \Delta X_0 \gg 1 \tag{2.21}$$

with δa being the minimal distance between the different eigenvalues a_i. This means that the coupling is sufficiently strong and that the initial pointer uncertainty in $\hat{X}$ space is large. Only then the pre-measurement can distinguish between separate eigenvalues a_i. Under these conditions the indirect measurement has the same consequences for the object system as an ideal projective measurement, i.e., the object system will 'collapse' into one of its eigenstates [42]. To obtain the resulting expectation value the outcomes a_i of many measurements, i.e. measurements on many identically prepared object-pointer systems are averaged [18]. This case is also referred to as strong measurement to distinguish it from the non-ideal and in particular weak ones.

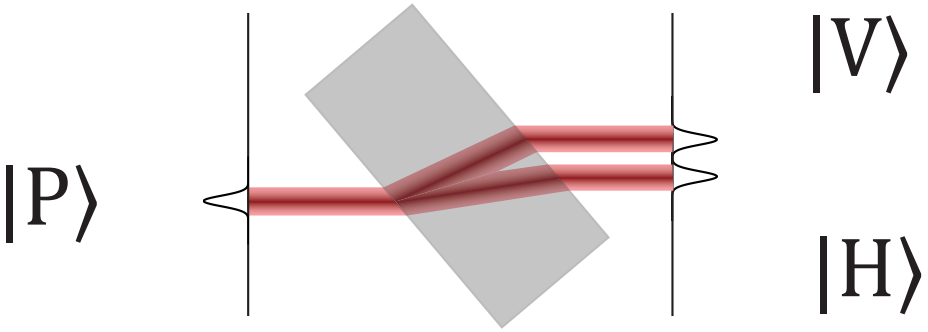

Figure 2.4: Schematic illustration of a realization of an ideal measurement in the indirect scheme. A birefringent element couples the object observable, here the $\hat{\sigma}_z$ operator, to the momentum of the pointer system. The deflection is different for each polarization component, $|H\rangle$ and $|V\rangle$, which results in a spatial separation between them. As a consequence of this interaction the polarization is correlated with the spatial degree of freedom.

Example a) If $\hat{A}$ is represented by $\hat{\sigma}_z$ with $|\psi\rangle$ is given by Eq. (2.1), the entangled state reads [42]

$$|\tau\rangle = \int \mathrm{dq}\,[a|H\rangle \otimes \phi(q - \epsilon g) + b|V\rangle \otimes \phi(q + \epsilon g)]\,|q\rangle \tag{2.22}$$

The expectation value of $\hat{Q}$ in this state is given by $\langle\hat{Q}\rangle = \epsilon g\,(|a|^2 - |b|^2)$. Fig. 2.4 schematically illustrates an experimental realization of an ideal measurement with $a = b = \frac{1}{\sqrt{2}}$, i.e. the preselected state is $|P\rangle$.

Weak setting

In general the pointer states are not mutually orthogonal, which means that condition 2.21 is not fulfilled and the indirect measurement will not result in an ideal projective, strong measurement of the object observable $\hat{A}$. By contrast, weak measurements, as the name indicates, do not merely avoid collapsing the object state, but rather disturb the object system as little as possible. The condition for a non-ideal measurement to be weak can be formulated as

$$\frac{\epsilon|g|}{\hbar}\Delta A\Delta X_0 \ll 1. \tag{2.23}$$

, In this case, the coupling strength together with the initial standard deviation of the pointer position is required to be very small, with reference to the spacing of the eigenvalues of $\hat{A}$. Under these conditions a Taylor series expansion of the unitary transformation, in the following approximated to terms of second order, is valid [42]:

$$\hat{U} = \mathrm{e}^{-\frac{i}{\hbar}\epsilon g\hat{A}\otimes\hat{X}} \approx \mathbb{I} - \frac{i\epsilon g}{\hbar}\hat{A}\otimes\hat{X} - \frac{\epsilon^2 g^2}{2\hbar^2}(\hat{A}\otimes\hat{X})^2 \tag{2.24}$$

The approximation makes sense when the initial pointer wave function in $\hat{X}$ space vanishes sufficiently fast for large values. Together with the simplifying assumption that $\langle\hat{X}\rangle_0 = 0$ the overlap of the different, evolved pointer states in this limit is given by [42]

$$\langle\phi_i|\phi_j\rangle \approx 1 - \frac{\epsilon^2 g^2}{2\hbar^2}\langle\hat{X}^2\rangle_0(a_i - a_j)^2 \tag{2.25}$$

which means, there is almost total overlap. Consequently the correlations between object and pointer states are not in one-to-one correspondence. This means that the dimension of the pointer system d_{pointer} does not have to be greater than the one of the object system d, in particular it can be smaller. This can be exploited by choosing a pointer with simple structure, i.e., with few dimensional degrees of freedom to measure and is especially useful for obtaining the mean value of the probability distribution of an object system with unbounded spectrum of eigenvalues [35]. Inserting Eq. (2.25) into the object's density matrix in Eq. (2.10) underlines that its elements change only very little by the weak unitary interaction with the pointer system, to be exact on the order of $\mathcal{O}(\epsilon^2 g^2)$, meaning that the coherence of the state is largely maintained. Although the shift in $\langle\hat{M}\rangle$ on the order of $\mathcal{O}(\epsilon g)$ is formally the same as for the ideal case, under weak conditions it is much smaller than the uncertainty of $\hat{M}$ and, thereby, not resolvable by a single measurement. Moreover, with the off-diagonal elements of the object's density matrix, that give rise to interference effects, the profile of the probability distribution of $\hat{M}$ changes compared to the strong case.

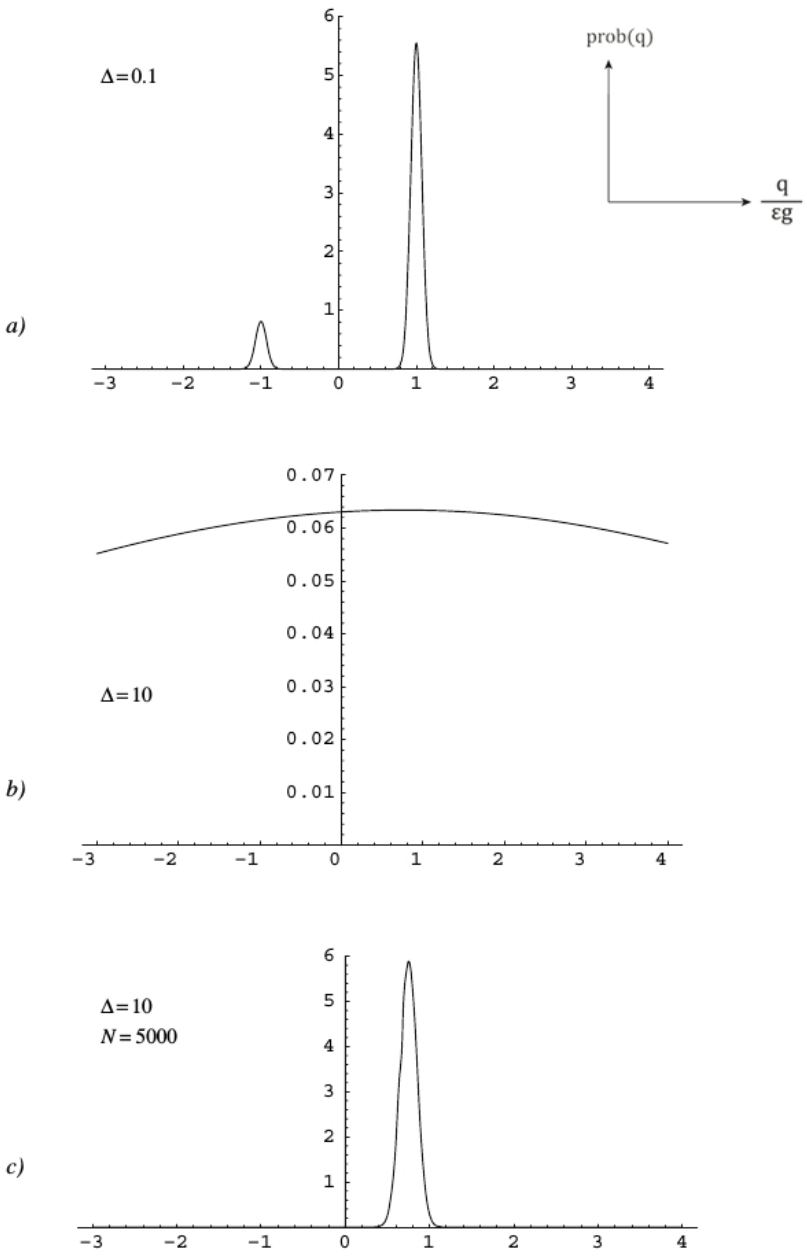

Figure 2.5: Shown is the probability distribution for a strong and a weak measurement. *a*) The former manifests itself in distinct peaks at the eigenvalues ± 1 of the observable, if the axis is scaled appropriately. The standard deviation in this case is $\Delta = 0.1$, which is parametrized as $\Delta = \sqrt{2}\Delta Q_0$. *b*) Distribution resulting from a weak interaction, where the standard deviation given here is 10. *c*) It is reduced to $10/\sqrt{5000} \approx 0.14$ with an ensemble of $N = 5000$ particles. Figure modified from [10].

This can be seen by expanding the exponential factor to first order in the explicit expression of Eq. (2.18), where the interaction caused a superposition of position shifts. Although $\hat{P}$ has an unbounded spectrum, the approximation makes sense, provided $\phi(p)$ vanishes fast enough for large values of p, which is fulfilled by a Gaussian wave function. If we take into account Eq. (2.23), which implies that $\epsilon|g|\Delta A \ll \Delta Q_0$, then [43]

$$\text{prob}(q) \approx \frac{1}{\sqrt{2\pi(\Delta Q_0)^2}} \sum_{i=1}^{d} |c_i|^2 \left(1 - \frac{(q-\epsilon g a_i)^2}{2(\Delta Q_0)^2}\right) \approx \frac{1}{\sqrt{2\pi(\Delta Q_0)^2}} \, \mathrm{e}^{-\frac{\left(q-\epsilon g\langle\hat{A}\rangle\right)^2}{2(\Delta Q_0)^2}} \tag{2.26}$$

which means the superposition of substantially overlapping Gaussians may be approximated by a single Gaussian centred around $\epsilon g\langle\hat{A}\rangle$. This corresponds to the initial wave function, shifted by this value, namely:

$$\phi_0(q) \to \phi_1(q) \approx \phi_0(q - \epsilon g\langle\hat{A}\rangle). \tag{2.27}$$

A certain outcome of a single measurement on one object-pointer system, i.e. particle, provides almost no information because one does not know if the deviation of the outcome from the initial expectation value is due to its original standard deviation ΔQ_0 or due to the shift according to the spectral distribution of eigenvalues of $\hat{A}$. If, however, a large number N of identically prepared object-pointer systems is used, the overall standard deviation reduces according to $\frac{\Delta Q_0}{\sqrt{N}}$ so that the expectation value may be obtained by statistical averaging to an accuracy of $\mathcal{O}(\frac{1}{\sqrt{N}})$ [10], [45].

Example b) This can be seen by means of the example in Fig. 2.5, which shows the probability distribution in $\hat{Q}$ space for $\hat{A} = \frac{1}{\sqrt{2}}(\hat{\sigma}_x + \hat{\sigma}_z)$ and $|\psi\rangle = |P\rangle$, i.e. plus-polarised. The eigenvalues of this operator take the values ± 1. In the strong case *a*) there are two distinct peaks at the locations of the respective eigenvalue, where the positive eigenstate is more probable. When the interaction is weak, which is accomplished here by an increased ΔQ_0, the distribution is located at the expectation value $\frac{1}{\sqrt{2}}\langle P|\hat{\sigma}_x + \hat{\sigma}_z|P\rangle = \frac{1}{\sqrt{2}}$ in case *b*). However the shift is not resolvable from the background, unless a high amount of object-pointer systems is used as in *c*) [10].

2.2 Optics

This section addresses the optical processes which are employed in the realization of the experiment. For a comprehensive description of photonic system it is referred to standard optic textbooks [39, 30].

2.2.1 Laser operating principle

The operation principle of a laser, which is the acronym for 'light amplification by stimulated emission of radiation', are shortly reviewed. A laser is essentially composed of an optical resonator containing an optical amplifier, i.e. an active medium [39]. For operation a third component is needed, as can be seen in Fig. 2.6: an energy source sufficiently excites the active medium via a pumping mechanism over a certain threshold value, such that there arises a population inversion in the energy level system of the active medium. Spontaneous decays into the lower energy level produce incoherent photons emitting in all directions, which is called spontaneous emission. The mirrors of the resonator selectively reflect photons back into the active medium, what is referred to as positive feedback [30]. These may then primarily stimulate directed emission of secondary photons resulting in an amplification of radiation along the resonator. The stimulated energy transitions above the lasing threshold result in the gain spectrum of the medium, whose maximum defines the central wavelength of the laser [30]. The amplification combined with the positive feedback results in coherent oscillation, which is partly outcoupled through one of the mirrors of the resonator [39]. Under steady-state conditions, where the gain equals the losses in the system, the population difference saturates and the photon flux grows linearly with the pumping rate [39].

The oscillation between the reflecting mirrors manifests itself via transverse and longitudinal resonant modes, with characteristic mode numbers. The longitudinal distribution of the electric field forms standing waves, determined by the geometry and the reflectivity of the mirrors [30]. The free spectral range, i.e., the distance between adjacent resonator modes becomes [39]

$$\Delta\nu_{FSR} = \frac{c}{2l} \tag{2.28}$$

where l is the optical length of the resonator. Longitudinal modes are defined by the same optical path length within the resonator, but differ from each other in their wavelength resulting from different numbers of nodes n [1]. Only those within the gain spectrum of the medium may oscillate. As the medium's spectral bandwidth is much broader than the mode spacing, multiple modes may compete for oscillation.

The transversal distribution of the electric field arises from diffraction due to the finite lateral size of the resonator [1]. Depending on the geometry of the resonator the characteristic distributions are described by different Laguerre-Gaussian modes (cylindrical symmetry characterized by radial and angular node numbers) or different Hermite-Gaussian modes (rectangular symmetry characterized by horizontal and vertical node numbers). As different transverse modes exhibit slightly different effective path lengths inside the resonator,

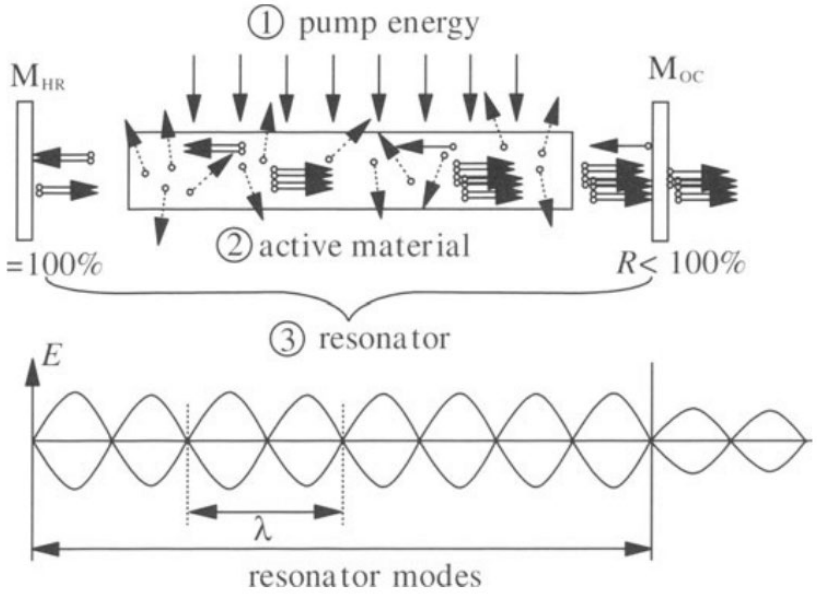

Figure 2.6: Laser components from [30]. An amplifying material placed inside an optical resonator builds up an optical oscillator, when supplied with a pumping energy source. Light is reflected back and forth between the mirrors, where one is highly reflecting, denoted by M_{HR} in the figure, while the other one is less reflective and therefore used for out-coupling the beam, denoted by M_{OC}. Beneath there is a schematic of the longitudinal distribution of the electric field forming standing waves.

they also slightly differ in their associated longitudinal modes [1]. In the following we will be concerned with the fundamental transverse mode TEM_{00}, namely the transverse electromagnetic mode where both node numbers are zero, which results in a Gaussian distribution.

2.2.2 Diode laser with external optical resonator

In the following we restrain the discussion to compact semiconductor lasers, i.e. diode lasers, where the pumping is conducted by means of electric current. A typical model is depicted in Fig. 2.7.

There the gain medium comprises a highly doped p-n-junction at which recombination processes of electrons and holes spontaneously emit photons [30]. The current, at which the minimum population difference of electron hole pairs is achieved, such that the stimulated emission of photons becomes the dominant process is called the threshold current to initiate lasing. The confinement of charge carriers and photons to the active or junction plane may be achieved by an index-guided structure, involving different refractive indices [39]. The spatial confinement selects a single, i.e. the fundamental transverse mode of oscillation.

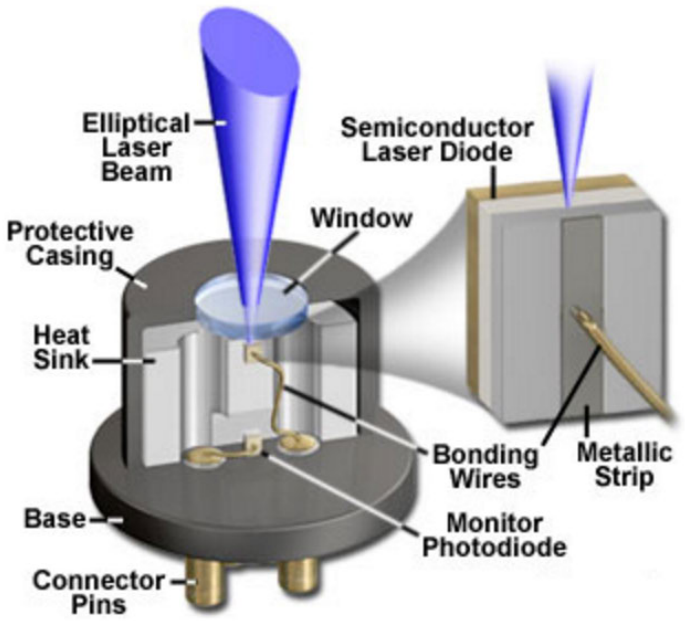

Figure 2.7: Diode laser from [41] showing the typical structure involving components such as the semiconductor diode, which is connected to wires, encompassed by a heat sink inside a casing.

The back and the front facets of the laser diode serve as mirrors.

Longitudinal mode selection

Even if the laser operates in a single Gaussian transverse mode, it may still oscillate on multiple longitudinal modes. To select a single longitudinal mode an external dispersive element, e.g. a diffraction grating, is placed in the path of the output beam. The multi-frequent beam is diffracted according to its wavelengths. In the Littrow configuration, which is shown in Fig. 2.8, the first diffraction order is fed back into the laser diode, while the zeroth order is coupled out as the actual beam. Then the external resonator dominates the feedback over the internal one of the laser diode. According to Eq. (2.28) a longer resonator length means a shorter free spectral range, what may cause mode hops. If, however, the grating is well aligned such that primarily only one frequency is fed back, the laser oscillates in a single longitudinal mode. Additionally its spectral linewidth decreases with the square of increasing external resonator length and therefore its coherence increases [40].

The various spectra involved to select a longitudinal mode are shown in Fig. 2.9. The net amplification for a selected mode arises from the semiconductor gain, the diffraction dispersion as well as the internal and external cavity interference [27]. In this way the wavelength of the output beam may be selected and tuned across the gain profile of the

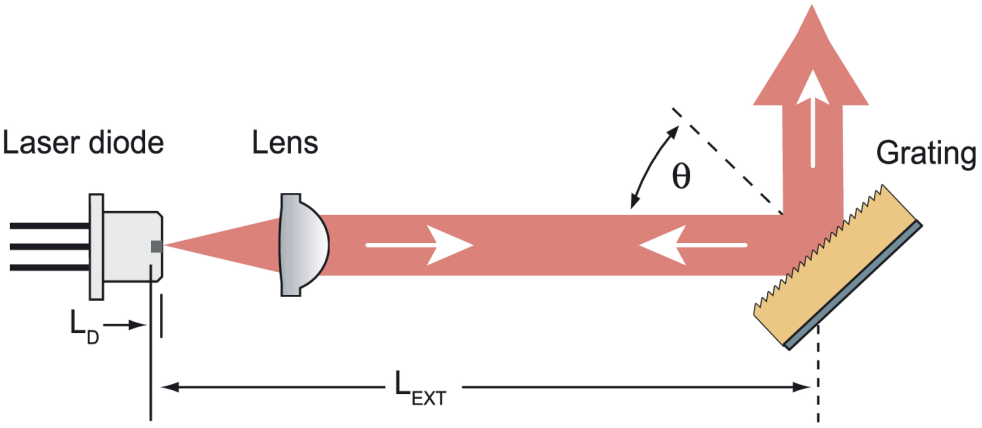

Figure 2.8: External optical resonator in the Littrow configuration from [40]. The laser beam is outcoupled from the laser diode and reaches the diffraction grating after passes a lens. The first diffraction order is coupled back into the laser diode, such that the feedback from the external resonator, whose length is denoted by L_{EXT} in the figure, dominates over the feedback from the internal diode resonator, whose length is given here as L_D. The zeroth diffraction order is used as the actual beam.

semiconductor material.

2.2.3 Beam characteristics

One of the most important characteristics of the output laser beam is its coherence, which is the basis of interference effects.

Spatial coherence

The highest spatial coherence is achieved for the fundamental transverse mode (TEM_{00}) providing the highest beam quality. This involves in particular the focus and collimation properties of the beam, where the beam exhibits only low divergence. The electric field amplitude of a Gaussian beam travelling in z-direction takes the form

$$E(x,y,z) = A(x,y,z)\,\mathrm{e}^{-ikz} = \frac{A_1}{q(z)}\,\mathrm{e}^{-ik\frac{r^2}{2q(z)}}\,\mathrm{e}^{-ikz} \tag{2.29}$$

The complex envelope $A(x,y,z)$ satisfies the slowly varying envelope approximation of the wave equation [39]. That is, $A(x,y,z)$ changes much slower in z direction than it does in x and y direction, where $r^2 = x^2 + y^2$. Here A_1 is a constant and $q(z)$ denotes the complex

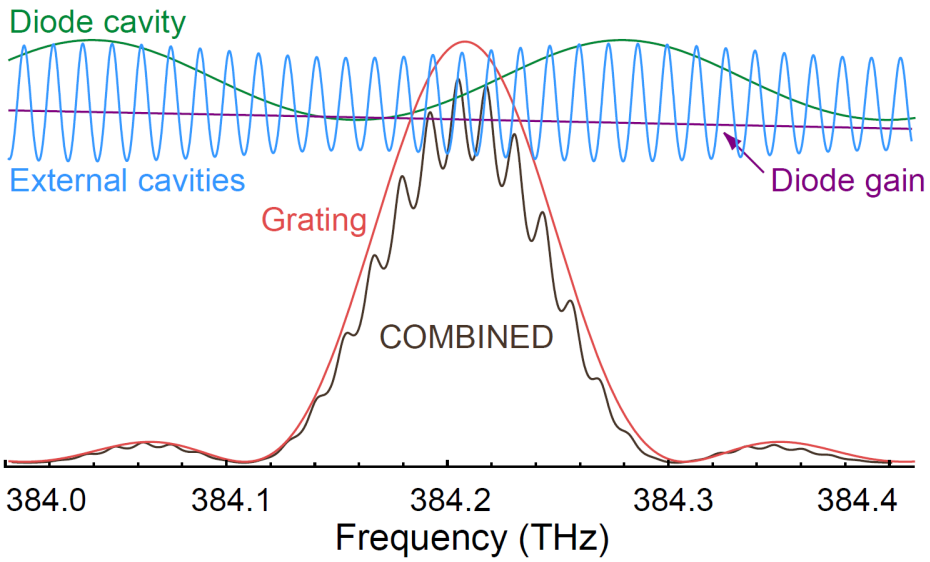

Figure 2.9: Shown are the various frequency-selective elements of a diode laser at a central wavelength of 780 nm: semiconductor diode gain, the diffraction grating, the internal and external resonator, which is called cavity here. The combined gain resulting from those factors defines the selected longitudinal mode. The figure represents a misaligned external resonator because two external cavity modes are similarly amplified, which will cause multi-mode operation. Figure from [27]

q-parameter, whose inverse comprises amplitude and phase parts according to:

$$\frac{1}{q(z)} = (z + iz_0)^{-1} = \frac{1}{R(z)} - i\frac{\lambda}{\pi W^2(z)} \tag{2.30}$$

$R(z)$ denotes the wave front radius of curvature. The definition of the other two parameters refer to the respective intensity distribution $I = |E(x, y, z)|^2$: The beam width, which is dependent on the z direction, is called $W(z)$, where W_0 is the waist radius. The Rayleigh length z_0 indicates the distance from the beam waist position over which the waist diameter $2W_0$ has diverged by a factor of $\sqrt{2}$, as shown in Fig. 2.10. The quantities are defined as

$$R(z) = z\left(1 + \frac{z_0^2}{z^2}\right), \tag{2.31}$$

$$W(z) = W_0\sqrt{1 + \frac{z^2}{z_0^2}}, \tag{2.32}$$

$$z_0 = \frac{\pi {W_0}^2}{\lambda}. \tag{2.33}$$

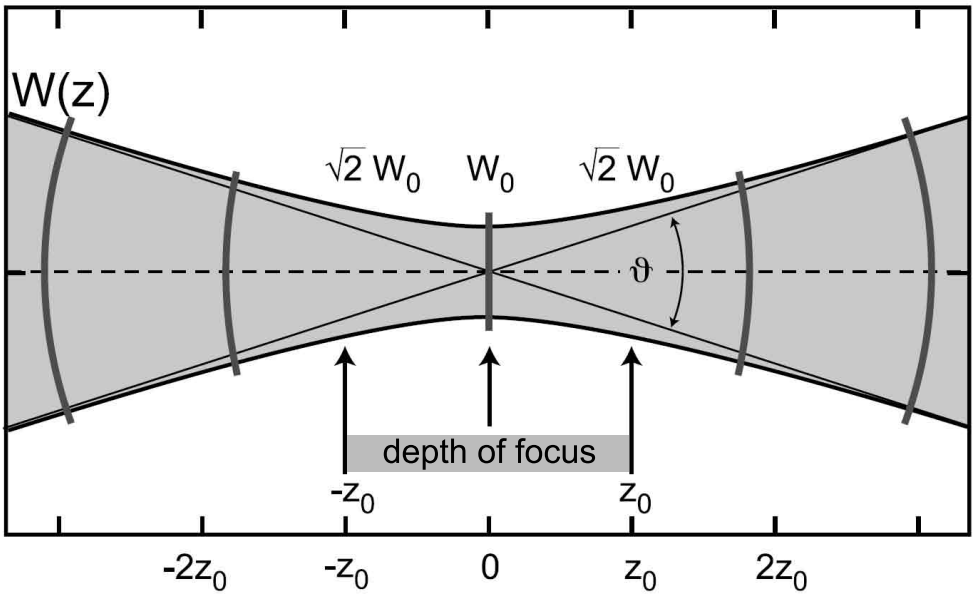

Figure 2.10: Width of the Gaussian beam from [51]. The beam width $W(z)$ is smallest at the waist position $z = 0$. The Rayleigh length z_0 is defined as the distance, where the beam radius has diverged by a factor of $\sqrt{2}$ from its minimal value W_0. The range of $2z_0$ around the waist position is sometimes denoted the depth of the focus.

Substituting (2.30) in (2.29) yields

$$E(x, y, z) = A_0 \frac{W_0}{W_z} \mathrm{e}^{-\frac{r^2}{W^2(z)}} \mathrm{e}^{-ikz - ik\frac{r^2}{2R(z)} + i\gamma(z)} \tag{2.34}$$

where A_0 is abbreviated for $\frac{A_1}{iz_0}$ and $\gamma(z) = \tan^{-1}\left(\frac{z}{z_0}\right)$ is a function describing the phase retardation at the beam axis with reference to a plane wave [39]. The corresponding intensity results in

$$I(r, z) = I_0 \frac{W_0^2}{W^2(z)} \mathrm{e}^{-\frac{2r^2}{W^2(z)}} \tag{2.35}$$

with $I_0 = |A_0|^2$. In total the Gaussian beam is completely specified by its direction, its waist location, A_0 and either W_0 or z_0 [39].

The wave front normals of a collimated beam may be considered as paraxial rays [39].

The Gaussian wave function in section 2.1.2 was for simplicity chosen real-valued, which is an approximation for the beam near the center. The waist radius is connected to the standard deviation of its probability distribution via $W_0 = 2\Delta Q_0$.

Temporal coherence

The coherence time is related to the coherence length l_c by $\tau_c = \frac{l_c n}{c}$ with the velocity of light c inside a medium with refractive index n [30]. It specifies the time over which the phase of the beam stays longitudinally correlated [16]. The coherence length is inversely proportional to the linewidth of the beam spectrum, in particular its full width at half maximum (FWHM) is given by [30]:

$$|\Delta\lambda_{\mathrm{FWHM}}| = \frac{2\sqrt{2}\ln(2)}{\pi}\frac{\lambda_{\mathrm{peak}}^2}{l_c} \tag{2.36}$$

The selection of a longitudinal mode results to a good approximation in monochromatic radiation or more precisely in a small spectral linewidth. This means high spectral coherence, which therefore also amounts to high temporal coherence.

2.2.4 Propagation in anisotropic media

Anisotropic media are asymmetrical regarding their dielectric properties [19]. This makes the propagation of light or rather the pointing vector $\vec{S}$, along which the photon energy travels, dependent on its polarization. If the anisotropic medium is otherwise linear, the induced electrical polarization reads

$$\vec{P}(\omega) = \varepsilon_0\hat{\chi}(\omega)\vec{E}(\omega) \qquad \text{with} \qquad \hat{\chi} = \begin{pmatrix} \chi_{11} & \chi_{12} & \chi_{13} \\ \chi_{21} & \chi_{22} & \chi_{23} \\ \chi_{31} & \chi_{32} & \chi_{33} \end{pmatrix} \tag{2.37}$$

with ε_0 the vacuum permittivity and $\hat{\chi}$ being the electric susceptibility of the material [19]. Unlike in an isotropic medium the electric susceptibility is not a scalar, but a tensor. Therefore in anisotropic media the induced polarisation $\vec{P}$ is in general not parallel to the electric field vector $\vec{E}$. With this likewise the electric displacement field $\vec{D}$, given by

$$\vec{D} = \varepsilon_0\vec{E} + \vec{P} = \varepsilon_0(1+\hat{\chi})\vec{E} = \varepsilon_0\hat{\varepsilon}_r\vec{E} \tag{2.38}$$

with $\hat{\varepsilon}_r$ the relative permittivity of the material, is in general not parallel to $\vec{E}$.

Dichroism

One anisotropic effect is dichroism. It describes the property of selective absorption of one linear polarization component along an axis distinguished by the dichroitic material. This means the electric susceptibility is not real-valued in that direction, because the imaginary part causes absorption. The perpendicular direction is hardly absorbed, but gets almost fully transmitted. This is exploited in polarisers, where a substrate containing a thin wire grid absorbs the polarisation along that direction [19]. The transformation matrix of a

linear polariser with the tilting angle θ starting from the horizontal position reads

$$\hat{T}_{\text{Polariser}}(\theta) = \begin{pmatrix} \cos^2(\theta) & \cos(\theta)\sin(\theta) \\ \sin(\theta)\cos(\theta) & \sin^2(2\theta) \end{pmatrix} \tag{2.39}$$

Birefringence

As the principle of birefringence plays a central role in the experiment presented in this thesis it is described in more detail. Here it is classified into linear and circular birefringence.

Linear birefringence

The principle of birefringence is caused by the fact that in anisotropic media there exist two allowed oscillation directions of $\vec{D}$ for a given wave vector $\vec{k}$ [19]. The latter is perpendicular to the wave front, which describes surfaces of constant phase. Likewise there exist two possible directions of $\vec{E}$ and - perpendicular to them - $\vec{S}$, which describes the direction of the group velocity v_g. The phase velocity of a wave packet v_{ph} is determined by the polarization direction, such that

$$v_{ph} = \frac{\omega}{k} = \frac{1}{\sqrt{\mu_0} D}. \tag{2.40}$$

Hence, the index of refraction

$$n = \frac{c}{v_{ph}} = \frac{D}{\sqrt{\varepsilon_0}} \tag{2.41}$$

is dependent on the direction of the wave vector and has two possible solutions, sometimes denoted by n_{fast} and n_{slow}, referring to the different values of the phase velocity [19]. The polarization vectors $\vec{D}$ of these two modes are orthogonal to each other [14]. For the further discussion we will focus on uniaxial materials. They exhibit one line of symmetry, namely the optical axis. By suitably transforming the coordinate system the relative permittivity then has two different components. Light with its electric field in a plane perpendicular to the optical axis will experience the component perpendicular to the optical axis $\varepsilon_{r\perp}$. This is referred to as ordinary beam because it is refracted ordinarily according to Snell's law of refraction with $n = n_o$, where the subscript o means ordinary. n_o is not dependent on the direction of the wave vector.

Light that has its electric field in a plane, which contains the optical axis, will be affected by $\varepsilon_{r\perp}$ as well as the parallel component $\varepsilon_{r\parallel}$ and therefore see both, n_o and n_e, where the subscript e denotes extraordinary. It is given by

$$n = n_e(\vartheta) = \frac{n_o n_e}{\sqrt{{n_o}^2 \sin^2(\vartheta) + {n_e}^2 \cos^2(\vartheta)}} \tag{2.42}$$

where ϑ denotes the angle between $\vec{k}$ and the optical axis [14]. The corresponding beam is called extraordinary.

Huygens principle, where wave fronts are illustrated as circles, is not appropriate here as elementary waves have to be described by ellipses, which is illustrated in Fig. 2.11. Their envelope is parallel to the incident envelope, but the direction of propagation $\vec{S}$, i.e. the energy flux, is changed. As a result $\vec{k}$ and $\vec{S}$ are not parallel.

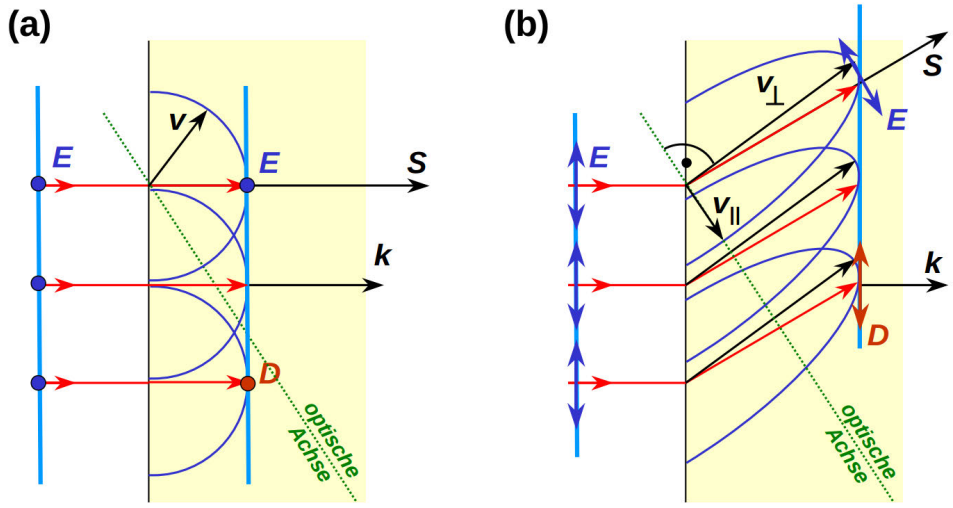

Figure 2.11: Illustration of linear birefringence from [19], where 'optische Achse' means optical axis. *a*) shows the ordinary case, where wave fronts can be described with circles. As the incidence is normal to the surface there is no refraction. In case *b*) the vectors $\vec{D}$ and $\vec{E}$ are not parallel and so are $\vec{S}$ and $\vec{k}$. This means that the energy travels in a different direction than the wave fronts, which have to be described by ellipses. This is called extraordinary refraction.

A uniaxial material is called positive when the extra-ordinary beam is the slow beam, while the ordinary is the fast one, i.e. the extra-ordinary index of refraction is greater than the ordinary. For a negative uniaxial medium it is vice versa [14]. The measure for birefringence is commonly expressed in the maximal difference of extra-ordinary and ordinary refractive index.

For the special case, when the propagation, i.e., the wave vector $\vec{k}$, is parallel to the optical axis of a crystal ($\vartheta = 0$), the two solutions for $\vec{D}$ are degenerate. This means $\vec{D}$ and $\vec{E}$ are parallel for the extraordinary beam and so are $\vec{k}$ and $\vec{S}$. Like in isotropic media the refractive index is not dependent on the direction of the wave vector, i.e. it can lie anywhere in the plane perpendicular to $\vec{k}$ and is given by n_o. That is, the degenerate ordinary beams are solely governed by Snell's law.

For the case when $\vec{k}$ is perpendicular to the optical axis ($\vartheta = 90°$) the extraordinary beam propagates at a different phase velocity, corresponding to the refractive index n_e, but $\vec{E}$ and $\vec{D}$ are parallel for the extra-ordinary beam and so are $\vec{k}$ and $\vec{S}$ [14].

A schematic to illustrate this is depicted in Fig 2.12, where the optical axis is in the surface plane of crystal. It is expressed in terms of the angle of incidence of the beam θ

and the respective refraction angles $\theta^{(o)}$ and $\theta^{(e)}$. The latter are each determined by Snell's law according to $\sin(\theta) = n_o \sin(\theta^{(o)}) = n_e \sin(\theta^{(e)})$, if incident from air with $n = 1$. With a crystal thickness d the separation distance δx of the ordinary and the extraordinary beam becomes:

$$\delta x = \delta x_e - \delta x_o = d \left(\frac{\sin(\theta - \theta^{(e)})}{\cos(\theta^{(e)})} - \frac{\sin(\theta - \theta^{(o)})}{\cos(\theta^{(o)})} \right) \tag{2.43}$$

where δx_o and δx_e are the respective beam displacements with reference to the original beam axis.

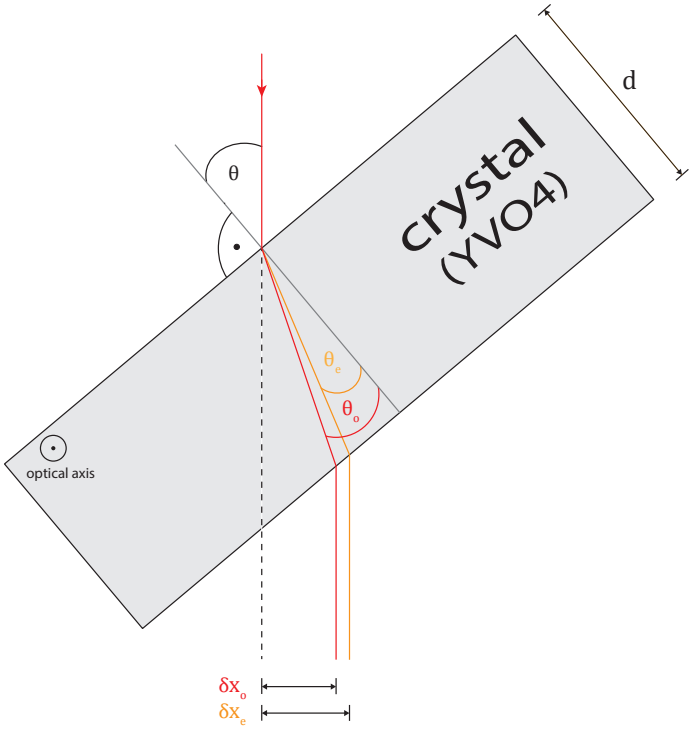

Figure 2.12: Schematic birefringence for the case when $\vec{E}$ and $\vec{D}$ are parallel. The beam is incident on a positive birefringent crystal from a medium with lower refractive index (air), such that $\vec{k}$ is perpendicular to the optical axis. The polarization of the ordinary beam is horizontal, i.e. in the plane of incidence, while the extraordinary beam is vertically polarised. The refraction can in both cases be described by Snell's law with refractive indices n_o and n_e. The resulting angles θ_e and θ_o are different, in particular the extra-ordinary beam is refracted more towards the crystal normal than the ordinary one. Therefore the displacements δx_o and δx_e are different.

The connection to the quantum mechanical description, in particular to the interaction Hamiltonian, where $\hat{A}$ is $\hat{\sigma}_z$ with eigenvalues $+1$ and -1 with respect to horizontal and

vertical polarization state may explicitly be expressed [47] by:

$$\delta x = 2g\epsilon \tag{2.44}$$

where each side of the equation are indicators of the strength of the interaction. Here the time ϵ is assumed equal for both polarization components. Note, however, that the mean displacement of the whole beam $\frac{\delta x_e + \delta x_o}{2}$ is not readily accounted for in the theoretical model.

The refractive indices n_e and n_o are dependent on the wavelength of the incident beam. The Sellmeier equation provides a good approximation for most optically transparent media [39]. For a birefringent crystal called yttrium orthovanadate (YVO4) at room temperature it reads [13],[51]

$$\begin{aligned} {n_e}^2(\lambda) &= 4.59905 + \frac{0.110534}{\lambda^2 - 0.04813} - 0.0122676\,\lambda^2 \\ {n_o}^2(\lambda) &= 3.77834 + \frac{0.069736}{\lambda^2 - 0.04724} - 0.0108133\,\lambda^2 \end{aligned} \tag{2.45}$$

where λ is in units of μm. The two components of polarization propagate with different phase velocities. Notable, even for perpendicular beam incidence ($\theta = 0$), where there is no refraction, the phase relation between ordinary and extraordinary beam changes according to the difference $\Delta n = n_e - n_o$

$$\Delta\varphi = 2\pi \frac{d}{\lambda} \Delta n. \tag{2.46}$$

Therefore, the overall polarization state changes during propagation and is different afterwards than beforehand, unless $\Delta\varphi$ is an integer multiple of 2π.

This is exploited for wave plates, where the phase is delayed between two linear polarization directions dependent on its thickness d. Commonly used are quarter-wave plates (QWP) and half-wave plates (HWP), where the phase is shifted by $\frac{\pi}{2}$ and π, respectively.

The transformation matrix of a HWP is given by [22]

$$\hat{T}_{\mathrm{HWP}}(\theta) = \begin{pmatrix} \cos(2\theta) & \sin(2\theta) \\ \sin(2\theta) & -\cos(2\theta) \end{pmatrix} = \sin(2\theta)\hat{\sigma}_x + \cos(2\theta)\hat{\sigma}_z, \tag{2.47}$$

For $\theta = 22.5°$ the HWP operation reads $\frac{1}{\sqrt{2}}(\hat{\sigma}_x + \hat{\sigma}_z)$. A QWP transforms according to

$$\begin{aligned} \hat{T}_{\mathrm{QWP}}(\theta) &= \begin{pmatrix} \cos^2(\theta) - i\sin^2(\theta) & (1+i)\sin(\theta)\cos(\theta) \\ (1+i)\sin(\theta)\cos(\theta) & -i\cos^2(\theta) + \sin^2(\theta) \end{pmatrix} \\ &= \frac{1}{2}((1-i)\mathbb{I} + 2(1+i)\cos(\theta)\sin(\theta)\hat{\sigma}_x + (1+i)\cos(2\theta)\hat{\sigma}_z). \end{aligned} \tag{2.48}$$

The corresponding transformation matrix for the YVO crystal itself is given by

$$\begin{aligned}\hat{T}_{\mathrm{YVO}}(\varphi) &= \begin{pmatrix} i\cos(\frac{\varphi}{2}) + \sin(\frac{\varphi}{2}) & 0 \\ 0 & i\cos(\frac{\varphi}{2}) - \sin(\frac{\varphi}{2}) \end{pmatrix} \\ &= i\cos\left(\frac{\varphi}{2}\right)\mathbb{I} + \sin\left(\frac{\varphi}{2}\right)\hat{\sigma}_z \end{aligned} \tag{2.49}$$

Circular birefringence
Circular birefringence, also called optical rotation, amounts to the rotation of incident linear polarized light, irrespective of its polarization direction. The angle of rotation α is proportional to the path length, i.e. the thickness of the material d:

$$\alpha = \alpha_s \cdot d \tag{2.50}$$

where α_s is called specific rotation [19]. Analogously to the linear birefringence, which induces two orthogonal linearly polarized wave packets travelling with different phase velocities, circular birefringence induces two orthogonal circularly polarized wave packets travelling with different phase velocities. This may be understood due to the fact that linear polarization can always be written as a superposition of right and left circular polarization. When exiting the circular birefringent material, the decomposed beams, whose electric field vectors rotated by unequal amounts inside, recombine to a linearly polarized wave packet, whose polarization direction is rotated according to α [2]. Analogously, the measure for circular birefringence is expressed in the difference of the two refractive indices.

The effect of circular birefringence may either be an intrinsic property of the material, which is then called optical activity. Or it may be induced in a material by an external static magnetic field, parallel to the propagation direction of the light, which is then called Faraday effect. In the above expression the specific rotation is then replaced by a factor containing the magnetic field. This phenomenon is for example exploited in optical isolators.

2.3 Suitable measures

The essence of this work is the comparison of different quantum states, which is experimentally realized by bringing them to interference. To connect the resulting classical intensity modulation with an expression for the distance measure of two quantum states, the following relations are needed.
Visibility
The visibility V is a measure of the interference strength

$$V = \frac{I_{max} - I_{min}}{I_{max} + I_{min}} \tag{2.51}$$

where I_{max} and I_{min} are the extremal values of the sinusoidal intensity signal, which arises by varying the phase difference of the two interfering arms [39].

Fidelity

The fidelity F serves as a measure for the spatial proximity of two quantum states in Hilbert space and may be given by

$$F(\rho_1, \rho_2) = \mathrm{tr}\left(\sqrt{\sqrt{\hat{\rho}_1}\hat{\rho}_2\sqrt{\hat{\rho}_1}}\right) \tag{2.52}$$

The quantity is symmetric in its input arguments, non-negative and smaller than or for the case $\hat{\rho}_1 = \hat{\rho}_2$ equal to one. Furthermore it is invariant equal under unitary transformations, i.e. $F(\hat{U}\hat{\rho}_1\hat{U}^\dagger, \hat{U}\hat{\rho}_2\hat{U}^\dagger) = F(\hat{\rho}_1, \hat{\rho}_2)$ [31]. If the reference state is a pure state $|\Psi\rangle$, the expression simplifies to

$$F(|\Psi\rangle, \hat{\rho}_2) = tr\left(\sqrt{\langle\Psi|\hat{\rho}_2|\Psi\rangle|\Psi\rangle\langle\Psi|}\right) = \sqrt{\langle\Psi|\hat{\rho}_2|\Psi\rangle}. \tag{2.53}$$

Thus, the fidelity is the square root of the transition probability and therefore equal to the overlap between the states $|\Psi\rangle$ and $\hat{\rho}$.

Bures angle

While the fidelity itself is not a metric on the state space of density matrices, we can use purification and Uhlmann's theorem to see that a related definition, the Bures angle, provides a metric. Purification describes a mathematical technique, which allows to relate mixed states to pure states. A given density matrix $\hat{\rho}_A$ of a quantum system A may be written in terms of a pure state $|AB\rangle$ of a composed system AB, i.e. $\hat{\rho}_A = tr_R(|AB\rangle\langle AB|)$, where B is a virtual external system. By taking only system A into account one is left with the original mixed state [31].

Furthermore we use Uhlmann's theorem, for which $\hat{\rho}_1$ and $\hat{\rho}_2$ are mixed states of a quantum system A, with purifications $|\Psi_1\rangle$ and $|\Psi_2\rangle$ via a system B, respectively. Then

$$F(\hat{\rho}_1, \hat{\rho}_2) \geq |\langle\Psi_1|\Psi_2\rangle| \tag{2.54}$$

with equality for

$$F(\hat{\rho}_1, \hat{\rho}_2) = \max_{|\Psi_1\rangle, |\Psi_2\rangle} |\langle\Psi_1|\Psi_2\rangle| \tag{2.55}$$

where the maximization is over all purifications $|\Psi_1\rangle$ and $|\Psi_2\rangle$ into AB [31]. The fidelity between two mixed states equals the maximal overlap of respective purifications.

Using the fidelity, the angle between two vectors in Hilbert space, the Bures angle, may be defined as

$$D_A(\hat{\rho}_1, \hat{\rho}_2) = \arccos\left(F(\hat{\rho}_1, \hat{\rho}_2)\right). \tag{2.56}$$

By Uhlmann's theorem one can verify that this quantity fulfils the triangle inequality. Furthermore it vanishes if $\hat{\rho}_1 = \hat{\rho}_2$. Together with symmetry and non-negativity the Bures angle is a metric [31].

Connecting the quantities for interference experiment

For relating the visibility to the fidelity and therefore the Bures angle, let's first assume not-normalized states, such that $\langle U_1|U_1\rangle = I_1$ and $\langle U_2|U_2\rangle = I_2$ [39]. Interference of the two states yields the intensity modulation

$$\begin{aligned} I &= (\langle U_1| + \langle U_2|)\,(|U_1\rangle + |U_2\rangle) = \langle U_1|U_1\rangle + \langle U_2|U_2\rangle + \langle U_1|U_2\rangle + \langle U_2|U_1\rangle \\ &= I_1 + I_2 + 2\,\mathrm{Re}(\langle U_1|U_2\rangle) = I_1 + I_2 + 2|\langle U_1|U_2\rangle|\cos\zeta. \end{aligned} \tag{2.57}$$

$I_{\max}$ and $I_{\min}$ are the extremal value of I when the relative phase ζ is varied. Inserting these values into Eq. (2.51) results in

$$V = \frac{2\sqrt{I_1 I_2}}{I_1 + I_2}\left|\frac{\langle U_1|U_2\rangle}{\sqrt{\langle U_1|U_1\rangle}\sqrt{\langle U_2|U_2\rangle}}\right| = \frac{2\sqrt{I_1 I_2}}{I_1 + I_2}|\langle \tilde{U}_1|\tilde{U}_2\rangle| \tag{2.58}$$

where $|\tilde{U}_1\rangle$ and $|\tilde{U}_2\rangle$ are the normalized wave functions. If the intensities are equal, i.e., $I_1 = I_2$, it reduces to

$$V = |\langle \tilde{U}_1|\tilde{U}_2\rangle|, \tag{2.59}$$

which is equal to the fidelity of these states. Note that $|\tilde{U}\rangle$ may also represent a purification of a density matrix $\rho_{\tilde{U}}$. In this case the maximal visibility is equal to the fidelity if the purification states are maximized.

Therefore the resulting relation is defined as

$$D_A(\hat{\rho}_1, \hat{\rho}_2) = \arccos\left(V_{\max}\right). \tag{2.60}$$

3 Properties of weak values

In the following the concept of weak values will be introduced, from the main idea and general considerations to its major application and associated interpretational issues. To elaborate on its properties, in particular its differences and similarities to the standard - preselected only - measurement scheme, its behaviour will be compared with that of ordinary quantities, as expectation values and eigenvalues, where the proximity of the respective pointer states serves as criterion for similarity.

3.1 Main Idea

The weak value was introduced in the framework of a weak measurement, where post-selection onto a particular state of the object's subspace is added, before reading off the pointer, which is depicted in Fig. 3.1.

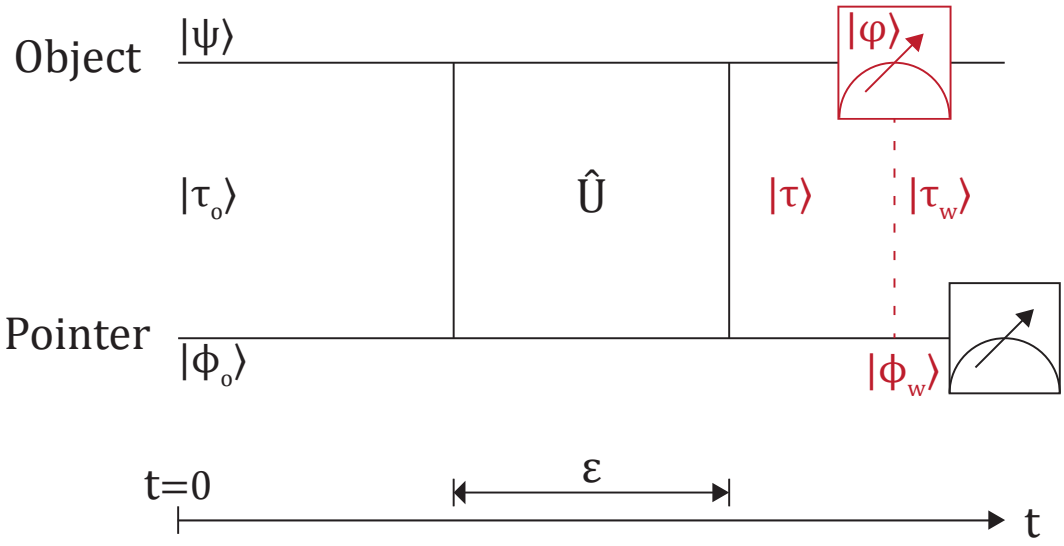

Figure 3.1: Pre- and postselected measurement scheme

Therefore all assumptions from section 2.1.2 apply here, too. After the pre-measurement, which evolved object and pointer system into the entangled state $|\tau\rangle = \sum_{i=1}^{d_s} c_i|a_i\rangle \otimes \mathrm{e}^{-\frac{i\epsilon g}{\hbar}a_i\hat{X}}|\phi_0\rangle = \sum_{i=1}^{d_s} c_i|a_i\rangle \otimes |\phi_i\rangle$, the object's subspace is projected onto $|\varphi\rangle = \sum_{i=1}^{d_s} c_i'|a_i\rangle$, which is not orthogonal to the objects initial state $|\psi\rangle$. Due to the correlation between the

systems this also changes the pointer state, such that the resulting dis-entangled product state reads

$$|\tau_w\rangle = (\hat{\Lambda}_\varphi \otimes \hat{I})|\tau\rangle = |\varphi\rangle \otimes |\phi_w\rangle \tag{3.1}$$

where the pointer state, up to the normalization constant $\mathcal{N} = 1/\sqrt{\text{prob}(\varphi|\tau)}$, can be expanded and approximated as

$$\begin{aligned}\mathcal{N}^{-1}|\phi_w\rangle &= \sum_{i=1}^{d_s} c_i'^* c_i |\phi_i\rangle = \sum_{i=1}^{d_s} \langle\varphi|a_i\rangle\langle a_i|\psi\rangle \left[\hat{I} - \tfrac{i\epsilon g}{\hbar} a_i \hat{X} + \sum_{r=2}^{\infty} \tfrac{(-i\epsilon g a_i \hat{X}/\hbar)^r}{r!}\right] |\phi_0\rangle \\ &= \langle\varphi|\psi\rangle \left[1 - \tfrac{i\epsilon g}{\hbar} A_w \hat{X} + \sum_{r=2}^{\infty} \tfrac{(-i\epsilon g \hat{X}/\hbar)^r}{r!} (A^r)_w\right] |\phi_0\rangle \\ &= \langle\varphi|\psi\rangle \left[\mathrm{e}^{-\frac{i\epsilon g}{\hbar} A_w \hat{X}} + \sum_{r=2}^{\infty} \tfrac{(-i\epsilon g \hat{X}/\hbar)^r}{r!} \left((A^r)_w - (A_w)^r\right)\right] |\phi_0\rangle \approx \langle\varphi|\psi\rangle\, \mathrm{e}^{-\frac{i\epsilon g}{\hbar} A_w \hat{X}} |\phi_0\rangle\end{aligned} \tag{3.2}$$

neglecting the second term in the last step [45]. Here

$$(A^r)_w = \frac{\sum_{i=1}^{d_s} c_i'^* c_i a_i^r}{\sum_{i=1}^{d_s} c_i'^* c_i} = \frac{\langle\varphi|\hat{A}^r|\psi\rangle}{\langle\varphi|\psi\rangle} \quad \text{with the quantity} \quad A_w = (A^1)_w = \frac{\langle\varphi|\hat{A}|\psi\rangle}{\langle\varphi|\psi\rangle} \tag{3.3}$$

named the weak value of the observable $\hat{A}$, which depends on both the pre- and the post-selected state of the object system. This newly defined quantity exhibits unusual properties. Unlike an expectation value of a bounded observable, it is not restricted to the spectrum of eigenvalues and can even be complex. The difference arises due to the postselection. If the weak value is complex, the expression $\mathrm{e}^{-\frac{i\epsilon g}{\hbar} A_w \hat{X}}$ constitutes a nonunitary operation, which may be understood as increasing or decreasing the probability of postselection dependent on the imaginary part $\text{Im}(A_w)$ or equivalently changing the expected relative size of the ensemble which survives the postselection [5, 8]. Thus, the nonunitary process can be interpreted as an effective Hamiltonian which creates or destroys systems. [8] The conditions for the above approximation to hold, can be formulated as

$$\frac{\epsilon g}{\hbar} \Delta X \max \left| \frac{(A^r)_w}{A_w} \right|^{\frac{1}{r-1}} \ll 1 \qquad (r = 2, 3, ...) \tag{3.4}$$

and

$$\frac{\epsilon g}{\hbar} \Delta X |A_w| \ll 1. \tag{3.5}$$

The first relation ensures the weakness of the interaction within the pre-and-postselected measurement [24]. Recalling section 2.1.2 a weak interaction means that the correlation between the object states $|a_i\rangle$ and the pointer states $|\phi_i\rangle$ is not unique because different pointer states overlap almost completely and therefore the object state is almost left unaffected. Whereas the second, stronger condition manifests itself in the linear shift in the probability distribution for $\hat{M}$, whose shape is otherwise unchanged in these limits

[24]. With both requirements simultaneously fulfilled, the averaged pointer readout of any observable $\hat{M}$ evolves according to [21, 42]

$$\langle\phi_w|\hat{M}|\phi_w\rangle - \langle\phi_0|\hat{M}|\phi_0\rangle \approx$$
$$\mathcal{D}\left(i\frac{\epsilon g}{\hbar}\,\mathrm{Re}(A_w)\langle\phi_0|[\hat{X},\hat{M}]|\phi_0\rangle + \frac{\epsilon g}{\hbar}\,\mathrm{Im}(A_w)\left(\langle\phi_0|\{\hat{X},\hat{M}\}|\phi_0\rangle - 2\langle\phi_0|\hat{X}|\phi_0\rangle\langle\phi_0|\hat{M}|\phi_0\rangle\right)\right) \quad . \tag{3.6}$$

Here the normalization constant $\mathcal{D}$ is abbreviated for $\mathcal{N}|\langle\varphi|\psi\rangle|^2$. It is to first order approximation a function of the weak value of $\hat{A}$, which is the only quantity related to the object system that remains [42]. While the first term of the equation looks familiar from the expression for preselected only, i.e. standard measurements with $\langle\hat{A}\rangle$ replaced by $\mathrm{Re}(A_w)$, which results from $\mathrm{e}^{-\frac{i\epsilon g}{\hbar}\mathrm{Re}(A_w)\hat{X}}$, the second term arises due to the action of the operator $\mathrm{e}^{\frac{\epsilon g}{\hbar}\mathrm{Im}(A_w)\hat{X}}$. If the overlap between pre-and postselected state is rather small, the real and the imaginary part of the weak value gets accordingly large. As a consequence the shift in the expectation value of the pointer observable can exceed the spectral range of the object observable $\hat{A}$ by far, i.e. it can get much larger than the shift without postselection. This amplifying effect is implemented in experiments for determining a small unknown parameter g. However it comes with a drawback in that for a small overlap the associated probability of post-selection becomes small. Expanding the latter to second order with the assumption that $\langle\hat{X}\rangle_0 = 0$ reads $\mathrm{prob}(\varphi|\tau) = |\langle\varphi|\psi\rangle|^2(1 - \frac{\epsilon^2 g^2}{\hbar^2}\langle\hat{X}^2\rangle_0\,(\mathrm{Re}(A^2{}_w) - |A_w|^2)$, such that the normalization constant may be approximated to $\mathcal{D} = \dfrac{|\langle\varphi|\psi\rangle|^2}{\mathrm{prob}(\varphi|\tau)} \approx 1$ to first order. Each the real and the imaginary part of A_w may be determined by measuring suitably chosen observables $\hat{M}$. The latter may even commute with the observable involved in the interaction $\hat{X}$, i.e. $\hat{M} = \hat{X}$. This case has no analogue in the standard, pre-selected only measurement scheme because there is no shift in $\langle\hat{X}\rangle$ there. Therewith Eq. 3.6 reads

$$\langle\hat{X}\rangle_w - \langle\hat{X}\rangle_0 = \mathcal{D}\frac{2\epsilon g}{\hbar}\,\mathrm{Im}(A_w)(\Delta X_0)^2 \tag{3.7}$$

By measuring both, the input observable $\hat{X}$ and any non-commuting output observable $\hat{M}$, one gets two relations to deduce both unknowns, the real and the imaginary part of the weak value of $\hat{A}$. Remarkably, the simple relation for the pointer output, namely its linear shift by the weak value, holds for arbitrary systems in weak pre- and postselected measurements under the stated limits. The linear dependence of the outcome on A_w is sometimes referred to as the *linear-response regime* or *AAV limit*.

3.2 Extensions

Outside of this regime, when the pre-and postselected states are nearly orthogonal a nonlinear approximation becomes necessary, even if the interaction is still considered weak.

Higher orders - in particular the probability in the denominator of the normalization constant cannot be neglected any more. The average shift decreases rapidly with decreasing overlap of pre-and postselected states. That is, for a given weak interaction strength there exists a maximal outcome, which can be achieved with an optimal overlap [49].

Furthermore there exist generalizations for exactly orthogonal pre-and postselection states, which require a distinct definition of the weak value. This case is meaningful because the pre-selected state may undergo a slight change due to the weak interaction, so that there might still be a non-zero overlap with the postselection state, under the further assumption that neither the preselected nor the postselected state commutes with the observable $\hat{A}$ [49]. However, the amplifying effect is not limited to weak interactions only and is to some extent still visible beyond weak interactions. Resulting pointer shifts in general non-ideal pre-and postselected measurements have been related to corresponding higher order, semi-weak or generalized weak values [33]. The respective pointer probability distributions then display profiles with d pronounced peaks together with remaining interference between the single distributions depending on the overlap of different pointer wave functions.

3.3 Canonically conjugated pointer observables

Let us recall the setting from the preselected-only measurement in section 2.1.2 where the pointer observable $\hat{X}$ is replaced by the momentum $\hat{P}$ and the pre-measurement entangling the two systems is assumed weak, such that the pointer's wave function in position space is shifted by $\epsilon g\langle\hat{A}\rangle$. As a result of a following projective postselection on the object's subspace it evolves into

$$\phi_1(q) \to \phi_w(q) \approx \phi_0\left(q - \epsilon g A_w\right) \tag{3.8}$$

under the above conditions. Thus, it may exceed the spectrum of $\hat{A}$ depending on the post-selection or rather the overlap of pre-and postselected states. The corresponding shift in the expectation value of $\hat{Q}$ is given by

$$\langle\hat{Q}\rangle_w - \langle\hat{Q}\rangle_0 \approx (\epsilon g\,\mathrm{Re}(A_w)) \tag{3.9}$$

and the one of $\hat{P}$ reads

$$\langle\hat{P}\rangle_w = \frac{2\epsilon g}{\hbar}\,\mathrm{Im}(A_w)(\Delta P_0)^2. \tag{3.10}$$

As above the initial expectation value $\langle\hat{P}\rangle$ is assumed to vanish, which is definitely the case for a pure initial pointer state, that is an even wave function [49]. Here also the expectation value of the anti-commutator is assumed to vanish, which is the case if the initial pointer wave function is purely real-valued up to an overall constant phase [21].

Example a) To illustrate how the pointer probability distribution in $\hat{Q}$ space is anomalously shifted, we consider the example given in 2.1.2, where $\hat{A} = \frac{1}{\sqrt{2}}(\hat{\sigma}_x + \hat{\sigma}_z)$ and the preselected state is $|\psi\rangle = |P\rangle$. With a postselected state $|\varphi\rangle = |H\rangle$, the weak value is

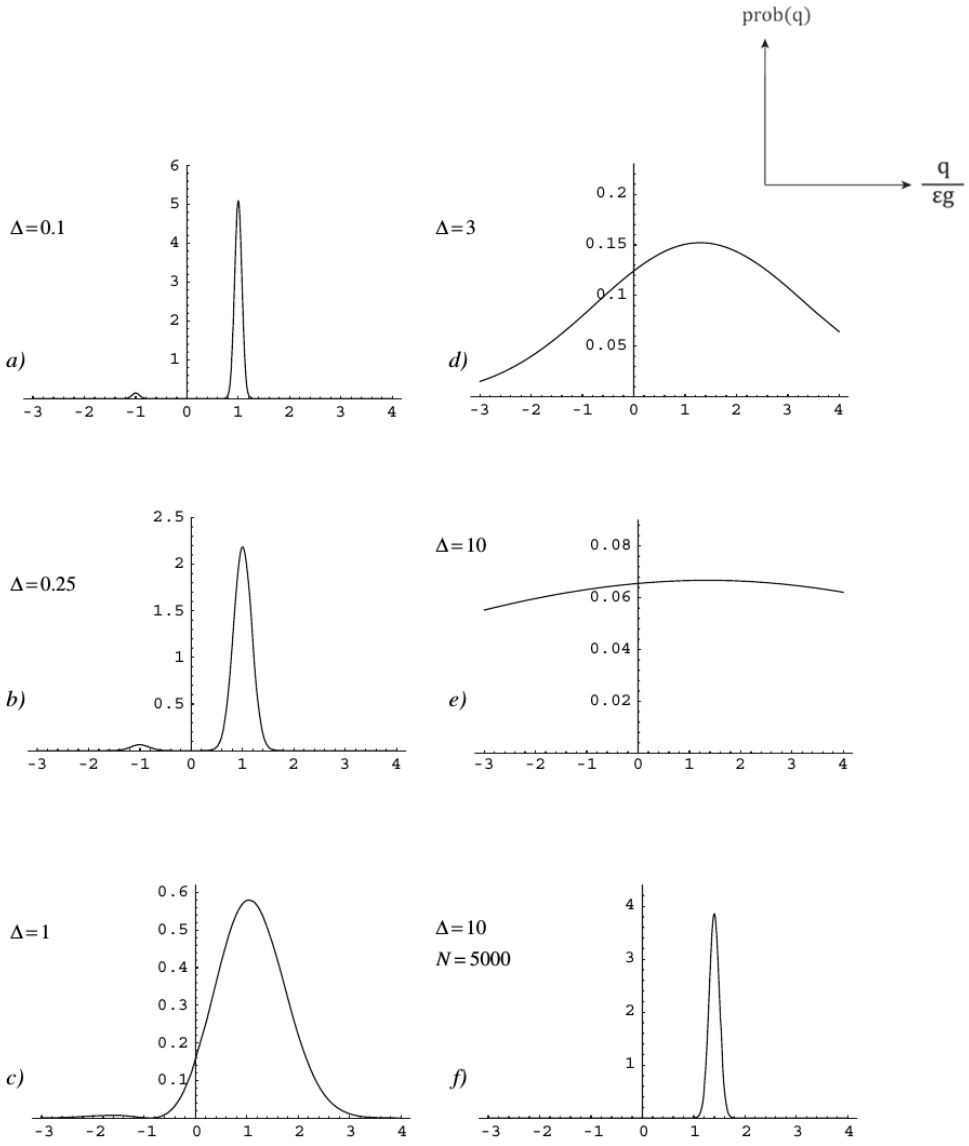

Figure 3.2: Probability distribution in $\hat{Q}$ space of a pre- and postselected measurement with $A_w = \frac{\frac{1}{\sqrt{2}}\langle H|\hat{\sigma}_x+\hat{\sigma}_z|P\rangle}{\langle H|P\rangle} = \sqrt{2}$. Case a) and b) are considered strong measurements as the standard deviation given here is $\Delta = \sqrt{2}\Delta Q_0 \ll 1$, such that the distribution has distinct peaks located at the eigenvalues, where $+1$ is more probable than -1. Cases $c)-f)$ show the change to a weak pre-and postselected measurement by increasing Δ, which results in a single broad peak at the weak value $A_w = \sqrt{2}$, located outside the spectrum of $\hat{A}$. The shift becomes resolvable in case f), where $N = 5000$ object-pointer systems are used to reduce Δ by the factor $\frac{1}{\sqrt{N}}$ to about 0.14. Figure modified from [10].

given by $A_w = \frac{\frac{1}{\sqrt{2}}\langle H|\hat{\sigma}_x+\hat{\sigma}_z|P\rangle}{\langle H|P\rangle} = \sqrt{2}$, which is outside the eigenvalue spectrum of the observable. In Fig. 3.2 the evolution of the final pointer probability distribution from a strong to a weak PPS measurement is shown [10].

Example b) To elaborate on the amplification phenomenon of the weak value, it is instructive to examine the results of a weak pre-and postselected measurement without approximations. To this end we consider the example given in section 2.1.2, where the pointer wave function is Gaussian, $\hat{A} = \hat{\sigma}_z$ and ψ is given by Eq. (2.1).

The pointer state after postselection reads

$$\phi_w(q) = \mathcal{N}(\alpha\phi_0(q-\epsilon g) + \beta\phi_0(q+\epsilon g)) \tag{3.11}$$

with the abbreviations $\alpha = a\langle\varphi|H\rangle$ and $\beta = b\langle q|V\rangle$ and $\mathcal{N} = 1/\sqrt{\text{prob}(\varphi|\tau)}$ as above. The latter is given without approximations by

$$\begin{aligned}\text{prob}(\varphi|\tau) = \int \text{dq}\,|\phi_w(q)|^2 &= |\alpha|^2 + |\beta|^2 + 2\,\text{Re}\left(\int \text{dq}\,\alpha\phi_0(q-\epsilon g)\beta^*\phi_0(q+\epsilon g)^*\right) \\ &= |\alpha|^2 + |\beta|^2 + 2J\,\text{Re}(\alpha\beta^*)\end{aligned} \tag{3.12}$$

with the overlap integral $J = \int \text{dq}\,\phi_0(q-\epsilon g)\phi_0(q+\epsilon g)^*$ [42]. The resulting position expectation value reads [42]

$$\langle\hat{Q}\rangle_w = \frac{\epsilon g(|\alpha|^2 - |\beta|^2}{|\alpha|^2 + |\beta|^2 + 2J\,\text{Re}(\alpha\beta^*)} \tag{3.13}$$

From the comparison with the corresponding mean value for standard, pre-selected only measurements $\langle\hat{Q}\rangle$ in (2.19), it becomes clear that the postselection allows for a much higher output shift due to the denominator $\text{prob}(\varphi|\tau)$ in $\langle\hat{Q}\rangle_w$. The so-called amplification factor is the quotient $\dfrac{\langle\hat{Q}\rangle_w}{\langle\hat{Q}\rangle}$, which may exceed unity by far. The magnitude of the averaged shift can be expressed as [42]

$$\left|\langle\hat{Q}\rangle_w\right| \leq \frac{\epsilon g}{\sqrt{1-J^2}} \tag{3.14}$$

. It is maximal for a specific overlap, namely $\langle\varphi|\psi\rangle = \alpha\frac{1}{J}\left(\pm\sqrt{1-J^2} - (1-J)\right)$. Therewith the probability reads [42]

$$\text{prob}(\varphi|\tau) = 2\frac{|\alpha|^2(1-J^2)}{1+\sqrt{1-J^2}} \tag{3.15}$$

As a result the amplification increases as $J \to 1$ [42]. Under the assumption that the initial wave function is a Gaussian the associated variance of $\hat{Q}_w$ is given by [42]

$$(\Delta Q_w)^2 = (\Delta Q_0)^2 + \epsilon^2 g^2\left(\frac{|\alpha|^2+|\beta|^2}{\text{prob}(\varphi|\tau)} + \left(\frac{|\alpha|^2-|\beta|^2}{\text{prob}(\varphi|\tau)}\right)^2\right). \tag{3.16}$$

At maximal shift $\langle\hat{Q}\rangle_w^{\max}$ it is equal to the initial variance, i.e. $(\Delta Q_w)^2 = (\Delta Q_0)^2$, independent of the interaction strength [42].
Under the weak measurement condition the overlap integral may be approximated by $J \approx 1 - \frac{1}{2}\left(\frac{\epsilon^2 g^2}{\hbar^2}\right)^2 \langle\hat{P}^2\rangle_0 + \mathcal{O}(\epsilon^3 g^3)$ such that the maximal shift may be estimated at [42]

$$\langle\hat{Q}\rangle_w^{max} \approx \hbar\left(\langle\hat{P}^2\rangle_0\right)^{-\frac{1}{2}} \sim \left(\langle\hat{Q}^2\rangle_0\right)^{\frac{1}{2}} \tag{3.17}$$

which means the amplification is bounded by the initial standard deviation of $\hat{Q}$. The respective approximation for the probability reads [42]

$$\text{prob}(\varphi|\tau) \approx \left(\frac{\epsilon^2 g^2}{\hbar^2}\right)^2 |\alpha|^2 \langle\hat{P}^2\rangle_0 \propto \left(\langle\hat{Q}\rangle_w^{max}\right)^{-2} \tag{3.18}$$

underlining the fact that large amplification appears only very rarely for a single system [42].

3.4 General considerations

The standard definition of an expectation value of an observable is the weighted average of its eigenvalues, i.e. $\langle\psi|\hat{A}|\psi\rangle = \sum_{i=1}^{d_s} a_i |\langle a_i|\psi\rangle|^2$. A possible interpretation in terms of weak values is provided by the following sum rule:

$$\langle\hat{A}\rangle = \langle\psi|\hat{A}|\psi\rangle = \sum_j \langle\psi|\varphi_j\rangle\langle\varphi_j|\hat{A}|\psi\rangle = \sum_j |\langle\psi|\varphi_j\rangle|^2 \frac{\langle\varphi_j|\hat{A}|\psi\rangle}{\langle\varphi_j|\psi\rangle} = \sum_j \text{prob}(\varphi_j|\psi) A_{wj}, \tag{3.19}$$

which links $\langle\hat{A}\rangle$, as the outcome of a pre-selected only measurement, with the weighted average of weak values A_{wj}, as the linear outcome of weak pre- and post-selected systems (PPS). The weak values, which lie outside the spectral bounds of $\hat{A}$ due to a small overlap $|\langle\varphi_j|\psi\rangle|$, are weighted with accordingly small probabilities, which ensures that the result is constrained to the spectrum of eigenvalues of $\hat{A}$. An equivalent formulation of the above expression reads

$$\sum_j |\langle\varphi_j|\psi\rangle|^2 \,\text{Re}(A_{wj}) = \langle\hat{A}\rangle \quad \text{and} \quad \sum_j |\langle\varphi_j|\psi\rangle|^2 \,\text{Im}(A_{wj}) = 0 \tag{3.20}$$

meaning that the imaginary part cancels out in the calculation [24]. There is a similar formulation for the second moment of $\hat{A}$, namely [20]

$$\langle\psi|\hat{A}^2|\psi\rangle = \sum_j |\langle\varphi_j|\psi\rangle|^2 A_{wj}^* A_{wj} = \sum_j \text{prob}(\varphi_j|\psi)|A_{wj}|^2 \tag{3.21}$$

which enters the standard deviation ΔA. Using the relation [9]

$$\hat{A}|\psi\rangle = \langle\hat{A}\rangle|\psi\rangle + \Delta A|\chi\rangle, \tag{3.22}$$

which holds for a normalized state $|\chi\rangle$ being orthogonal to $|\psi\rangle$, and by choosing a post-selection state as $|\tilde{\varphi}\rangle = u|\psi\rangle + |\chi\rangle$ with $0 \neq u \in \mathbb{C}$, one finds [25]

$$A_w = \frac{\langle\tilde{\varphi}|\hat{A}|\psi\rangle}{\langle\tilde{\varphi}|\psi\rangle} = \langle\hat{A}\rangle + \frac{\Delta A}{u^*}. \tag{3.23}$$

Interestingly, the weak value can be expressed in terms of the two ordinary quantities expectation value and standard deviation and simultaneously attain an arbitrary complex number by designing u in $|\tilde{\varphi}\rangle$ appropriately, unless $|\psi\rangle$ is an eigenstate of $\hat{A}$, then $\Delta A = 0$ [25]. This leads to a peculiar property of pre-and post-selected systems in general, irrespective of the strength of the measurement interaction. If either the pre- or the post-selected state is an eigenstate of the measured observable, the weak value is fixed, equal to the respective eigenvalue. Thus, if both are unequal eigenstates corresponding to two non-commuting observables, the latter have definite values, despite the absence of common eigenstates. By contrast, in pre-selected only systems two observables simultaneously exhibit sharp values only if they commute, i.e. have a common set of eigenstates [24, 18].

3.5 Applications

The weak value has its most practical application as a metrological technique. The idea is schematically displayed in Fig. 3.3.

The first experiment which utilized weak pre-and postselected measurements for its potential in amplifying small quantities was the observation of the optical spin-Hall-effect in 2008 [28], which cannot be observed with traditional measurement schemes. On one hand the effect of signal amplification helps to improve the signal-to-noise ratio, but on the other hand the simultaneous decrease in the overall measurement probability contributes to statistical loss [25]. Recent analysis which allows for uncontrollable uncertainty of measurements in its estimate, i.e. which cannot be modelled statistically, suggests that this trade-off relation indeed provides a range of problems, where the weak value protocol is advantageous over others [25]. In particular, its application is useful whenever technical noise limits the sensitivity, i.e. the resolution of the measuring device is insufficient to detect a possible shift, whilst enough systems are available [25]. Then it represents a valuable and a facile option to overcome these technical limitations [46]. This is exploited both in quantum and in classical experimental settings because the effect can be mimicked with classical waves.

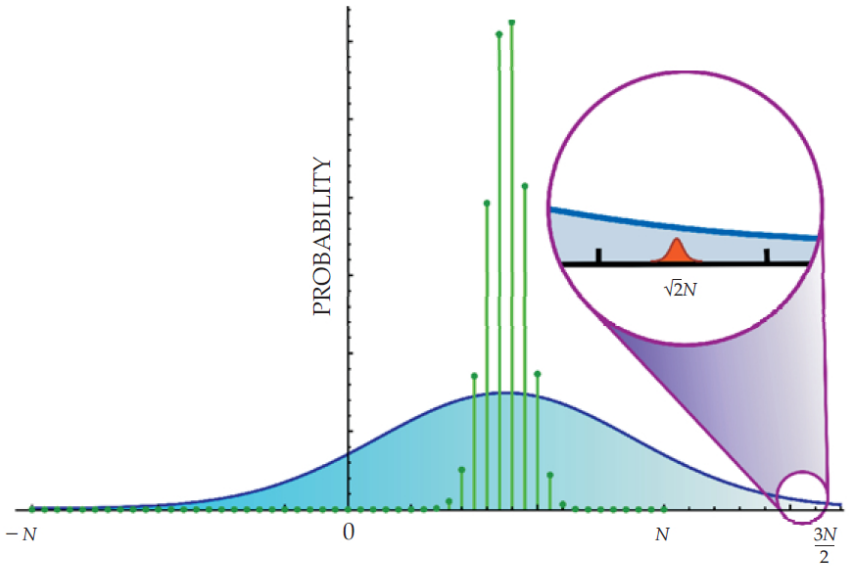

Figure 3.3: The weak value as metrological technique. Schematically shown are the probability distributions of N systems referring to example a) above. The green bars denote the possible outcomes of an ideal measurement without postselection. The broad blue distribution corresponds to probabilities in a weak measurement. The tail of the former includes the small postselection probability, as shown in the inset, which corresponds to a weak PPS measurement with $A_w = \sqrt{2}$. This amplifying effect can be useful in determining small quantities. Figure modified from [7]

3.6 What is the weak value?

The concept of weak values is accepted in the science community. Indeed, the formalism itself is hardly controversial, unless it comes to interpreting this new quantity. So far no consensus has been reached on this issue, despite the extensive investigation of its usefulness for various purposes.

One possible interpretation is to explain weak values as measurement errors [8]. To elaborate on this, we leave out the post-selection for now. Ideal measurements are defined to yield eigenvalues of the observable under study as outcomes. In this limit the uncertainty in the configuration space of the pointer, say q, and the amount, by which the pointer is shifted corresponds to an eigenvalue [8]. In a weak measurement, however, the uncertainty in q space - let's assume a Gaussian wave function for simplicity - is required to be comparably large. Then it is in principle possible for the pointer to yield any value due to the uncertainty, unrelated to the object observable [8]. This can be understood as the scatter around the intended value, which typically scales with the order $\sqrt{N}$ for an ensemble of N object-pointer systems [7]. Errors outside of this range may be explained by interference effects in the pointer. However, the probability for such large errors to appear is decreasing

the larger they are [7]. For all cases where the postselection succeeded, corresponding to an 'unusual' weak value, the pointer wave function before the postselection must have constructively interfered to this value and destructively anywhere else [8]. That's the reason why successful weak pre-and postselected measurements consistently yield such a value, while for weak measurements without postselection it is just a rare error and repetitions will not show a trend towards such a value.

As in this thesis the concept of the weak value can be fully addressed in standard quantum mechanics, but may as well be accessed from any approach to quantum measurement theory [46].

An opposing interpretation from the one above is given by the two-state vector formalism (TSVF). It is a time-symmetric reformulation of quantum mechanics, which is closely related to the concept of PPS systems and weak values. According to the TSVF the most complete description of a quantum system is given in terms of the preselected and postselected state vector, or more generally density matrix [6]. Both states are thought to evolve independently in opposite directions of time, where forward is defined as the direction of increasing entropy [6]. The two boundary conditions and therefore the two associated wave functions are seen as equally important for the quantum system in between. That is, it is influenced by both of them. Proponents of this approach claim that it facilitates the computational treatment of weak values and provides an intuitive interpretation of strange quantum effects [7].

3.7 Comparison with eigenvalue and expectation value

As the interpretation of the weak value of an observable may still considered to be unclear, we investigate the quantity from an operational point of view. In particular we are interested in how its behaviour compares with other - ordinary - quantities, as the eigenvalue and the expectation value of an observable. To this end we choose the closeness of the pointer quantum states, referring to the respective object quantities, as a criterion for similarity. That is, the pointer state obtained for an eigenvalue is to be compared to that obtained for a numerically equal weak value as well as to that obtained for a numerically equal expectation value. The proximity of two quantum states shall be expressed in terms of the Bures angle, as introduced in section 2.3.

3.7.1 General relations for arbitrary systems

The Hamiltonian of interaction between object and pointer system shall be given as in 2.7. For the situation when initially the object system is in an eigenstate of $\hat{A}$ with eigenvalue a, the pointer state, initially given by $|\phi_0\rangle$ and its probability distribution will be shifted according to that eigenvalue as a result of the interaction, while remaining undisturbed. Then the pointer state, labelled with the subscript e for eigenvalue, reads

$$|\phi_e\rangle = \mathrm{e}^{-\frac{i\epsilon g}{\hbar} a\hat{X}} |\phi_0\rangle \tag{3.24}$$

irrespective of post-selection. When the pointer state describes a weak value A_w, which numerically equals the eigenvalue a, but neither pre- nor postselected state are the corresponding eigenstate, it reads

$$|\phi_w\rangle = \mathcal{N}\langle\varphi|\,\mathrm{e}^{-\frac{i\epsilon g}{\hbar}\hat{A}\hat{X}}\,|\phi_0\rangle|\psi\rangle \tag{3.25}$$

as in Eq. (3.2) above. The Bures angle between $|\phi_e\rangle$ and $|\phi_w\rangle$, expanded in powers of ϵg with the normalization factor taken into account, reads [47]

$$D_A\left(|\phi_e\rangle, |\phi_w\rangle\right) = \arccos|\langle\phi_e|\phi_w\rangle| = \left|(A^2)_w - a^2\right|\sqrt{\langle\hat{X}^4\rangle_0 - \langle\hat{X}^2\rangle_0^2}\,\frac{\epsilon^2 g^2}{2\hbar^2} + \mathcal{O}(\epsilon^3 g^3) \tag{3.26}$$

Noticeable, the first order in ϵg vanishes. For the situation when the pointer state comprises the expectation value of $\hat{A}$, $\langle\hat{A}\rangle$ is assumed to be numerically equal to a. The initial object state is a superposition of eigenstates, namely $|\psi\rangle = \sum_{i=1} c_i|a_i\rangle$. After the interaction the systems are entangled and the reduced density matrix of the pointer system, denoted by the subscript ex, is given by [47]

$$\sigma_{ex} = \sum_{i=1} |c_i|^2\,\mathrm{e}^{-\frac{i\epsilon g}{\hbar}a_i\hat{X}}\,|\phi_0\rangle\langle\phi_0|\,\mathrm{e}^{\frac{i\epsilon g}{\hbar}a_i\hat{X}} \tag{3.27}$$

recalling from 2.11. Computing the Bures angle yields [47]

$$D_A\left(|\phi_e\rangle, \sigma_{ex}\right) = \arccos\left(\sqrt{\langle\phi_e|\sigma_{ex}|\phi_e\rangle}\right) = \Delta A\Delta X_0\epsilon g + \mathcal{O}(\epsilon^2 g^2), \tag{3.28}$$

where the first order does not vanish provided the initial pointer state is not an eigenstate of $\hat{X}$ and the object state not an eigenstate of $\hat{A}$. As a consequence of applying this measure, the change corresponding to a weak value scales with higher order of the small parameter with reference to the eigenvalue than the one attributed to the expectation value. Equivalently, the overlap of the weak value state with the eigenvalue state is greater than that of the expectation value state with the eigenvalue state. Therewith the object system weak value behaves more similar to an eigenvalue than to an expectation value in regard to its action on the pointer system. This subject is discussed in reference [47], which claims that the weak value behaves similar to an eigenvalue even if the weak value is such that its numerical value cannot be achieved by an eigenvalue, i.e. it exceeds the spectrum of the observable or takes on a complex number. In the latter case the numerically equal reference eigenvalue is only virtual. In the limit of vanishing $\epsilon^2 g^2 \Delta X_0^2$ the object system described by the weak value affects the pointer system as if it were described by an eigenvalue with corresponding eigenstate. As a consequence we suggest that in the weak limit the object observable in the interaction Hamiltonian of weak PPS measurements may be replaced with its corresponding weak value [47].

3.7.2 Conceptual implementation

The above expressions are implemented via a polarization-based experiment. In particular the comparison is realized by means of an interferometer containing the states under study in the respective interferometer arms. The measure is represented by the interference quality of the eigenvalue case with the weak value case as well as with the expectation value case. The connection between the visibility and the Bures angle between quantum states is possible by the relation given in (2.60), namely $D_A = \arccos(V_{\max})$.

The object observable $\hat{A}$ is represented by the Pauli matrix $\hat{\sigma}_z$ of a photon, while the input pointer observable $\hat{X}$ is chosen as its momentum. The initial pointer state is effectively the same as in 2.1.2, i.e.

$$\phi_0(q) = \left(\frac{1}{\sqrt{2\pi(\Delta Q_0)^2}} \, \mathrm{e}^{-\frac{q^2}{2(\Delta Q_0)^2}} \right)^{\frac{1}{2}}, \tag{3.29}$$

realized by one dimension of the transversal position of a collimated Gaussian beam. As a polarization system contains only two eigenstates with eigenvalues $+1$ and -1, a third fictional one has to be conceptualized to be able to consider all cases. This fictive eigenvalue is 0. The initial object state reads

$$|\psi\rangle = \frac{1}{\sqrt{2}}(|H\rangle + |V\rangle) = |P\rangle. \tag{3.30}$$

The interaction is modelled by a birefringent crystal, which couples the polarization to the momentum upon tilting. This translates to a mean transverse position shift, which is not of interest here, because we assume it to be equal in all cases. The set-up is adjusted such that the mean displacement caused by the crystal is compensated and therewith the object system is described by the σ_z operator. The reference case, where the eigenvalue is zero, corresponds to no interaction at all. The three cases are realized by the following settings:

(i) eigenvalue 0: the object state stays as it is, as realized in the reference arm of the interferometer by the absence of any interaction.

(ii) weak value 0: this is achieved with the birefringent crystal in between the pre- and postselection, which are carried out by P-polarisers.

(iii) expectation value 0: the pre-selected P-polarised state is followed by the birefringent crystal, without postselection.

The cases (ii) and (iii) are embodied in the second arm of the interferometer, called *test arm*. Depending on the case studied the polariser which defines the post-selection has to be taken in or out.
To illustrate the conceptual implementation the schematic set-up is shown in Fig. 3.4, while for a detailed discussion of the actual realization of the interference experiment it is referred to the next chapter.

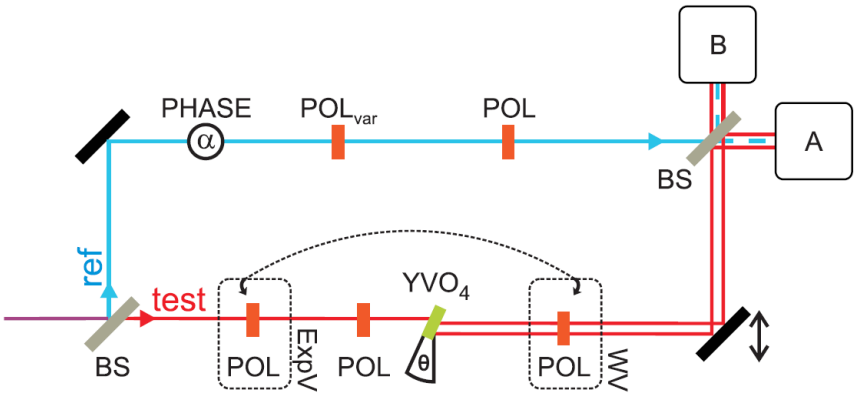

Figure 3.4: Schematic of the conceptual implementation of the interference experiment [47]. Shown is the reference and the test arm, which prepare the different pointer states. Depending on the case studied the polarisers in the test arm have to be adjusted. By varying the relative phase, denoted by α, the intensity is being modulated.

With this the pointer state corresponding to (i) is

$$\phi_e(q) = \phi_0(q), \tag{3.31}$$

the one corresponding to (ii) is [47]

$$\phi_w(q) = \mathcal{N}\left(\mathrm{e}^{-\frac{(q-ge)^2}{4(\Delta Q_0)^2}} + \mathrm{e}^{-\frac{(q+ge)^2}{4(\Delta Q_0)^2}}\right), \tag{3.32}$$

while the pointer state corresponding to (iii) is [47]

$$\sigma_{ex}(q) = \int \mathrm{d}q\,\mathrm{d}q' \,\frac{1}{2\sqrt{2\pi}\Delta Q_0}\left(\mathrm{e}^{-\frac{(q+ge)^2+(q'+ge)^2}{4(\Delta Q_0)^2}} + \mathrm{e}^{-\frac{(q-ge)^2+(q'-ge)^2}{4(\Delta Q_0)^2}}\right)|q\rangle\langle q'| \tag{3.33}$$

According to the general result Eq. (3.26), the Bures angle between the eigenvalue and the weak value state is given by

$$D_A\left(|\phi_e\rangle, |\phi_w\rangle\right) \approx \frac{\epsilon^2 g^2}{4\sqrt{2}(\Delta Q_0)^2}, \tag{3.34}$$

while the Bures angle between the eigenvalue and the expectation value reads

$$D_A\left(|\phi_e\rangle, \sigma_{ex}\right) \approx \frac{\epsilon g}{2\Delta Q_0}, \tag{3.35}$$

according to Eq. (3.28). The linear and quadratic approximations made are compared to the exact scaling functions in Fig. 3.5. For small values of $\frac{g\epsilon}{\Delta Q_0}$ the former resemble the

latter well. To experimentally check both expressions, (3.34) and (3.35), the visibility in

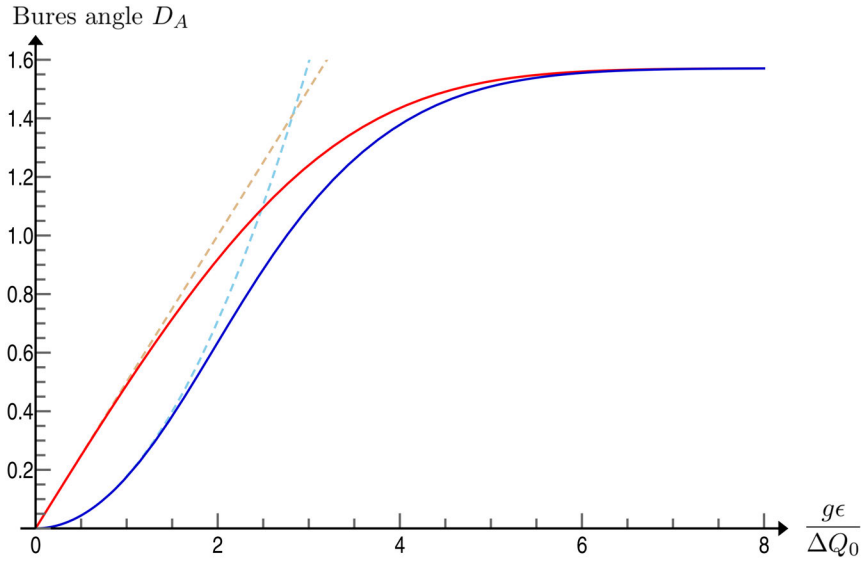

Figure 3.5: Theoretical scaling behaviour in terms of the Bures angle. For small interaction strengths the scaling behaviour is to a good approximation linear in the expectation value case (red) and quadratic in the weak value case (blue).

the interferometer has to be maximized in each case. The scaling behaviour is shown by varying the interaction strength ϵg, which is realized by tilting of the crystal, under the constraint of staying in the regime of weak interaction and linear pointer response. The theoretical graphs are shown in Fig. 3.6 in terms of the Bures angle and in Fig. 3.7 in terms of the visibility.

There the interaction strength is narrowed down to the range relevant in the experiment. The difference in scaling is clearly visible in both figures.

In essence the different scaling behaviour can be explained by the difference in the loss of coherence dependent on the interaction strength. If the object system is in an eigenstate it is not influenced by the interaction with the pointer, irrespective of its strength, which is represented by the constant line in Fig. 3.7. If the object system is described by an expectation value its state gradually transforms towards an incoherent mixture. This is counteracted, if the object system is described by a weak value, where its state is only disturbed comparably little over the range of a weak interaction strength. This means that the act of postselecting, which dis-entangles the object system from the pointer system, enables to some extent restoring of coherence.

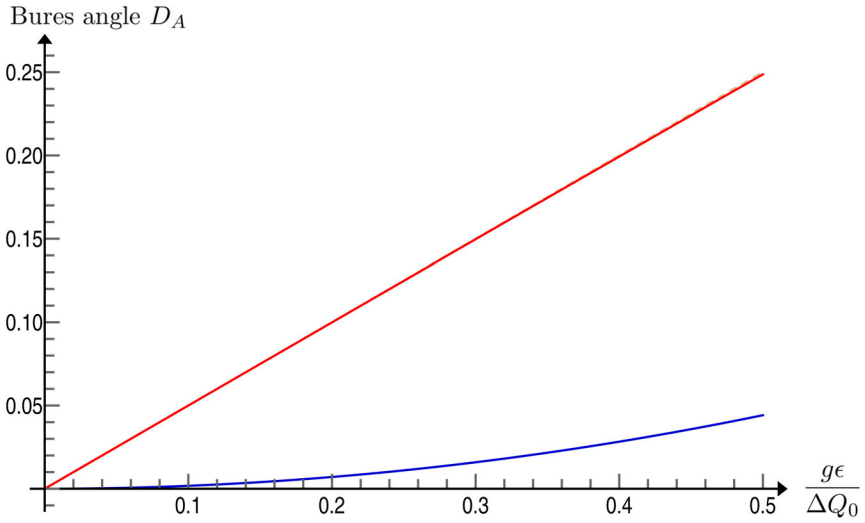

Figure 3.6: Theoretical scaling behaviour in terms of Bures angle, where the expectation value case (red)changes faster than the weak value case (blue).

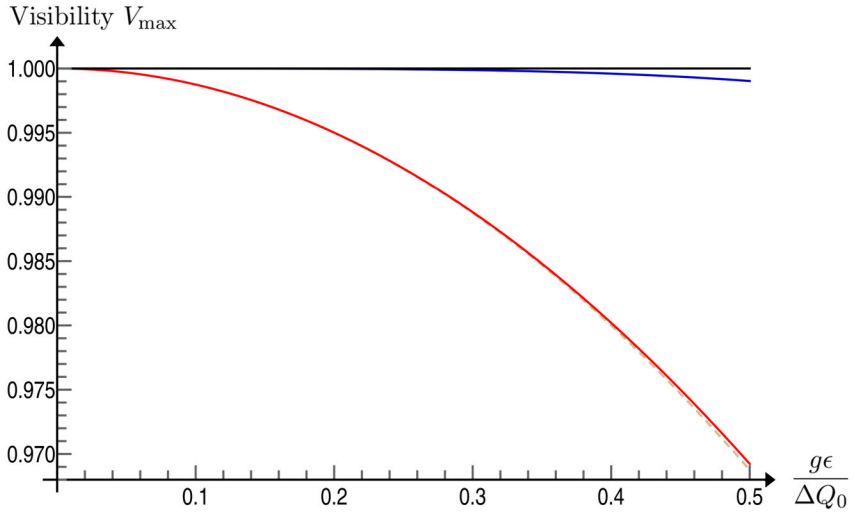

Figure 3.7: Theoretical scaling behaviour in terms of visibility, where the weak value case (blue) deviates only little from the constant reference line, which represents the eigenvalue case, while the expectation value case (red) drops considerably.

4 Material and methods

4.1 Experimental set-up

A schematic of the experimental set-up is displayed in Fig. 4.1. It shows the set-up for the beam preparation and the interference experiment, which will be explained in the following two sections. Fig. 4.1 also shows the scanning optical cavity, which is one of the methods used to optimize the experimental conditions in order to achieve maximized visibility, which is required for the successful realization of the experiment. This and other applied methods will be discussed in section 4.1.3.

4.1.1 Beam preparation

At the very outset comes the preparation of the laser beam. The laser set-up contains an external optical grating, mounted in a Littrow configuration as described in reference [36]. The laser system is placed in a thermoconductive mounting, grounded on a bottom panel, which comprises a thermoelectric cooler with a thermistor sensor. The infra-red laser diode is followed by an aspheric collimating lens. The outcoming laser beam then propagates to a diffraction grating, which acts as a dispersive element. While the first order of diffraction is retro-reflected and fed back into the laser diode, the zeroth order fraction is used as output beam. The collimating lens has to be adjusted such that the focal point of the beam is at a large distance, in our case about 4 m. With increasing distance the spot diameter of the back-fed beam at the laser diode decreases and therefore the coupling into the diode is more efficient [40]. If the spot size is small, however, one has to be more careful with the alignment such that it overlaps the diode cross-section [40].

The grating is aligned in an iterative manner using two degrees of freedom, i.e., horizontal and vertical tilting, such that the laser operates at a single mode. To ensure that the retro-reflected beam meets the laser diode, the grating is tuned such that both output beams, the primary and the secondary reflection from the grating, coincide. When they overlap the output intensity is significantly enhanced. The horizontal degree of freedom is tuned such that the lasing threshold is minimal. The threshold current is lowered by further aligning the grating correspondingly. This procedure allows for the selection of a single longitudinal mode for lasing.

Two laser systems were used for measurement data acquisition. The original and primarily utilized laser diode, Sanyo DL7140-201S, with a typical lasing wavelength of 785 nm and a typical output power of 70 mW in continuous wave operation, was already ready for use. In the course of the workings shortcomings concerning the mounting of the laser system

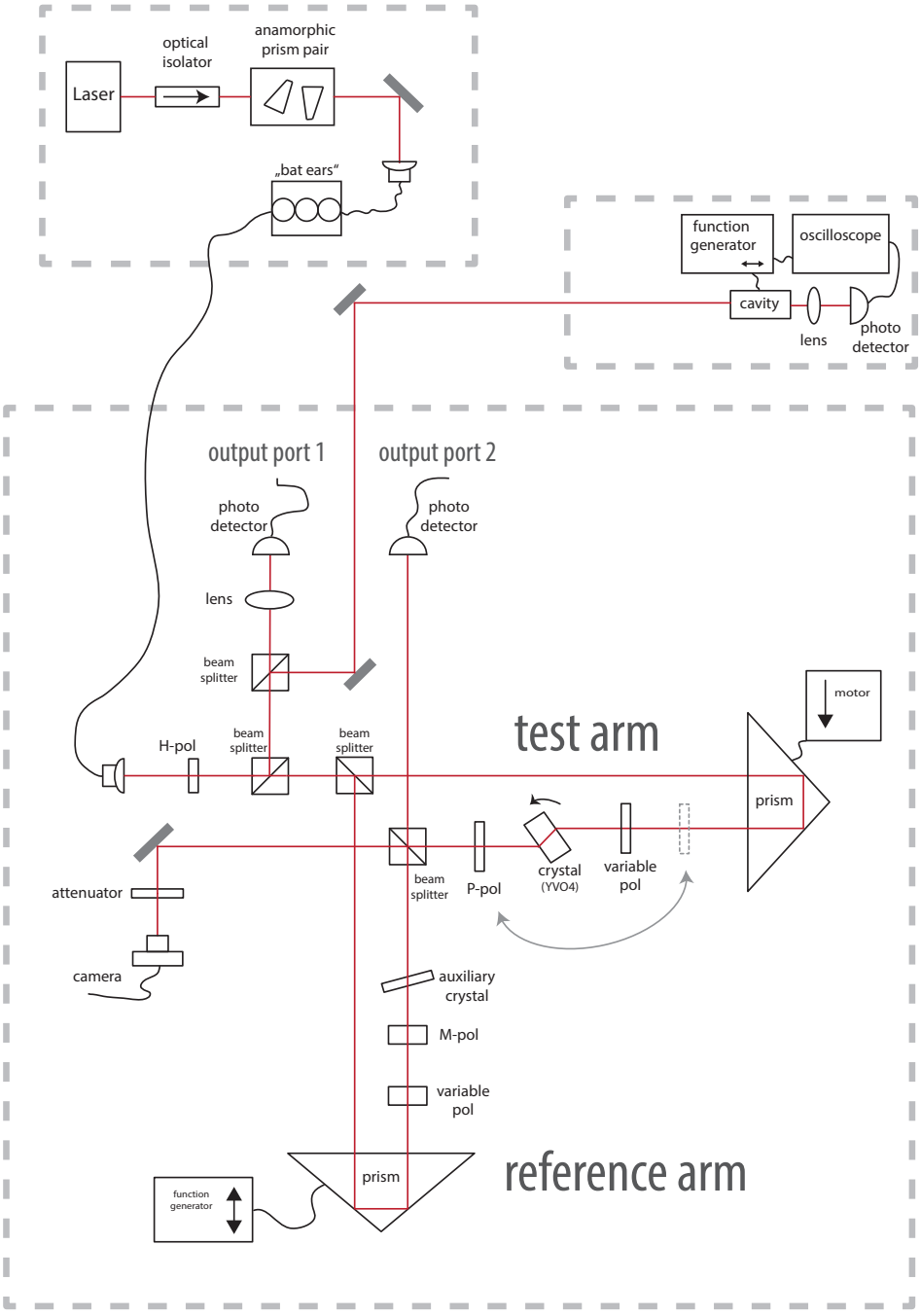

Figure 4.1: Experimental set-up. At the top the beam preparation is depicted. The main part shows the set-up for the interference experiment, where the test and the reference arm prepare the quantum states which are to be compared. At the top on the right the set-up for the scanning optical cavity is displayed.

had to be remedied, such as worn out tension springs and the adjustment screw. In this regard also the above mentioned laser diode was replaced by a newly set-up laser-diode of the same typical lasing wavelength, namely L785P090 Thorlabs.

The output laser beam propagates first to an optical isolator, which lets light travel through in one direction, but blocks it in the opposite direction. The purpose of this device is to prevent unwanted reflections from subsequent optical components back into the laser system, which could alter the laser emission by feedback or cause damage. Its functional principle is based on the Faraday effect, explained in section 2.2.4.

Next the beam passes an anamorphic prism pair, which is supposed to transform the elliptical beam profile, which is a result of the laser diode semiconductor structure, into a concentrically symmetric beam profile. This is done by expanding the beam diameter in only one dimension to eliminate the ellipticity [15].

Via a mirror the beam is then deflected towards a fibre collimator, which comprises a collimating lens and a connection to an optical fibre. Coupling the beam requires adjusting the tip and tilt set screws on the mounts of the mirror as well as of the collimator itself together with matching the focal plane the lens such that the maximum amount of laser power gets into the fibre, which is controllable by means of an attached power meter. This process of iteratively optimizing the alignment to reach a specific point in space with a specific angle, is called 'walking the beam' [3].

The beam is then transmitted via an optical single mode fibre (SMF), where only a single transverse mode is supported, to obtain a TEM_{00} mode in the interferometric set-up. The light is guided by the principle of total internal reflection. To this end the fibre is composed of a dielectric core, which is surrounded by a cladding material with a lower index of refraction. At the end of the fibre the light is coupled out again with a fibre collimator, 60FC-0-M12-10 Schäfter & Kirchhoff GmbH. In between, fibre polarization controllers, so-called *bat ears*, which are capable of changing the polarization, are set such that after an additional horizontal polariser the out-coupled power is on the order of a few mW.

The fibre collimator was selected under the premise that the output provides the best accordance with a symmetric Gaussian intensity distribution, which was checked at different positions by means of a beam profiling camera, WinCamD, analysed with the software from the manufacturer DataRay Inc. The laser beam was collimated parallel to the optical table by use of iris diaphragms and the beam profiling camera over a distance of approximately 3 m.

4.1.2 Set-up for the interference experiment

The beam first passes a horizontal polariser to start with a well defined polarization. Next it is divided by a non-polarising beam splitter, which reflects half of the light incident and transmits the other half. The reflected part is focussed by a converging lens onto a photo diode (for clarity henceforth called output port 1), which converts impinging light into electrical current signal. The detector is employed to monitor the fluctuation in overall laser intensity. The transmitted part is further utilized for the interference experiment.

For better handling, the set-up is designed as a modified Michelson interferometer with retro-reflecting prisms, corresponding to a folded Mach–Zehnder interferometer. Therefore two beam splitters (BS) are used, which are placed in separate mountings on translation stages because a joint mounting did not offer enough options for adjustment. They consist of a glass plate with a reflective dielectric coating on one of the sides. Both were chosen for their properties of being approximately 50:50 for all polarizations. For clarity one arm of the interferometer is called 'test', while the other one is named 'reference'. To accomplish a continuously varying phase difference between the arms of the interferometer the path length of the reference arm is continuously scanned. For this purpose a piezo element is connected to the prism of the reference arm, which is actuated by a function generator producing a triangular ramp signal, such that the prism moves back and forth over a few micrometers. In both arms the optical components defining the quantum states for the measurement are placed in the retro-reflected beam path to avoid unwanted phase shifts from the prisms (Goos-Hänchen effect). Optical components involved in the set-up are calibrated and cleaned with collodion. Polarisers are from Codixx AG. Motors connected to components help to automatise procedures whenever useful. Interference is measured at one of the interferometer ports (output port 2) via a second photo diode (PD) detector. Although the two detectors have different capacities, it is made sure that each of the used resistors is lower than the resistors of readout instruments.

Test arm

The test beam is operated with two different settings, one for the expectation value and one for the weak value. The sequence of components both have in common are a motorised linear polariser, followed by a motorised birefringent crystal. The latter is yttrium orthovanadate (YVO4), a positive uni-axial crystal, which was discussed in section 2.2.4. All utilized motors exhibit slight mechanical vibrations at specific unstable motor positions. The motor which is least vibrating is chosen to actuate the crystal, which is most sensitive to instabilities. Furthermore the motors are always driven from the same direction to circumvent that possible backlash alters the desired motor setting. The prism in the test beam is motorised to automatically adjust its position to compensate the predicted mean displacement of the beam caused by tilting the crystal, where one step of prism movement causes a beam shift of $0.156\,\mu$m. In particular the calculated position is centred between the ordinary and extraordinary beam components, which are refracted by different indices. Thereby the location of the beam center of mass behind the crystal does not change irrespective of the tilting angle. The different configurations are P-polariser - crystal - P-polariser for the weak value setting and P-polariser - P-polariser - crystal for the expectation value setting. In the latter case the polariser, which is not to be used behind the crystal is instead placed in front of the other P-polariser to maintain an equal number of optical components and therefore balanced distortions by surface effects. In practice the motorized polariser is not exactly set to 45° linear polarization to account for a slight difference in transmission for horizontal and vertical component through the crystal. The automatic compensation of the polariser for each tilting angle of the crystal makes sure that

equal fractions of horizontal and vertical polarized light traverse the crystal. With varying beam displacement also the components in front of the crystal are displaced accordingly via translation stages to ensure that the beam impinges on the same surface spots for the whole measurement series.

Reference arm

The reference arm has to match the intensity of the test arm. Varying the intensity is achieved by means of a motorised polariser, followed by a set polariser. For controlling and balancing the intensities of the reference and the test arm, beam blocker tools are attached to each of the motorised polarisers, such that the arms may be automatically blocked one after the other.

The polarisation state of the reference arm has to equalize the one of the test arm at the location of output port 2. The polarization of the beam in the test arm is reflected by the beam splitter, such that the expected polarization is $-45°$ linear, i.e. minus. However, there arises an unwanted elliptical polarization component with the deflection. This is compensated for by means of an auxiliary YVO4 crystal with a thickness of $300\,\mu$m in the reference arm. The induced beam separation, which is undesired here, is negligibly tiny for the linear birefringent crystal of this length, while the phase shift induced by propagation through the crystal is sufficient to compensate the unwanted ellipticity. Depending on the laser wavelength, the tilting of the thin crystal has to be modified slightly, such that the polarization matches the one of the beam in the test arm.

Acquisition of data

The voltages of the two photo detectors are read-out via separate input channels of an analogue-to-digital converting usb-voltmeter, which is connected to a computer. To feed in data from the ramp signal driving the piezo element at the prism, the voltage output of the function generator is carried along via a third channel. All measured data are recorded together with an internal time-stamp of the read-out device, where the read-out rate is 100 Hz. The timing is consistent over all inputs. The results may either be displayed simultaneously in real time or automatically written to a file.

4.1.3 Applied methods

Spatial alignment

The beam paths should be collinear and of equal optical lengths. The aligning process to see interference involves walking the beam by adjusting both beam splitters and both prisms, which are also placed on translation stages, such that the beam splitters are always hit near the center. Vernier adjustment is done based on the image of the beam of a video camera, which is placed at one of the output ports of the interferometer. It is, in contrast to the human eye, capable of detecting infra-red light such that the interference quality may simultaneously be observed via a connected screen. Position mismatches and the resulting

local intensity deviations are difficult to detect by eye, while angle mismatch becomes apparent by swiping interference patterns or fringes, exemplary displayed in Fig. 4.2. To

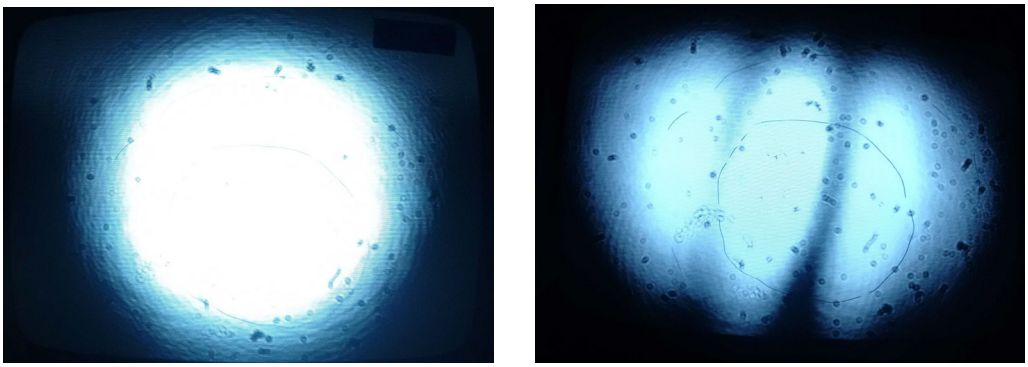

(a) Overlapping beams (b) Angle mismatch

Figure 4.2: Exemplary recordings of spatial alignment. The aim is to spatially overlap the two Gaussian modes without angle or lateral mismatch. (*a*) shows spatially well overlapping beams, while in (*b*) there is an angle mismatch present.

accurately correct for the difference in path lengths another laser source emitting pulsed radiation is temporarily coupled into the set-up. The former is a titanium-sapphire laser, which generates short pulses with duration of 130 fs at a wavelength of 780 nm. Due to its broad spectrum and short coherence length the interference pattern is much more sensible to distance variation, which makes it possible to precisely equalise the path lengths of both arms. All steps are repeated when necessary, especially after inserting optical components, which may alter angle, position and optical path length of the beam propagation.

Phase preserving crystal angles

The crystal induces a phase between horizontal and vertical polarization component, which changes progressively with its effective thickness upon tilting. Therefore the tilting angles, where the polarization of the incident beam stays equal, have to be found, which constitute usable settings for the measurement protocol. The intensity is recorded when varying the angle of the crystal, while the reference arm is blocked. The preselection polarization is $-45°$ (M), while the postselection polarisation is $+45°$ (P). The angle positions where the intensity is minimal yield the settings, where the polarization state is effectively preserved after the crystal.

Matching the polarization via state tomography

For measuring polarization a motorised quarter-wave plate and a motorised polariser are placed behind one another in output port 2. With respective angle settings it is possible to project a given state onto arbitrary states. The method of choice to match the polarisations of both arms involves finding the state orthogonal to the state of the test beam by varying

the orientation of the quarter-wave plate and the polariser at output port 2. The test arm is in the configuration of the weak value, i.e. with a P-polarized postselection such that the effect of the beam splitter can be exactly compensated. The polarization state corresponding to the angle setting which cancels the test arm intensity best is then set in the reference arm. The other arm is blocked in the respective alignment steps. By manually tuning both the set polariser and the thin crystal in the reference arm, again the state which gives the best extinction ratio is prepared. Thus the reference polarization is set to precisely meet the one of the test arm. This is also true for the expectation value setting because for the interference experiment the crystal is set to angles where the polarization stays equal.

Spectral analysis via scanning optical cavity

Monitoring the spectral distribution of the beam is accomplished by means of an optical cavity, which is inserted in the set-up at output port 1 via an additional beam splitter. The confocal cavity consists of two plano-concave reflecting mirrors, separated by a distance d, which equals the curvature radius. That means a resonant mode traverses the cavity twice before it overlays its path, i.e. the mode spacing becomes degenerate according to $\Delta\nu_{\mathrm{confocal}} = \Delta\nu_{\mathrm{FSR}}/2$.

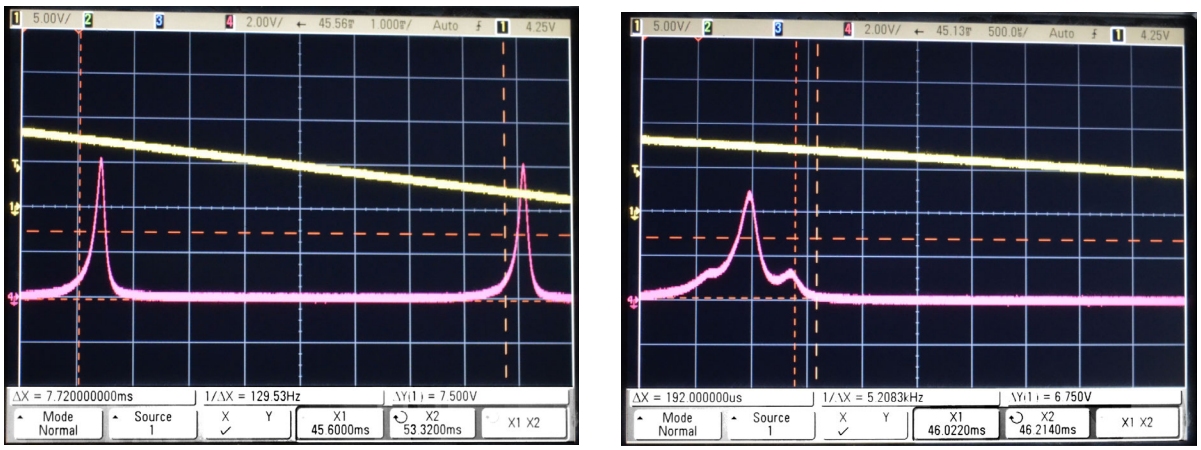

(a) Single-mode (b) Multi-mode

Figure 4.3: Exemplary recordings of the spectral distribution from an oscilloscope display using a scanning optical cavity. The aim is to choose the laser current such that the laser operates on a single longitudinal mode

To approximately match the transverse mode of the incoming beam to the one of the cavity, a plano-convex lens focusses the incoming beam into the cavity. The proper set-up of the cavity requires adjusting position and angles of the two mirrors such that their focal points coincide at the center of the cavity [44]. Thereby the transmission of the $\mathrm{TEM}_{0,0}$ mode is maximized, while that of other cavity modes is minimized. After alignment a photo

diode is placed behind the cavity. One of the cavity mirrors is attached to a piezo element, which is driven by a connected function generator producing a triangular ramp signal. To see the scanning of the spectrum of the beam, both, the detector and the function generator are read out via an oscilloscope. One can trigger it to display the detected voltage against the time it takes to traverse half of the spectral range, which is about $\Delta\nu_{\text{confocal}} = 750\,\text{MHz}$ for a cavity length of 10 cm. If the laser operates in single-mode, the oscilloscope display shows only one maximum. From reading of the time intervals of $\Delta\nu_{\text{confocal}}$ and of the FWHM of the peak its linewidth may be deduced to maximally 19 MHz. By monitoring the spectrum the current can be appropriately chosen, as depicted in Fig. 4.3.

4.2 Measurement protocol of interference experiment

The measurement protocol to measure the interference involves the optimization of various parameters, mostly executed automatically. Before starting the experiment the set-up is spatially aligned by hand, i.e. the overlap is optimized with regard to position and angle. The laser current is set such that the output power is stable over time and the beam spectrum is characterized by single mode operation. The main input parameters are crystal settings with equal polarization. Starting from the input parameters for a given crystal setting the program successively tunes the crystal angle for better agreement of polarization, the position of the prism for better lateral beam overlap and the reference arm polariser for better intensity equalizing. The motorized preselection polariser in the test arm is automatically set according to the crystal angle. All these parameters are optimized with the aim of maximizing the visibility, i.e. the program shortly measures the visibility for a range of tested configurations and chooses the best setting. This procedure is first performed coarsely, i.e., in greater intervals of change, then finely. In between the program stops its loop, so that the experimenter may realign the set-up manually. In particular the optical components in front of the crystal are shifted accordingly and - if possible - the overlap is optimized with the degrees of freedom, which are not accessible with motors. As this is done by eye, i.e., with the help of the camera, the program incorporates the option of checking the visibility in between for monitoring purposes. Additionally the prism in the reference arm is moved to compensate for low temporal coherence in the case of the misaligned laser system. After the final fine-tuning run, the actual measurement is carried out, by recording the output intensity over a longer time interval. This last step is repeated a few times for a given crystal setting to check the reproducibility of the fine-grained optimizing procedure. This loop successively passes through all the input settings.

4.2.1 Data evaluation

The data of the interference experiment are evaluated in the following way. To properly account for possible laser intensity fluctuations over time, the interference signal from output port 2 is normalized to the signal from output port 1, where the internal background

of each photo diode - noise in the absence of laser photons - is subtracted from the respective signal. The maxima and minima of the resulting intensity modulation over time are then separately fitted to parabolas within each ramp interval, where turning points are excluded. Thereby maximal and minimal values are determined, from which the visibility value is computed. A single mean visibility value for a certain crystal tilting angle is calculated out of several maximal intensities obtained in consecutive measurements. Due to, e.g., mechanical instabilities of the motor controlling the crystal, some data sets are found to be unreliable. In particular the measured data is checked for technical sources of error in an unbiased manner. Furthermore the evaluation script outputs a warning if the fit quality is not above a certain threshold.

5 Experiments and discussion of results

This chapter summarizes the measurements performed and discusses their results. This includes the characterization of the polarization, the spectral, temporal and spatial properties and of the stability of the output power of the laser beam to determine the quality of interference, as described in section 5.1. In addition to desired effects it is required to quantify also undesired effects one is faced with within the experimental set-up in order to either compensate them if possible or to account for them as sources of error. Section 5.2 focusses on measurements concerning the properties of the birefringent crystal in the test arm because it is the crucial element for the experiment. In the following main section 5.3 the results of the interference experiment are presented and analysed. The chapter concludes with the comparison of the experimental scaling behaviour to the theoretical one in section 5.4.

5.1 Beam properties

5.1.1 Characterization of the spatial distribution

In practice the spatial distribution differs from the idealized circular symmetric Gaussian beam profile. These deviations are visible in Fig. 5.1, where the beam profile of the test arm was recorded with a beam profiling device at output port 2.

The distribution is essentially Gaussian, in particular the beam profile is not substantially disturbed by the various components, in particular the birefringent crystal, but keeps its shape during propagation. However, local deviations from an ideal profile lower the spatial coherence of the two beams. Using a beam profiling camera the waist radius W_0 of the collimated beam is determined to about $813\,\mu$m from intensity profiles measured at several distances without components. This corresponds to a Rayleigh length of about 2.7 m in air, which is effectively reduced, when the imperfect beam quality is accounted for. Still, for the smaller length scale of the set-up the beam can effectively considered to be collimated. The waist radius is needed for computing the magnitude of the interaction strength, given by $\epsilon g \Delta Q_0$, via the relation $W_0 = 2\Delta Q_0$ for the comparison of the experimental with the theoretical scaling behaviour.

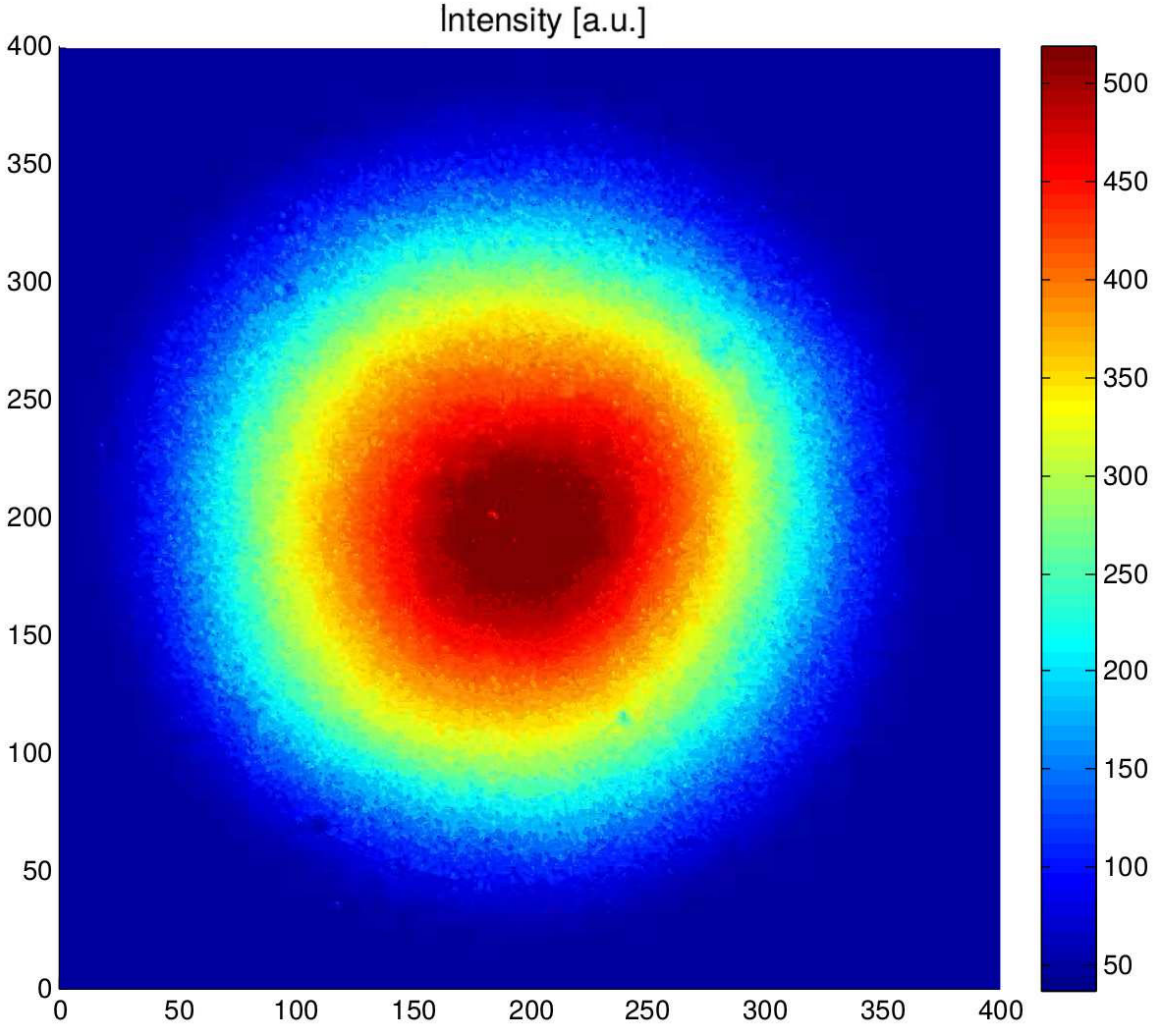

Figure 5.1: Beam profile in test arm where the crystal was not tilted. The axis denotes the number of pixels, where each pixel has a width of 6.7 μm .

5.1.2 Characterization of the spectral distribution

Temporal coherence can be measured in terms of the coherence length l_c. In an interferometric set-up the latter may be defined as the displacement length z, where the visibility is reduced to $1/\sqrt{2}$ from its maximal value [30]:

$$V(l_c) = \frac{1}{\sqrt{2}} V(z = 0) \tag{5.1}$$

In the course of this thesis, l_c of the employed laser light was determined after observations seemed to imply an unexpectedly small coherence length. To measure l_c the maximum visibility is recorded for varying positions of the reference arm prism, which is manually displaced via a translation stage. During a measurement interval the phase difference is

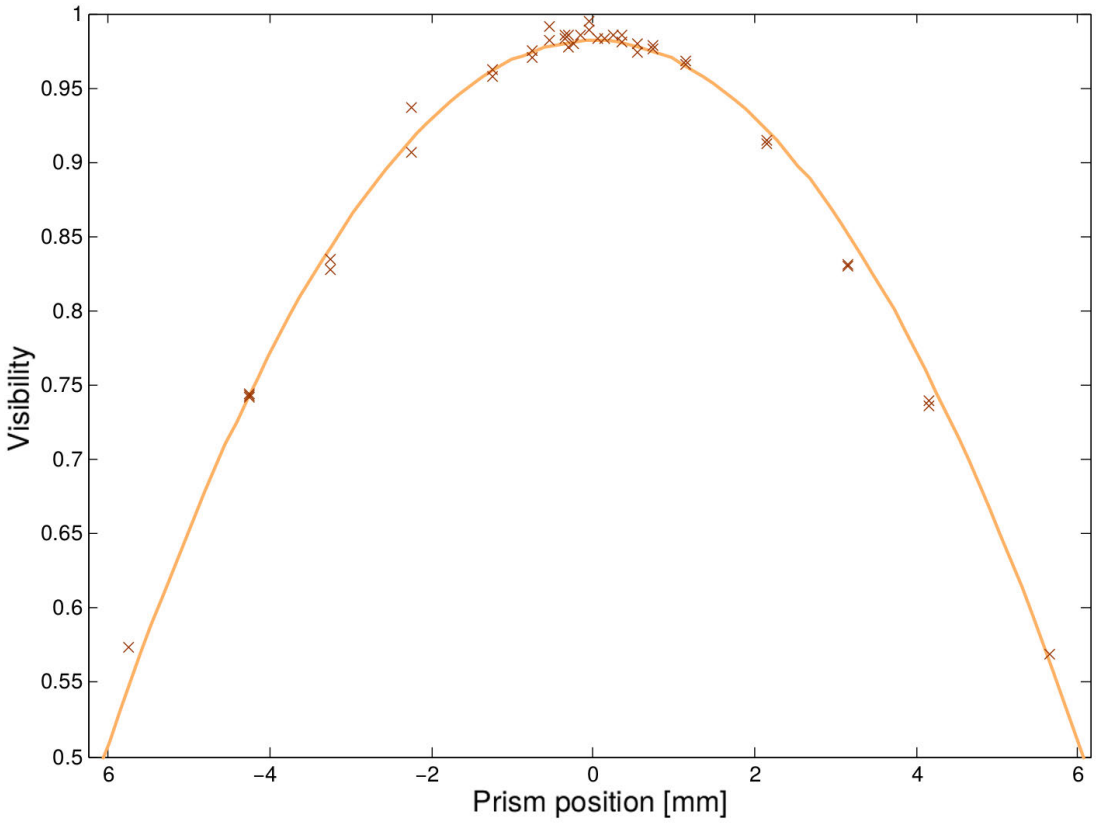

Figure 5.2: Measurement of the coherence length. Resulting visibility values for varying displacements of the prism in the reference arm. The set-up was optimized for a crystal tilting angle of 44.98°.

continuously modulated via the piezo element at the prism, which is regulated by the ramp signal given out by the function generator. Fig. 5.2 exemplary shows the resulting function for the setting, where the visibility is optimized for a crystal tilting angle of 44.9814°.

Evidently, a fast decrease of visibility with increasing displacement has been observed, such that $V(l_c)$ was reached for a displacement of approximately 5 mm only. This value was also reproduced with other crystal settings. As the coherence length l_c is inversely proportional to the linewidth $\Delta\lambda_{\mathrm{FWHM}}$ of the beam spectrum, a short l_c implies a broad $\Delta\lambda_{\mathrm{FWHM}}$, which in turn signifies low spectral coherence. The spectral distribution was measured by means of an optical spectrometer. While the peak wavelength may be deduced directly from Fig. 5.3, the resolution of the device is not sufficient to read off the exact value of $\Delta\lambda_{\mathrm{FWHM}}$ directly. For a peak wavelength of about 780.9 nm the linewidth is

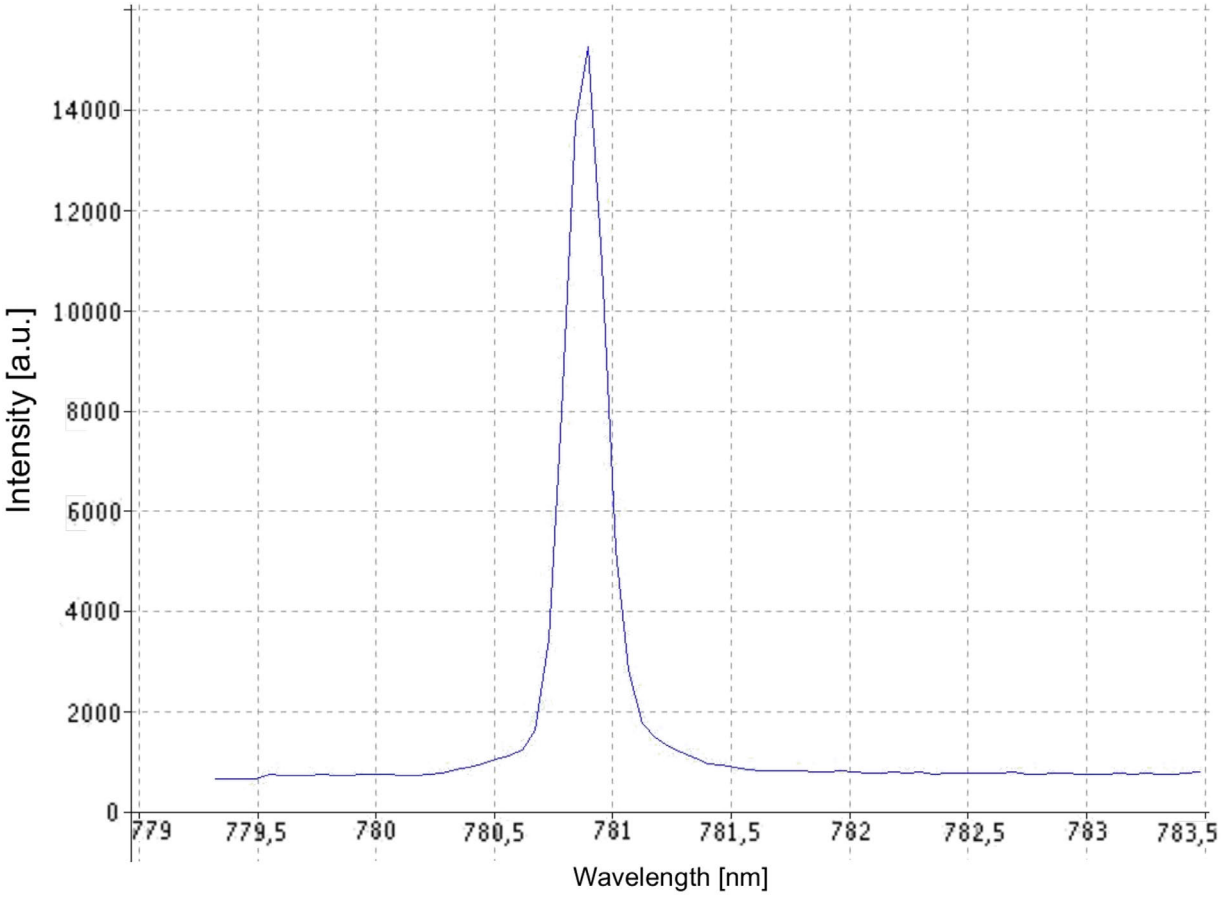

Figure 5.3: Measurement of the spectral distribution. The spectrum is peaked around a wavelength of 780.9 nm. The resolution of the spectrometer is not sufficient to detect a possible multi-mode shape.

calculated to $\Delta\lambda_{\mathrm{FWHM}} \approx 0.08\,\mathrm{nm}$ using Eq. (2.36). In the frequency representation this translates to a width of about 40 GHz. The reason for this relatively broad distributions is found to be the misalignment of the angle of the external grating of the diode laser, not ensuring proper feedback. With an assumed external resonator length of about 1.5 cm, the free spectral range of external modes is about 10 GHz, which means the laser operates in multiple modes simultaneously. A single mode linewidth, whose upper bound of about

19 MHz was determined with the scanning optical cavity, was realized with a newly set-up laser system, which ensured temporal coherence over the range of the set-up. Due to better resolution an optical cavity is used to monitor the spectral distribution for the interference experiment because the spectrum also changes with the current. The laser current is chosen such that the laser operates on a single longitudinal mode.

For most of the measurements presented in this thesis, performed with the original, misaligned laser system, the path lengths had to be balanced manually for different effective crystal lengths to maximize the visibility despite of the low temporal coherence.

5.1.3 Polarization balancing

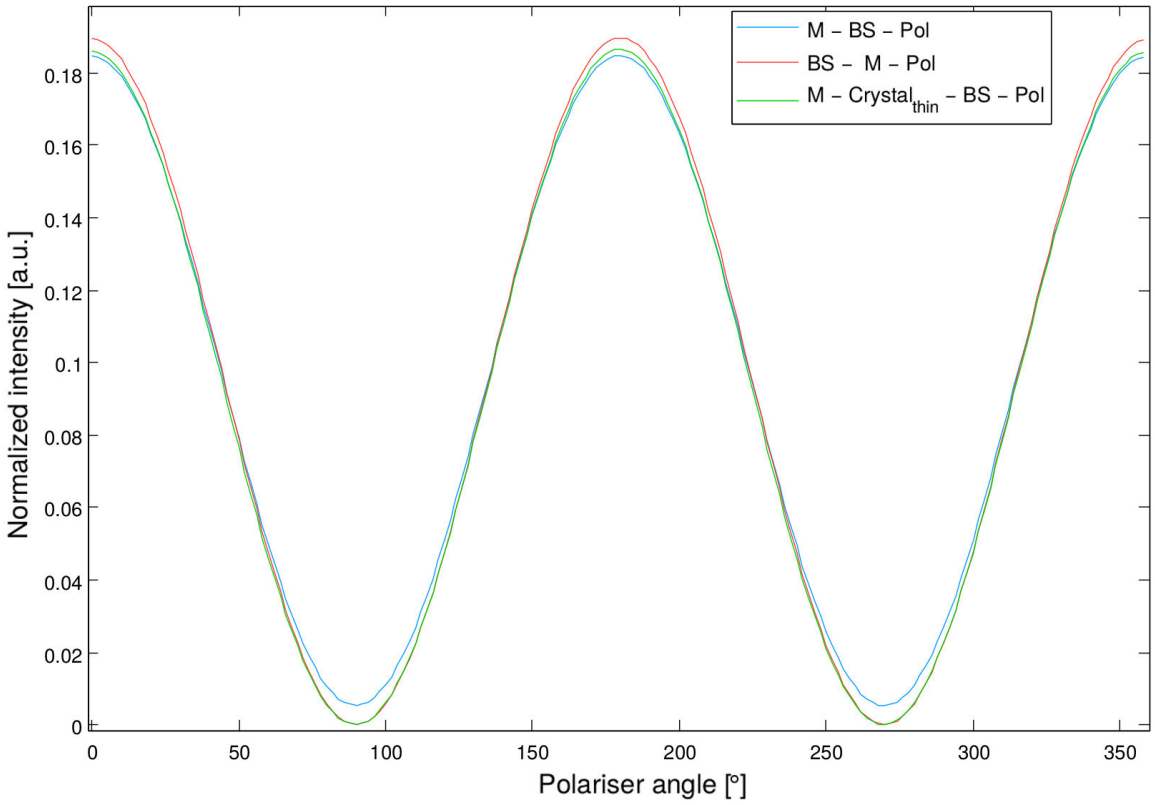

Figure 5.4: Quantifying the birefringence of the beam splitter in the reference arm. The linear polarization is scanned with an additional motorized polarized at output port 2. The contrast of the blue intensity modulation (visibility of 94.31%) is enhanced by the use of an additional thin crystal, which is placed in front of the beam splitter, denoted in green (visibility of 99.81%). For reference the M-polariser is placed next to the variable polariser resulting in an optimal contrast (red, visibility of 99.86%).

Maximal visibility also requires to equalize polarization in both interferometer arms at

the location of the second photo diode (output port 2). Conceptually this is implemented by separate projection onto the appropriate polarization state in each arm. The idealized setting comprises a minus-polariser in the reference arm and a plus-polariser as postsselection for the beam in the test arm because its polarization is reflected at the beam splitter. However, the beam splitter features slight circular and linear birefringence, which affects transmitted and reflected beam in an unequal manner. The effect becomes visible by rotating the polarization of an additional motorized polariser at the location of output port 2 when the respective set polariser is placed behind or in front of the beam splitter. Exemplarily shown in Fig. 5.4 is the difference in intensity modulation for the reference arm. The linear polarization rotation manifests itself in a tiny lateral displacement of the sinusoidal function, while the phase shift between horizontal and vertical polarization causes the modulation depth to decrease. The polarization of the reference arm is therefore matched to that of the test arm by a corresponding combination of a slightly rotated M-polariser and an auxiliary aligned crystal as described in section 4.1.3.

5.1.4 Output power

Due to various external and internal influences, the laser output power is subject to fluctuations, which add the actual interference modulation at output port 2. The monitoring photo detector at output port 1 serves for normalization according to

$$I = \frac{I_{\text{output port 2}} - I_{\text{background output port 2}}}{I_{\text{output port 1}} - I_{\text{background output port 1}}}, \tag{5.2}$$

where the background noise of each detector is subtracted. However this method can only cancel fluctuations to some extent. As the two detectors are not equal and operate with different capacities and resistors, they differ in their internal (dis)charging time, meaning that fast fluctuations might be averaged out by the slower detector. This becomes visible when fluctuations in the signal at op2 and op1 are not consistent with each other, i.e., appear only in one of them and therefore do not cancel by applying Eq. (5.2). Therefore for all measurements the laser current is tuned such that the output power is most constant. Interestingly, while there is always one setting of the current, where the laser operates stable, the other ones produce high frequency fluctuations in their output power, as can be seen in Fig. 5.5.

5.2 Crystal related measurements

5.2.1 Investigation of the beam deflection

The desired difference in displacement for the ordinary and the extraordinary beam is achieved by rotating the crystal around its optical axis, which is vertically aligned. In this way the latter stays perpendicular to the propagation direction $\vec{k}$ of the incident beam irrespective of the tilting angle. This ensures constant refraction indices, n_o and n_e. The

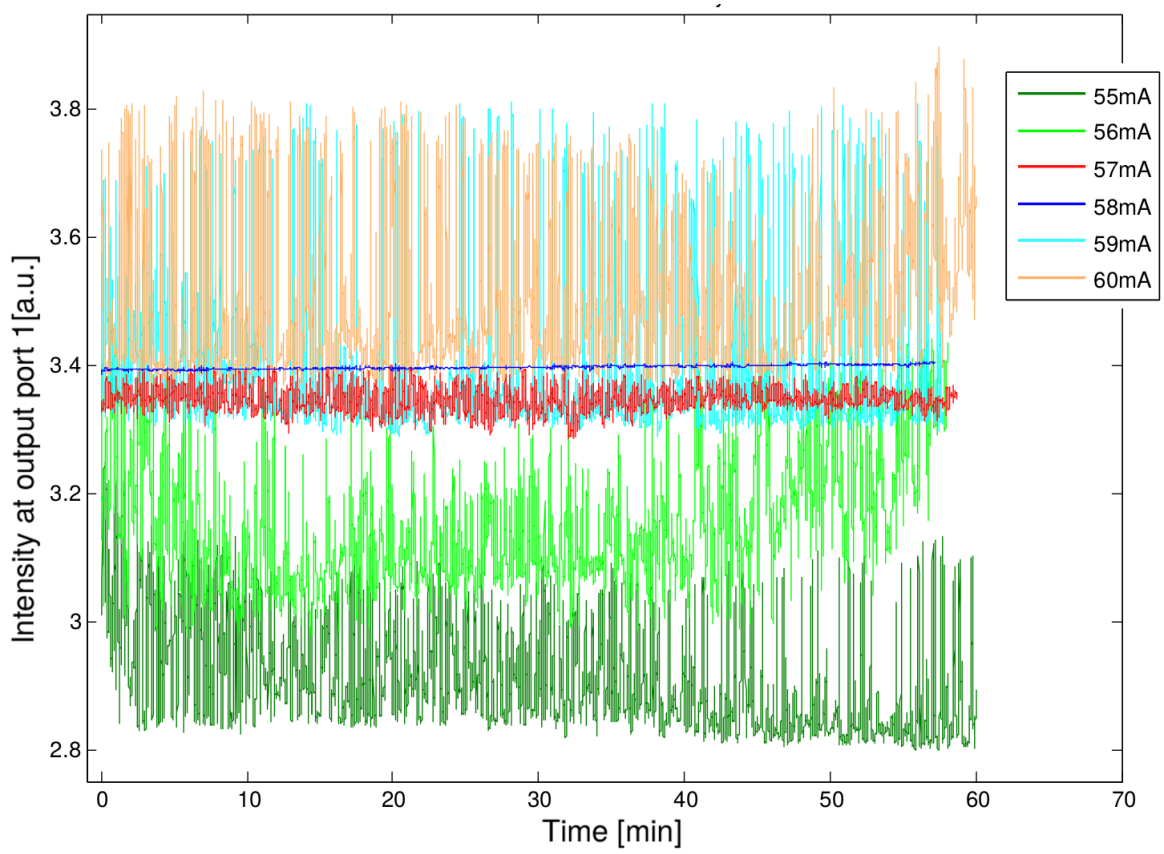

Figure 5.5: Output power, recorded at output port 1, for different settings of current, given in mA. The laser intensity is subject to fluctuations. For measurements the current is tuned such that the output is maximally stable over time.

angle of incidence, i.e., the tilting angle θ of the crystal, determines the refraction angles $\theta^{(o)}$ and $\theta^{(e)}$ according to Snell's law. This results in a spatial separation δx of the two beam components behind the crystal according to Eq. (2.43). The distance is experimentally obtained by separately recording the position of the beam for horizontal as well as for vertical input polarization for varying crystal angles. The useful angles are in the range of $[0°; 45°]$ since δx does not increase significantly for larger tilting angles. The beam profiling camera has a resolution of 1024×1024 pixels, where each pixel corresponds to $6.7\,\mu$m. From each measurement picture the beam centre is fitted to a Gaussian function, which takes into account the detected background noise. The so determined position values are given with 95% confidence intervals. The x coordinates of ordinary and extraordinary beams are further fitted by δx_e and δx_e from Eq. (2.43) to extract $d = 4529.6138\,\mu$m and $n_o = 1.973$, $n_e = 2.190$. The latter are in good agreement with the refractive indices obtained from the Sellmeier equation for a wavelength of 780 nm, namely 1.9738 and 2.1883. The resulting graph in Fig. 5.6 shows δx_o and δx_e as a function of the tilting angle.

The fitted parameters are implemented in the program for the measurement protocol,

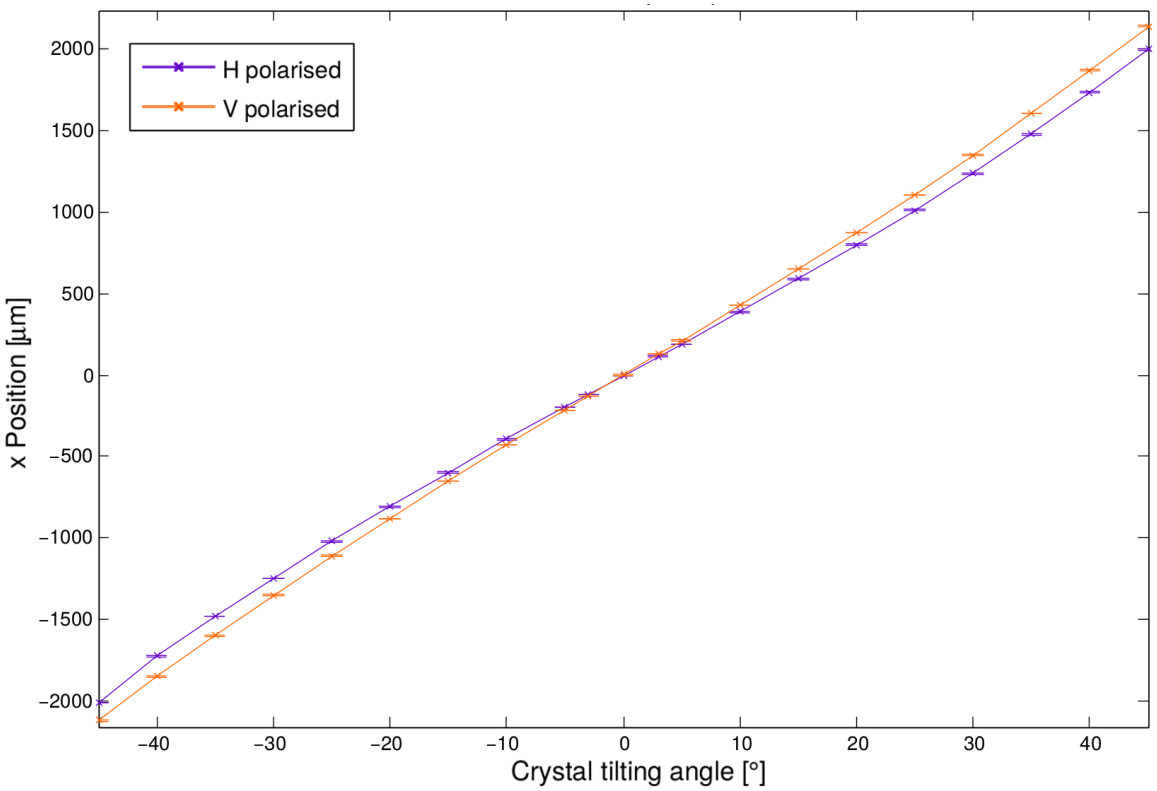

Figure 5.6: Beam deflection by the crystal, used for extracting the exact values of the crystal thickness d and the refractive indices n_o and n_e. The orientation of the optical axis is vertical, such that the ordinary beam is horizontally polarised, while the extraordinary beam is vertically polarised. The point of intersection may be used for an approximate calibration of the crystal angle.

such that the motorized prism is moved automatically to compensate the mean displacement of the whole beam $\frac{\delta x_e + \delta x_o}{2}$ for a given crystal angle. It can be driven in steps of $0.156\,\mu$m. At an angle of 45° the mean displacement is about $2042\,\mu$m, while the beam separation is only about $137\,\mu$m. By contrast, the y coordinates, plotted in Fig. 5.7, are supposed to stay constant for varying tilting angles. The beam height of both beam components is not perfectly constant, but varies about several μm. The difference in height for the H- and the V-polarization component is caused by the fact that the motorized polariser exhibits slight imbalance in its mounting, such that the beam transmission in the horizontal configuration does not exactly coincide in space with the one in the vertical.

In the interference experiment the preselection stays P-polarized in good approximation, or more specifically is adjusted only over a fraction of one angular degree (see section 5.2.5), such that this effect does not pose a problem. The same mounting instability can be seen in the reference arm, where the effect is much larger. Fig. 5.8 shows the position change of the beam center, when the motorized polariser is rotated over the full rotation of about 360°, which causes rather large spatial deviation. Encircled in red is the range typically

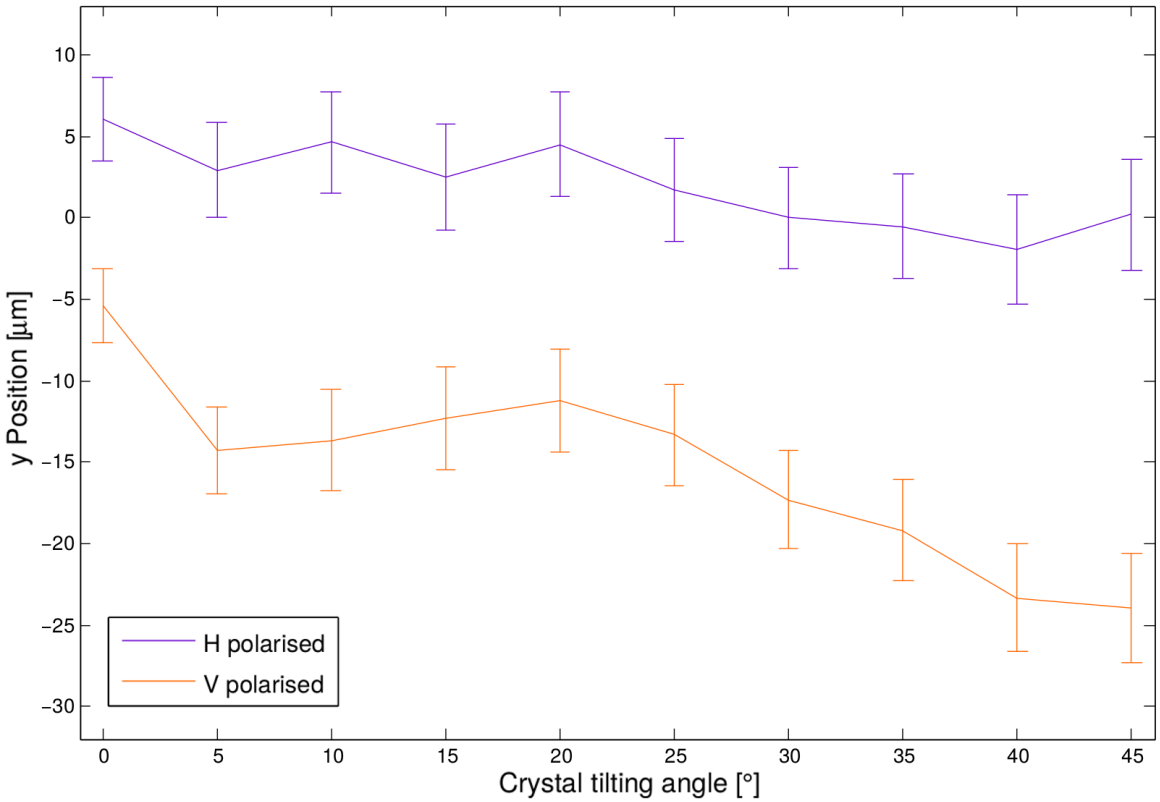

Figure 5.7: Beam stability in y direction in test arm. The height position changes within a range of several μm.

used for the interference experiment, which is depicted in Fig. 5.9 in close-up. Because the polariser is only rotated about a few degrees to balance the intensities within one measurement series, the deviations are limited to a few μm.

Due to these spatial instabilities the overlap of the two arms is automatically as well as manually adjusted for a given setting of crystal and polarization angles in the course of the experiment.

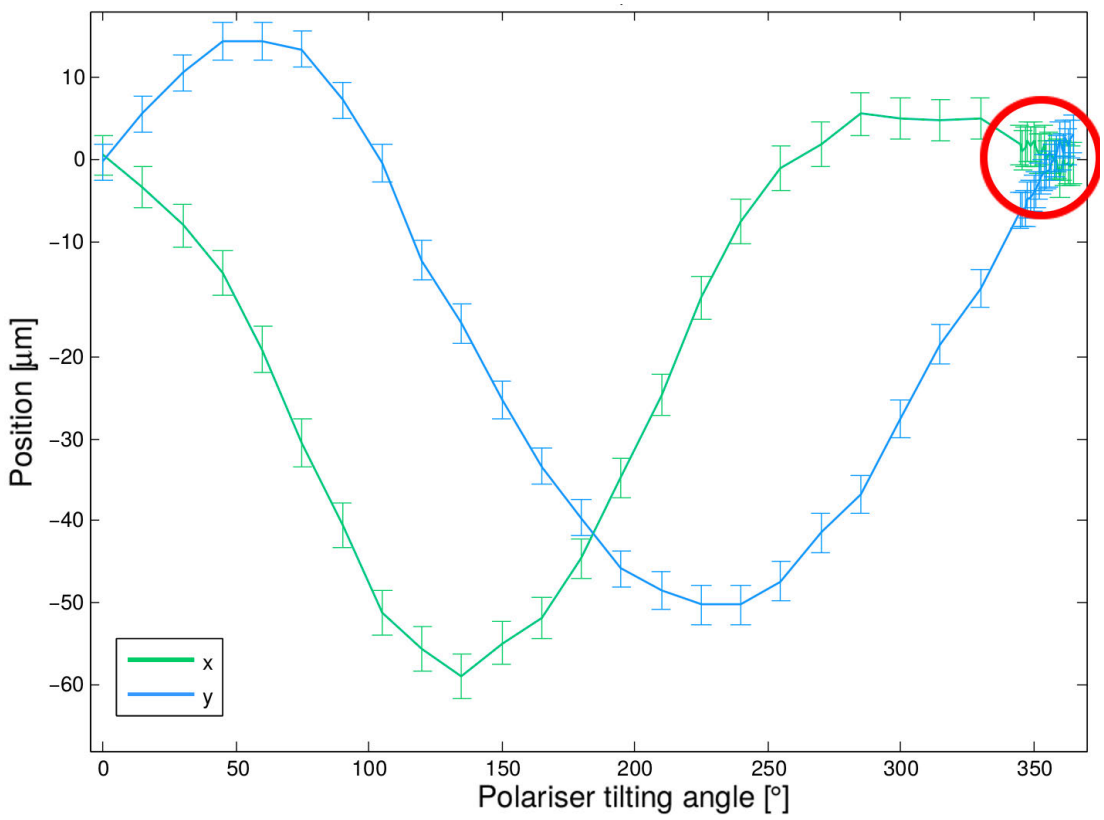

Figure 5.8: Shown is the change of the beam position in x and y direction as the angle of the motorized polariser in the reference arm is varied over a full rotation.

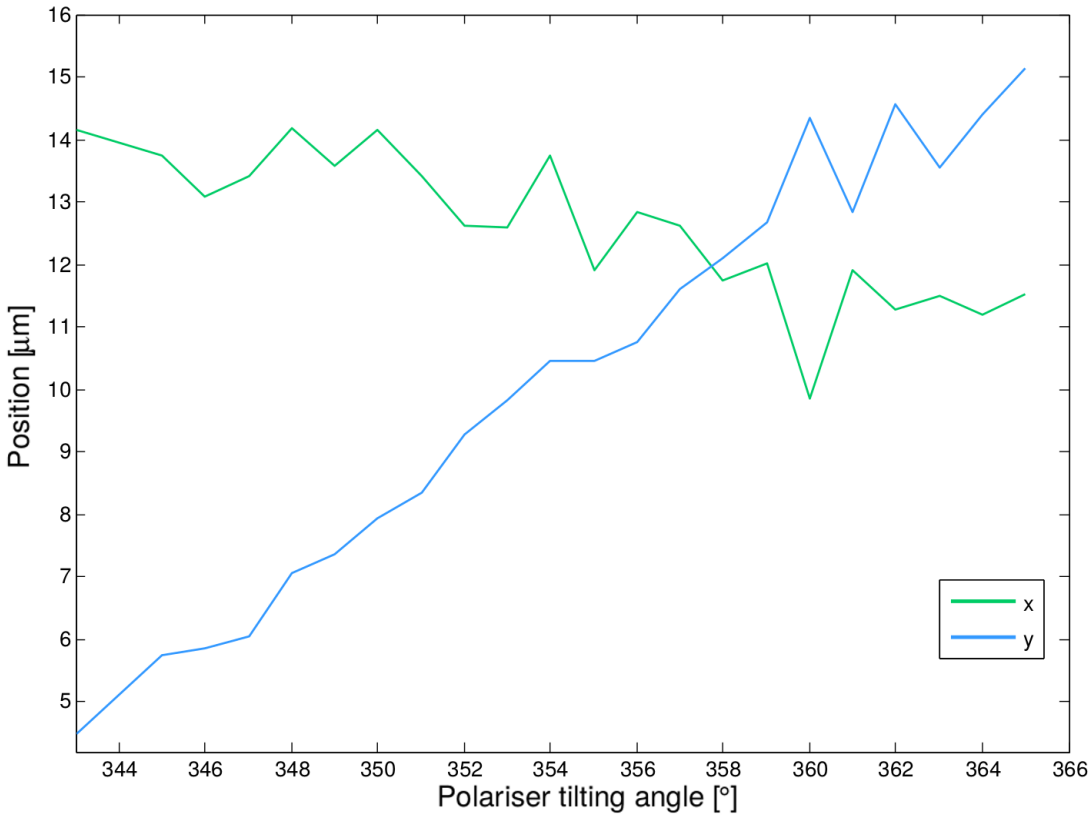

Figure 5.9: The change of the beam position in x and y direction as the angle of the motorized polariser in the reference arm is varied over the relevant range for interference experiment. The latter corresponds to the encircled part from Fig. 5.8

5.2.2 Determination of the tilting angles of the crystal

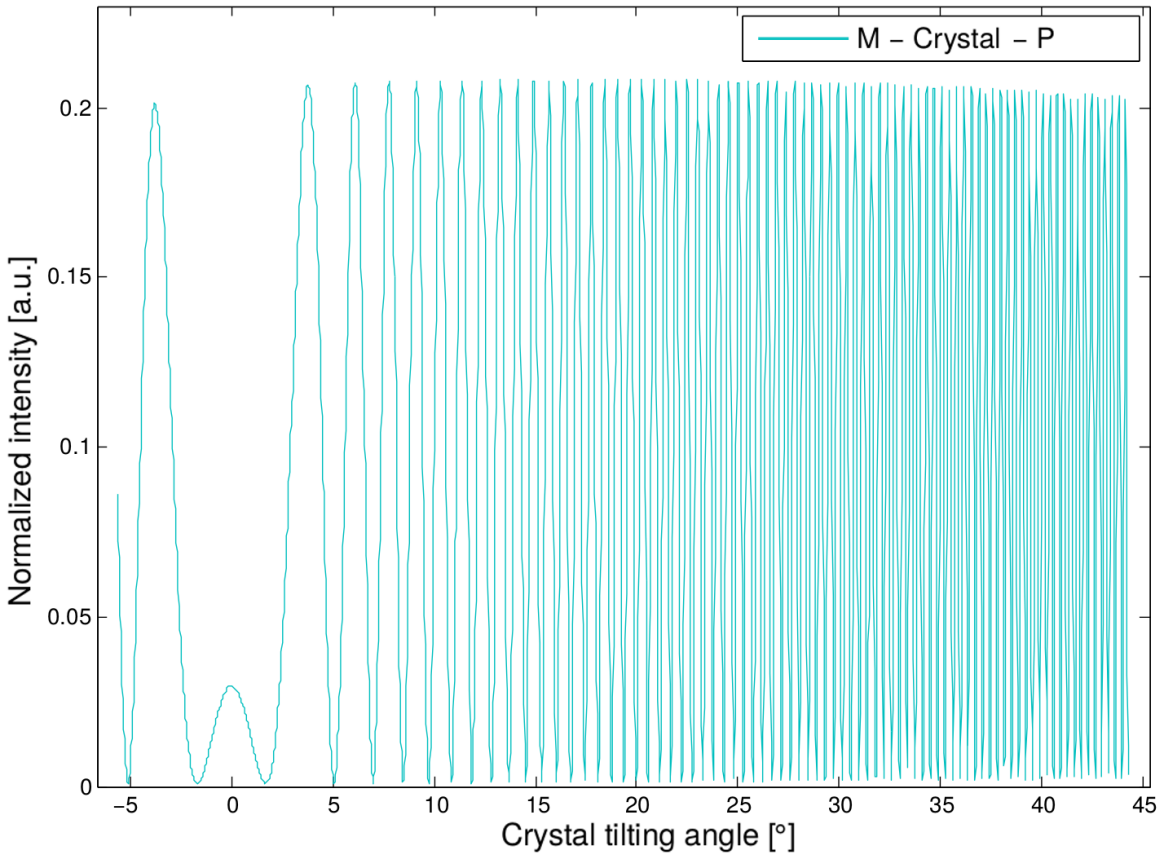

Figure 5.10: To determine the tilting angles, where the polarization stays equal, the crystal is placed between a M- and a P-polariser. At the angles where the intensity is minimal the polarization is maintained. The latter are used as starting points for the automatized optimization in the interference experiment

In addition to the spatial separation of the beam, the birefringent crystal in the test arm induces a relative phase $\Delta\varphi$ between the horizontally polarized ordinary and the vertically polarized extraordinary beam, which is unwanted at this place. The two beam components propagate with different phase velocities according to the different refractive indices. For perpendicular beam incidence the phase mismatch is given by Eq. (2.46). The phase shift is progressively modulated along the crystal thickness d, which is much greater than the wavelength. Upon tilting of the crystal the effective optical path length increases differently for each beam component and therefore the phase shift changes. For the experiment it is necessary to determine these rotation angles, where $\Delta\varphi$ is an integer multiple of 2π in the beam path behind the crystal, such that the overall polarization is effectively preserved.

To this end the intensity is recorded with the preselection M-polarized and the postselection P-polarized, as described in section 4.1.3. Fig. 5.10 shows the change of transmitted

intensity due to the change in polarization upon crystal tilting. With increasing tilting angle the change of the optical path length difference becomes greater, such that the phase shift is modulated more quickly. Selected minima of this graph serve as starting angles for the automatic optimization of the interference experiment.

5.2.3 Mechanical stability of crystal motor settings

The utilized motors exhibit mechanical instabilities at specific motor positions. The crys-

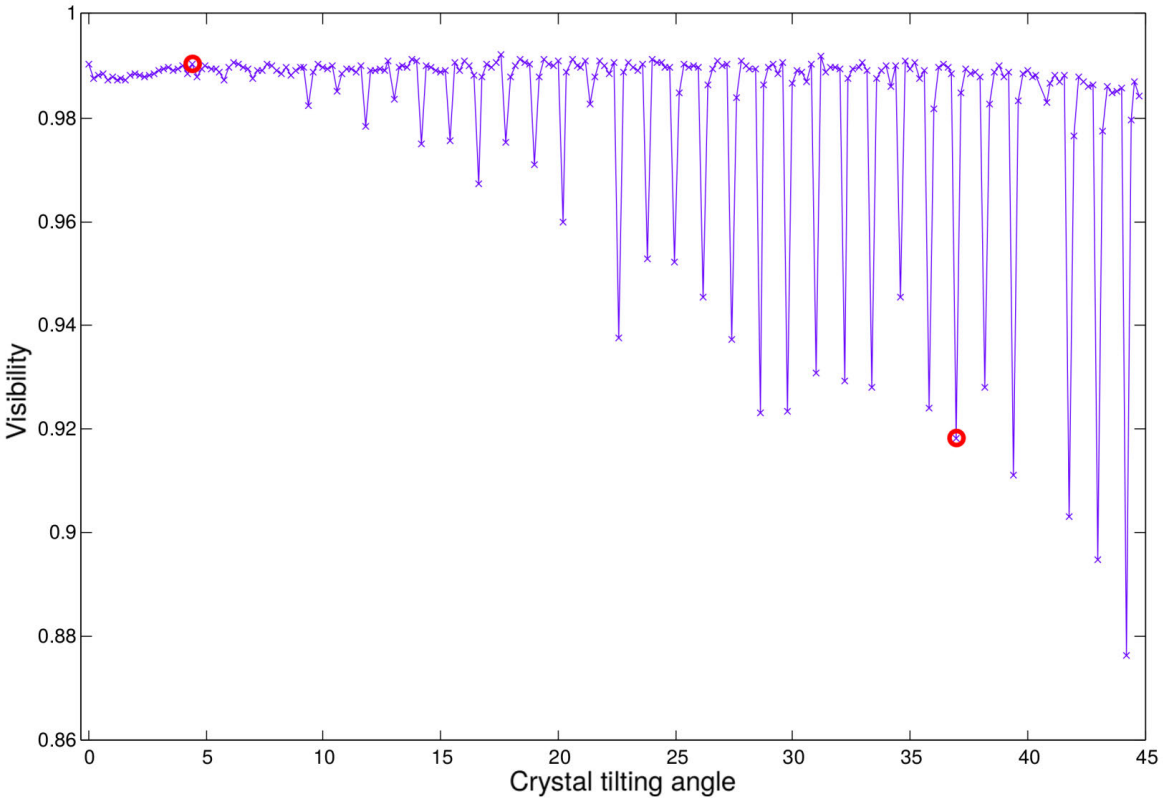

Figure 5.11: Reference visibility measurement in angle steps of 0.2° with H-polarization as preselection to study unstable motor settings. The spatial overlap was not optimized for simplicity. Rather large deviations occur every 1.2°, which tend to increase for larger tilting angles. The intensity modulation of the encircled visibility values will be exemplarily depicted in Fig. 5.12 and Fig. 5.13.

tal is the component most sensitive to these vibrations, which becomes apparent in the distorted interference modulation at such motor settings. To determine the occurrence of such vibrations and their influence on the visibility, the measurement protocol (see section 4.2) is performed with the preselection polariser oriented along H instead of P. This way there is only one ordinarily refracted beam and one does not have to account for the phase shift, which alters the polarization as discussed above. Therefore no further angle optimiz-

ing is needed, while other parameters are automatically optimized as usual. The manual adjustments are omitted for simplicity.

The resulting graph is shown in Fig. 5.11, where the visibility is recorded in angle steps of 0.2°. Most of the data points are approximately constant, as expected, and form a rather stable line across the tilting range. Deviations, whose magnitude increases with increasing tilting angle, occur every 1.2°. The reason for this increased deviation is that vibrations cause larger optical path variations in the tilted configuration, which results in greater distortion of the interference property. Fig. 5.12 shows the intensity variation over time for an exemplary data point from Fig. 5.11 obtained for an angle of 37°, where the visibility is lowered. For comparison, Fig. 5.13 shows the intensity modulation corresponding to a good angle of 4.4° resulting in high visibility.

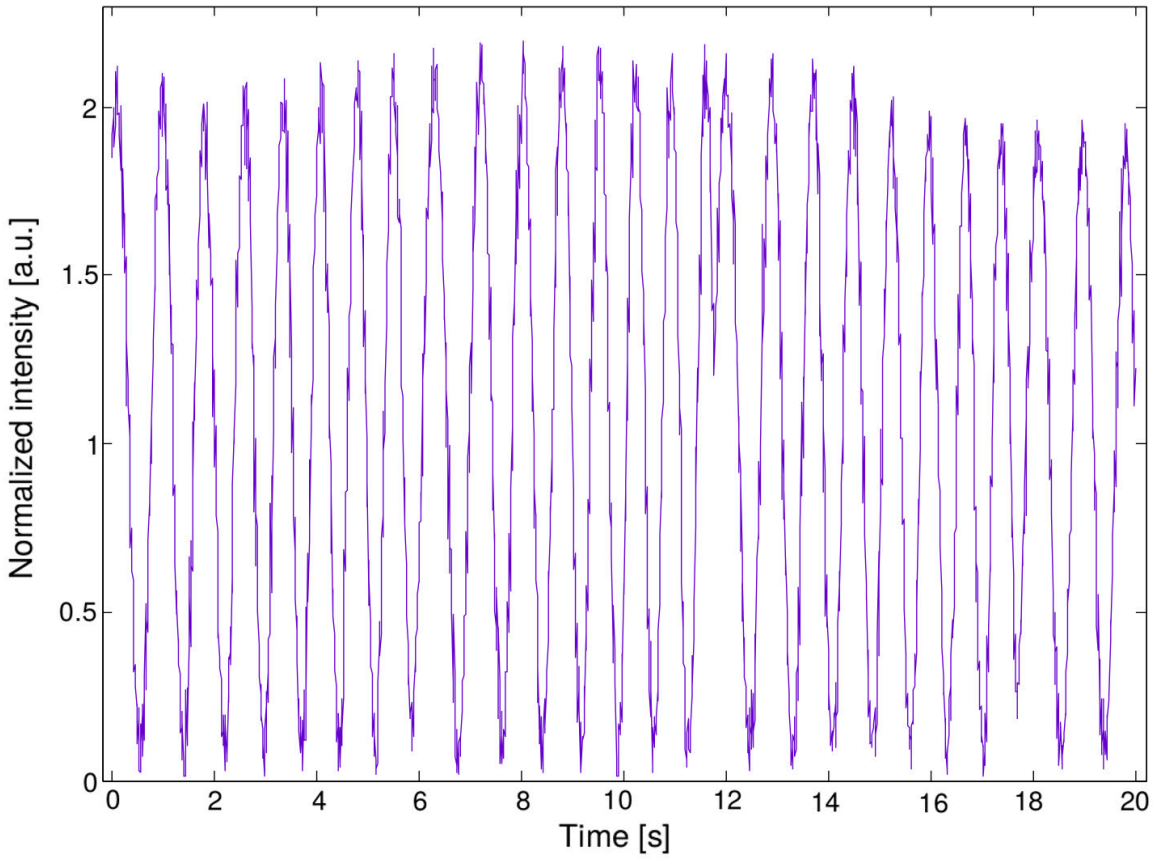

Figure 5.12: The interference pattern is distorted at unstable motor settings. Exemplarily shown is the intensity signal corresponding to the data set from the visibility graph of Fig. 5.11 at an angle of 37°. The resulting interference pattern is unreliable and the visibility decreases. The effect becomes larger with larger tilting angles.

Thus, the useful angle settings are limited by both the condition of maintaining the

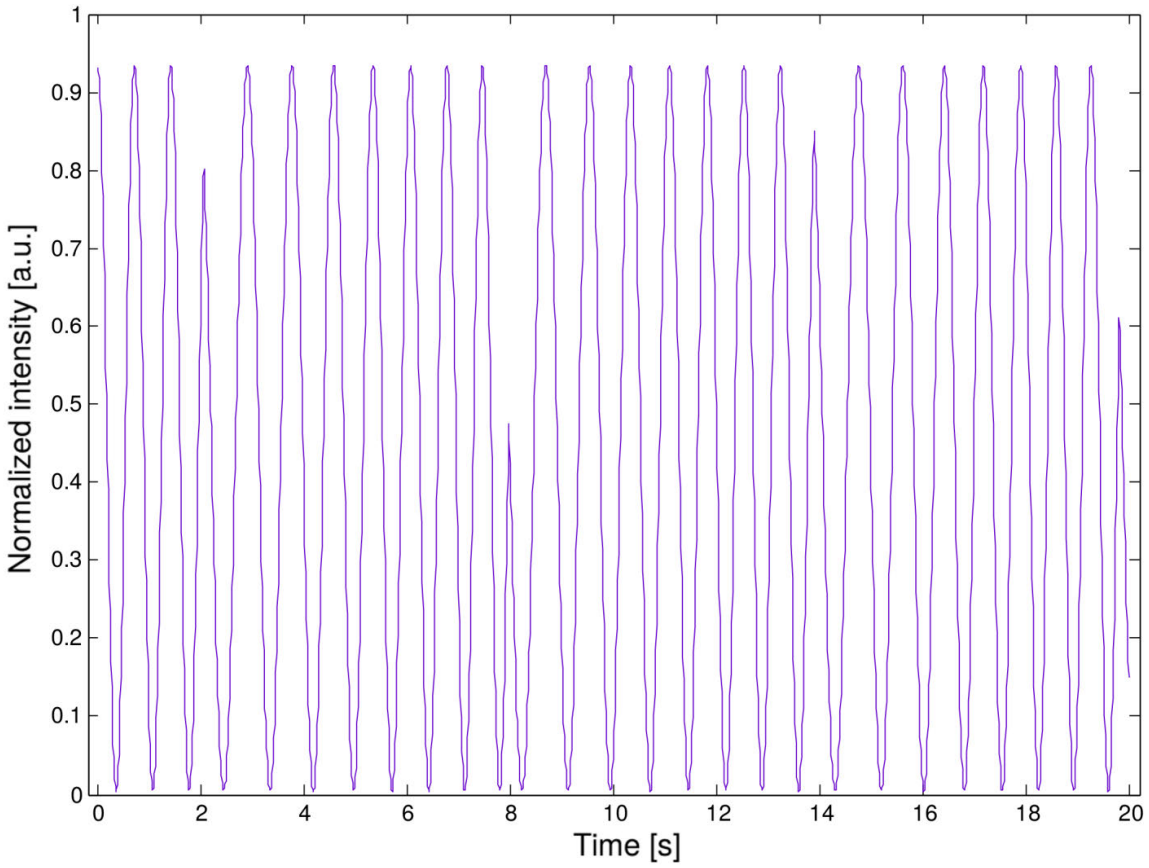

Figure 5.13: Exemplarily shown is the intensity modulation corresponding to the data set from the visibility graph of Fig. 5.11 at an angle of 4.4°. This represents an angle position, where the polarization of the incoming beam is maintained.

polarization and the condition of mechanical stability of the motor, which has a periodicity of at most 1.2°.

5.2.4 Characterizing the alignment of the optical axis of the crystal

The optical axis of the crystal has to be aligned vertically, i.e. perpendicular to the incident beam. With preselection V-polarized and postselection H-polarized the optical axis is adjusted such that the transmitted power, measured with a power meter, is minimal. The accuracy of the performed adjustment procedure was limited, as can be seen from the fact that for varying tilting angles the power ranges from 14 nW to 22 nW, when the background noise of the power meter is subtracted. The corresponding modulation is depicted in Fig. 5.14, where the y axis is scaled to match the recorded power range. For perfectly calibrated polarisers and optimally aligned optical axis the signal is supposed to stay minimal irrespective of the tilting angle of the crystal. However, the deviation arising

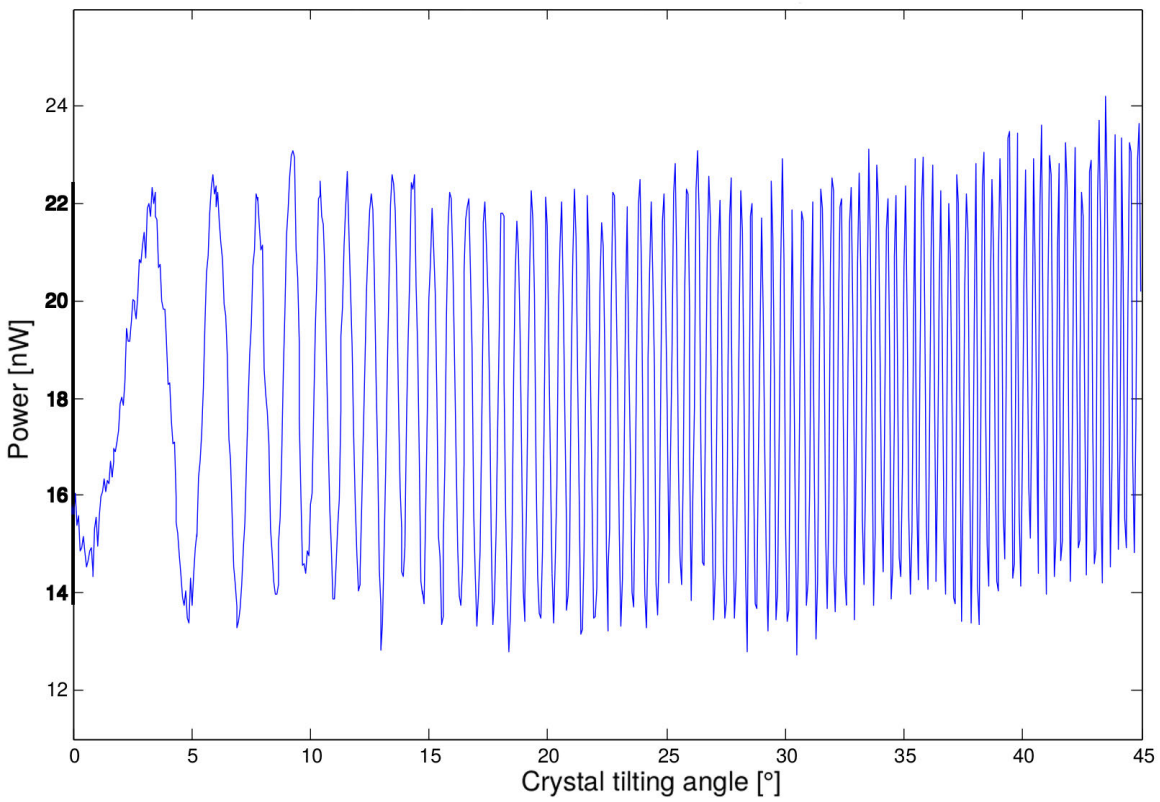

Figure 5.14: Optical axis alignment. The minimal signal measured with the sequence V - Crystal - H ranges from 14 nW to 22 nW, while the maximal signal, obtained with H - Crystal - H, is about four orders of magnitude higher.

from slight mismatches is minor with reference to the recorded power of 235 μW for pre- and postselection horizontally polarized. Due to the extinction ratio of about 1 : 10000 the alignment of the optical axis can be considered precise.

5.2.5 Compensating polarization dependent transmission

Despite the anti-reflection coating of the crystal, the transmission is slightly different for the H- and V-polarized beam depending on its tilting angle. The transmitted signal corresponding to horizontal, T_H, and vertical polarization, T_V, is individually recorded in the test arm starting from an initially plus-polarized beam. As the optical axis is aligned with respect to the H-V-basis, the horizontally polarized beam is assumed to stay horizontal upon propagation and analogously for the vertical polarization. Fig. 5.15 shows that for angles below 34.5° the transmission for vertical polarization is slightly higher than that for horizontal, while it is reversed for the remaining range. The transmission of the initially plus-polarized beam is depicted for comparison. To ensure equal transmission amplitudes for the interference experiment, i.e., $\sqrt{T_H} = \sqrt{T_V}$, the preselection polariser

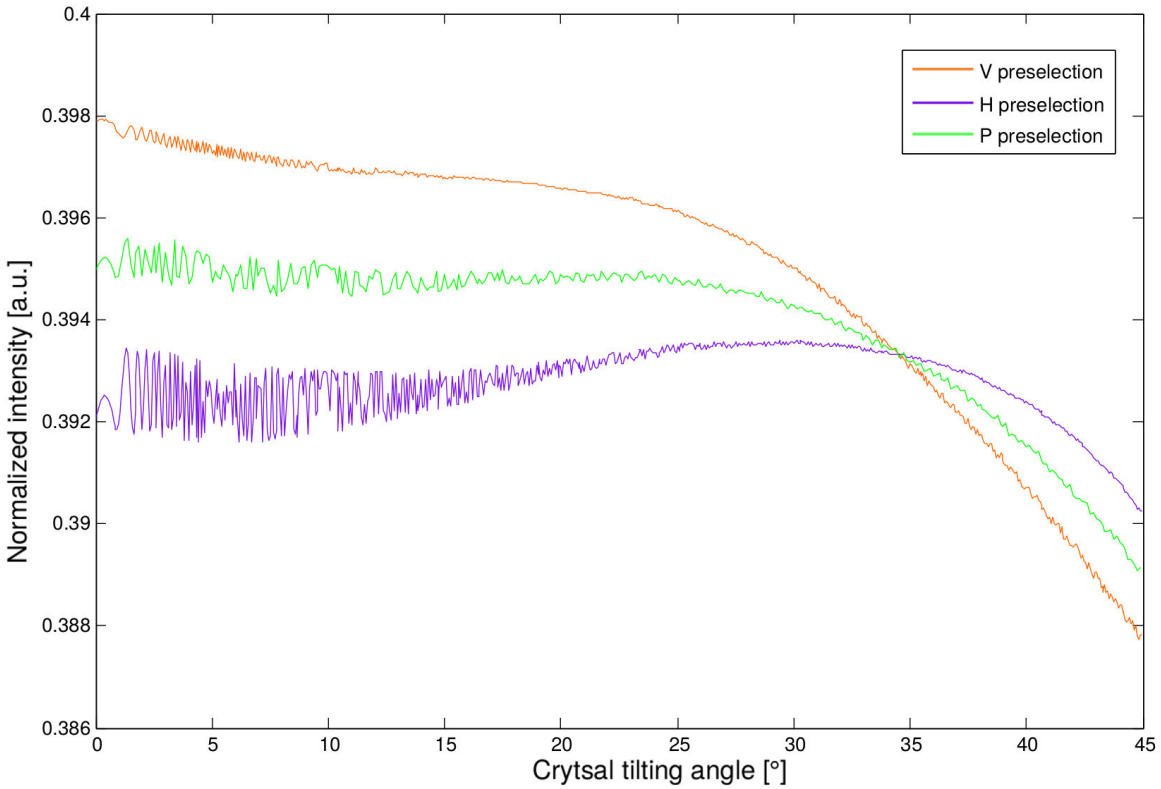

Figure 5.15: Transmission without postselection

has to be set such that it compensates for the difference. Its state may be written as $|P_{\text{var}}\rangle = \cos(\beta)|H\rangle + \sin(\beta)|V\rangle$. As the compensating polarization angle β is dependent on the tilting of the crystal θ, it is fitted as a function of the latter by $\beta = \arctan\left(\frac{\sqrt{T_H(\theta)}}{\sqrt{T_V(\theta)}}\right)$. Although the effect is rather small, the compensation is implemented in the measurement program, which automatically adjusts the preselection according to θ. What can also be seen in Fig. 5.15 is an underlying intensity modulation, which is different for each polarization component. This could be caused by multiple reflections of a fraction of the beam inside the coating of the crystal. Also the overall transmitted intensity decreases.

5.3 Interference experiment

5.3.1 Analysis of visibility optimization within a measurement series

The measurement procedure involves the maximization of the visibility for each crystal setting by optimizing various parameters. The pre-settings for this measurement include tuning the laser current for obtaining a stable output power and a single longitudinal mode, featuring high temporal coherence. Thereby also a certain wavelength is selected. If the current and therefore the wavelength is different from previous measurement settings, it is

crucial to balance the polarizations of both arms accordingly. With a changed wavelength, the phase shift, induced by a birefringent crystal, changes. In particular the ratio of the optical path length difference to the wavelength alters. This affects the polarization change induced in both crystals and since only the one in the test arm is automatically optimized with respect to visibility, while the one in the reference arm is fixed, the polarization in the reference arm has to be manually aligned for that specific wavelength setting. If this is not accounted for, only one nanometer of wavelength change can cause significant decreases in the visibility. As the current is not changed during one measurement run, it is sufficient to balance the polarizations once beforehand. The automatized optimization during a measurement run involves three parameters:

- tuning the crystal angle for a phase-preserving position starting from the input angles
- moving the prism in the test arm to account for the lateral mean displacement of the ordinary and extraordinary beam for better spatial overlap with the reference beam
- balancing the intensity of both arms by setting the motorized polariser in the reference arm

From these degrees of freedom the relative phase induced by the crystal is the most sensitive one. If the angle cannot be optimized to a polarization-maintaining position the visibility drops significantly. This effect is greater for larger angles as the phase relation is more sensitive to deviations there, as seen in Fig 5.10. In this region it becomes more difficult to reach the optimal points of the phase modulation as the minimal angle step size is limited to about 0.01875°. The degrees of freedom, which cannot be optimized automatically include the spatial angle and the height position. However, these are essential for optimal overlap of the two interferometer arms and consequently for the maximal achievable visibility. Therefore both parameters are manually aligned by means of tuning the tip and tilt set screws on the prism mounting in the reference arm and on the first beam splitter to compensate for subtle mismatches, for each angle setting of the crystal as described in 4.2. The angle mismatch, as shown in Fig. 4.2, manifests itself in the characteristic fringes or swiping patterns, which facilitates its detection and therewith its compensation. The mismatch in height position is difficult to observe by eye and therefore difficult to correct. It does not stay constant during the measurement run as the position offsets due to the mounting imbalance of both motorized polarisers and that of the crystal in the test arm are subject to to change in each measurement setting. Likewise, the moving prisms could alter the position offset if they are mounted slightly oblique. The combination of those factors results in a changing spatial offset, which is hardly traceable with the used experimental equipment.

5.3.2 Scaling behaviour

An exemplary measurement series is depicted in Fig. 5.16, where the visibility is recorded for five different values of interaction strength. The latter is given as $\frac{g\epsilon}{\Delta Q_0}$, which translates from the crystal tilting angle θ via the relations 2.43 and 2.44 and from $W_0 = 2\Delta Q_0$.

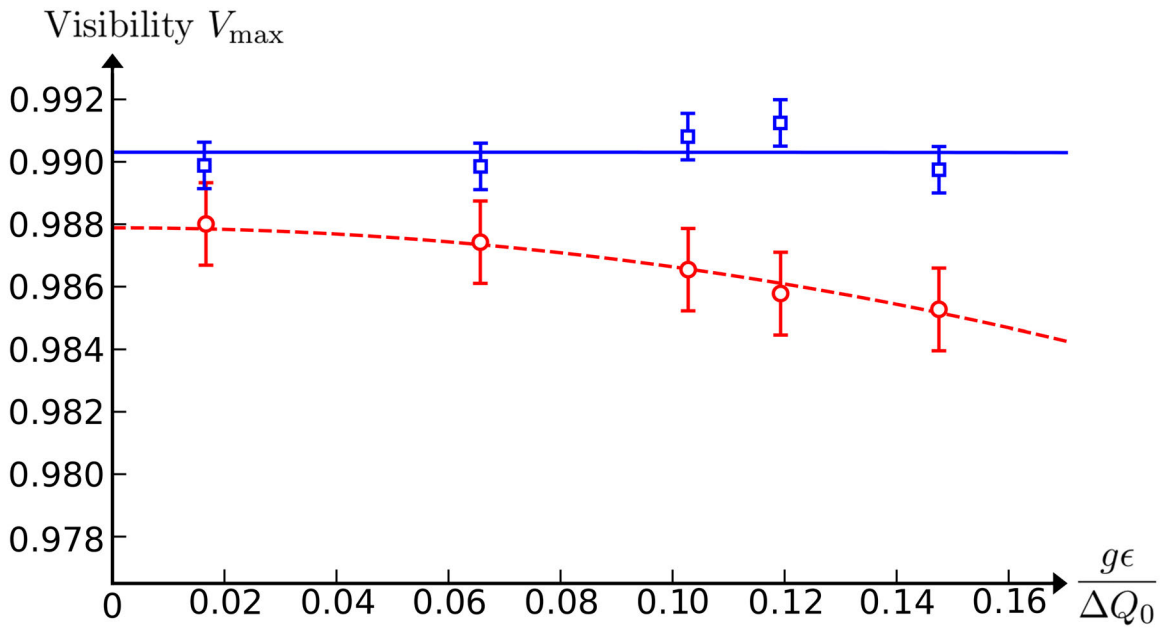

Figure 5.16: Experimental scaling behaviour in terms of visibility

Each data point is measured ten times after a separate automatic fine-tuning optimization to reduce the error caused by the optimization procedure. The blue data points correspond to visibility values obtained for the weak value setting, while the red ones refer to the visibility values in the expectation value setting. i.e. without postselection. The former show a rather stable visibility over the measured range of interaction strength, while the latter decrease more quickly, as expected. If all involved degrees of freedom are perfectly optimized resulting in ideal interference, the initial visibility would be 100% for both cases. This includes the polarization, the intensity, the temporal and spatial properties. Both data sets, however, do not start at 1 due to various imperfections, which are encountered in a real experiment. To fit each of them to the theoretical scaling function $D_A = \arccos(V_{\max})$ these systematic errors are modelled by angle offsets η_1 and η_2, which enter the Bures angle. Due to the high dimensionality of the overall Hilbert space it is very unlikely that these offsets are collinear to the intended scaling direction. Therefore we assume them to be orthogonal. With the deviation angle η and the Bures angle, henceforth called $D_{\mathrm{A,th}}$, being small, the following approximation is valid:

$$\tilde{D}_A = \sqrt{\sin^2(\eta) + \sin^2(D_{\mathrm{A,th}})} \approx \sqrt{\eta^2 + D_{\mathrm{A,th}}^2} \tag{5.3}$$

Therefore the modified expressions, capable of taking into account real experimental conditions, are formulated as

$$\tilde{D}_A\left(|\phi_e\rangle, |\phi_w\rangle\right) \approx \sqrt{\eta_1^2 + \left(\frac{\epsilon^2 g^2}{4\sqrt{2}(\Delta Q_0)^2}\right)^2}, \tag{5.4}$$

for the Bures angle between the states associated with the weak value and the eigenvalue, and as

$$\tilde{D}_A\left(|\phi_e\rangle, \sigma_{ex}\right) \approx \sqrt{\eta_2^2 + \left(\frac{\epsilon g}{2\Delta Q_0}\right)^2}. \tag{5.5}$$

for the Bures angle between the states associated with the expectation value and the eigenvalue. The offset angle η is visualized in Fig. 5.17. For small interaction strength

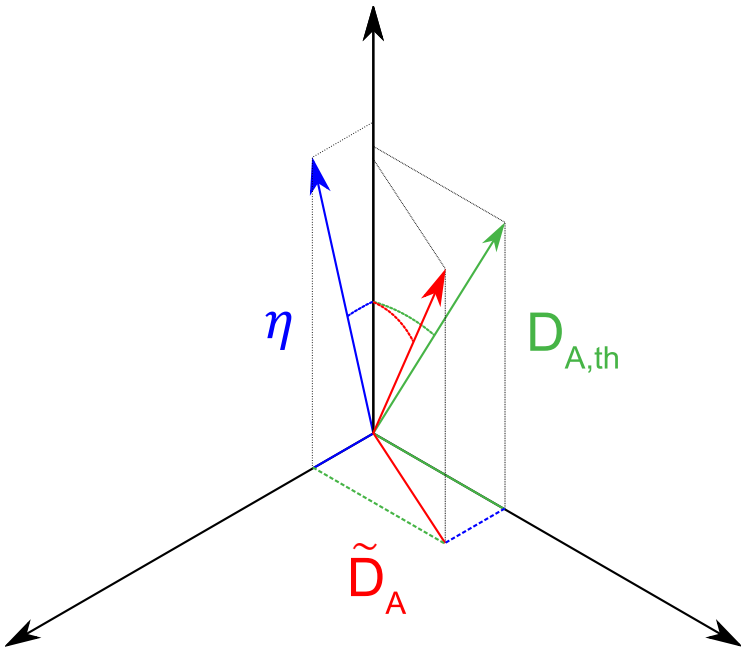

Figure 5.17: Experimental Bures angle. The observed angle in the experiment involves an offset angle η, which is assumed orthogonal to the intended angle $D_{\mathrm{A,th}}$. As the description uses a metric space, the angles can be understood as distances. Therefore the experimental Bures angle can be modelled by use of Pythagoras's theorem as $\tilde{D}_A \approx \sqrt{\eta^2 + D_{\mathrm{A,th}}^2}$.

the impact of η_1 and η_2 is comparably large, while for increasing strength these modified Bures angle expressions asymptotically converge to the ideal ones. The fact that η_1 and η_2 are not equal arises from the changed initial conditions, i.e. the set-up is slightly different. With the fitted offsets the visibility values in Fig. 5.16 agree well with the expressions 5.4 and 5.5. The same can be seen in Fig. 5.18. The data points of the expectation value case follow the modified Bures angle scaling very well and reside almost exactly on the fit function. In the weak value case the data points are constant to a good approximation, where two of the values at around $0.10\frac{g\epsilon}{\Delta Q_0}$ and $0.12\frac{g\epsilon}{\Delta Q_0}$ even lie below the fitted function. Because the usual experimental conditions are non-ideal, there can be settings during the measurement run, where the optimization of the various parameters is slightly more successful compared to other settings, which could explain these smaller values. The error

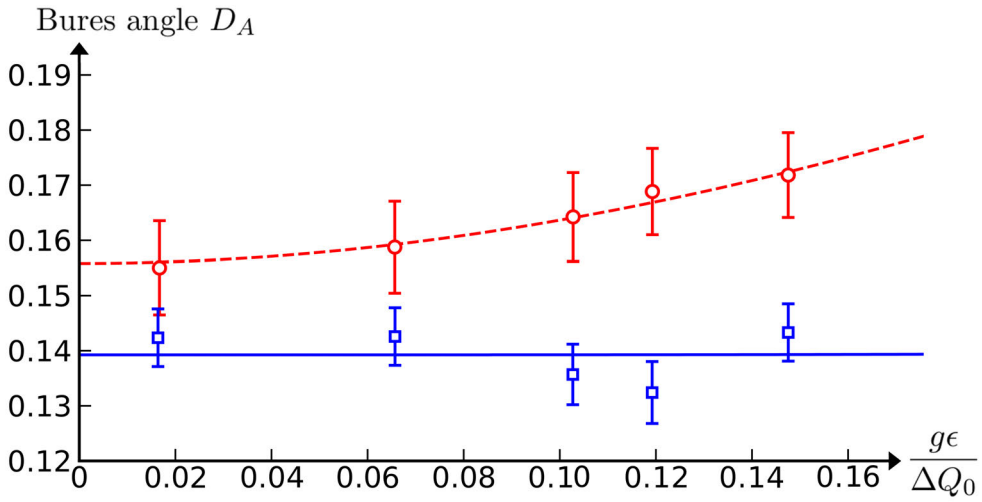

Figure 5.18: Experimental scaling behaviour in terms of Bures angle.

bars have been averaged for weak value and expectation value, respectively. They indicate the reproducibility of the automatic optimization.

5.3.3 Reproducibility and sources of error

As the intended effect is tiny in the available range of interaction strength, small errors have a great impact on the resulting measurement. The visibility is found to be most sensitive to the parameters of spatial overlap and polarization-maintaining crystal angles. The latter is optimized automatically and therefore the optimization is comparable for different measurement settings. However, due to the finite step size of the motor the visibility depends on how well the polarization maintaining angle position coincides with the angle accessible by the motor. A further restricting factor regarding the crystal angles is that every 1.2° the motor exhibits an unstable position such that the angle cannot be used for the measurement or equivalently that the corresponding measurement has to be discarded in the data analysis. Thus, the useful angle positions are very limited. The manual alignment for every data point is hardly reproducible in an exact manner because there is no reference spatial setting to compare with. In particular the precision of the alignment of the height position is limited, as this is accomplished by walking the beam via the first beam splitter and the prism in the reference arm. Other than in the case of an angle mismatch the interference pattern observed on the camera screen is not considerably affected by a small deviation and is therefore difficult to correct. Therefore tiny unknown deviations make different measurement series difficult to be exactly reproduced.

5.4 Comparison with theory

As the range of the interaction strength is constrained by the properties of the crystal, i.e., its thickness and its birefringence, as well as by the available width of the laser beam, pre-set by the lens of the fibre collimator, the experiment can only cover the first part of the theoretical graph. The successful experimental implementation is based on the premise of maximizing the visibility for each of the two settings. The resulting scaling behaviours are comparable if all degrees of freedom, relevant for the visibility, are optimized. Then the difference in the scaling behaviour results solely from the added postselection. In our case, small initial offsets η_1 and η_2 have to be taken into account for both settings. The Bures angle expressions are reasonably modified according to Eq. 5.3 to capture realistic conditions. The former converge to the theoretical ones for larger interaction strengths. Therefore the range, where the expectation value case evolves linearly and the weak value case scales quadratically cannot be seen in the experiment directly. Instead, the overall error has to be considered first. Nonetheless, in the range available in the experimental set-up the difference in the scaling behaviour is clearly visibly despite the offsets and despite the predicted difference being rather small in that range. The data follows to a good approximation the expressions for $\tilde{D}_A\left(|\phi_e\rangle, |\phi_w\rangle\right)$ and $\tilde{D}_A\left(|\phi_e\rangle, \sigma_{ex}\right)$, where in both cases only one parameter is added with respect to Eq. 3.34 and Eq. 3.35.

6 Conclusion and outlook

The aim of this thesis was to experimentally demonstrate the scaling behaviour of the visibility as a function of the interaction strength. Therefore an interferometer was set up and refined to meet the requirements needed to enable the comparison to the theoretical expressions in terms of the Bures angle. In summary, it can be said that the difference in the scaling behaviour between the Bures angle of the states associated with a weak value and an eigenvalue and the Bures angle of the states associated with an expectation value and an eigenvalue was clearly verified. Despite of imperfect experimental conditions it was possible to resolve the respective theoretical scaling functions with the available experimental equipment. The fact that these imperfections are kept small, allowed to model an expression for the Bures angle, which is modified by only one parameter in each case to comply with the experimental conditions. The obtained results agree well with these slightly modified Bures angle expressions. With the investigation of the scaling behaviours presented in this thesis, it was possible to make a contribution towards a comprehensive understanding of the physical meaning of the weak value and therewith to unravel a further puzzle in the framework. To improve the reproducibility of optimizing the visibility in the set-up, which is needed for the successful measurement, future measurements could employ position sensing detectors, which allow for a better comparability of the spatial alignment between different measurement settings. The spatial degree of freedom of the two interfering laser beams is a crucial parameter in the optimization of the visibility in the set-up and was one of the precision limiting factors. Another approach of experimental realization would be to implement an anomalous weak value instead of the specific case, when the weak value is zero. In this case the weak value exceeds the range of eigenvalues of the observable of interest. Then the comparison with expectation value and eigenvalue is effectively possible by creating respective virtual quantities. Beyond this question, the set-up can for instance be used to study and compare different realizations of the weak value, which we leave as a prospect.

Surely, this exceptionally fascinating and challenging topic provides an immense research potential which is worth studying. The understanding of the concept of the weak value is far from being complete. Therefore it seems likely that future investigations will lead to the discovery of so far unknown properties and new effects.

Bibliography

[1] *Chapter 11 - laser cavity modes.*

[2] *Tutorial polarization optics.*

[3] Agha, S. and D. Minkin: *Understanding "walking the beam"*, 2007.

[4] Aharonov, Y., D. Albert, and L. Vaidman: *How the result of a measurement of a component of the spin of a spin-1/2 particle can turn out to be 100.* Physical Review Letters, 60(14):1351–1354, 1988.

[5] Aharonov, Y. and A. Botero: *Quantum averages of weak values.* Physical Review A, 72(5):1–12, 2005.

[6] Aharonov, Y., E. Cohen, E. Gruss, and T. Landsberger: *Measurement and collapse within the two-state vector formalism.* Quantum Studies: Mathematics and Foundations, 1(1):133–146, 2014.

[7] Aharonov, Y., S. Popescu, and J. Tollaksen: *A time-symmetric formulation of quantum mechanics.* American Institute of Physics, Physics Today, 63(11):27–32, 2010.

[8] Aharonov, Y. and D. Rohrlich: *Quantum Paradoxes: Quantum Theory for the Perplexed.* Wiley-VCH Verlag GmbH & Co. KgaA, Weinheim, Germany, 2005.

[9] Aharonov, Y. and J. Tollaksen: *New insights on time-symmetry in quantum mechanics.* arxiv, 2007.

[10] Aharonov, Y. and L. Vaidman: *"The Two-State Vector Formalism: an Updated Review" in "Time in Quantum Mechanics".* Springer-Verlag Berlin Heidelberg, Germany, 2008.

[11] Dixon, P.B., D.J. Starling, A.N. Jordan, and J.C. Howell: *Ultrasensitive beam deflection measurement via interferometric weak value amplification.* Physical Review Letters, 102(17), 2009.

[12] Dziewior, J.: *The concept of weak values.* Master's thesis, Ludwig-Maximilians-Universität, Munich, 2016.

[13] Foctek Photonics, I.: *Birefringent crystals - yvo4*.

[14] Gillen, G.D., K. Gillen, and S. Guha: *Light propagation in linear optical media.* CRC Press, Taylor & Francis Group, Boca Raton, Florida, USA, 2014.

[15] GmbH, R.P.C. and R. Paschotta: *Anamorphic prism pairs.*

[16] GmbH, R.P.C. and R. Paschotta: *Coherence.*

[17] Goggin, M.E., M.P. Almeida, M. Barbieri, B.P. Lanyon, J.L. O'Brien, A.G. White, and G.J. Pryde: *Violation of the leggett-garg inequality with weak measurements of photons.* Proceedings of the National Academy of Sciences, 108(4):1256–1261, 2011.

[18] Griffiths, D.J.: *Introduction to Quantum Mechanics.* Pearson Prentice Hall, New Jersey, USA, 2005, second edition.

[19] Gross, R.: *Die Polarisation von Licht*, 2003.

[20] Hosoya, A. and Y. Shikano: *Strange weak values.* Journal of Physics A: Mathematical and Theoretical, 43(38):1–15, 2010.

[21] Jozsa, R.: *Complex weak values in quantum measurement.* Physical Review A, 76(4):1–3, 2007.

[22] Knips, L.: *Reconstruction and analysis of multi-photon entangled quantum states.* Master's thesis, Ludwig-Maximilians-Universität, Munich, 2013.

[23] Kocsis, S., B. Braverman, S. Ravets, M.J. Stevens, R.P. Mirin, L.K. Shalm, and A.M. Steinberg: *Observing the average trajectories of single photons in a two-slit interferometer.* Science, 332:1170–1173, 2011.

[24] Kofman, A., S. Ashhab, and F. Nori: *Nonperturbative theory of weak pre- and post-selected measurements.* Physics Reports, 520(2):43–133, 2012.

[25] Lee, J. and I. Tsutsui: *Merit of amplification by weak measurement in view of measurement uncertainty.* Quantum Studies: Mathematics and Foundations, 1(1):65–78, 2014.

[26] Lobo, A. and C. Ribeiro: *Weak values and the quantum phase space.* PHYSICAL REVIEW A, 80(1):1–6, 2009.

[27] Ltd, M.L.P.: *moglabs - external cavity diode laser*, 2010.

[28] Lundeen, J., B. Sutherland, A. Patel, C. Stewart, and C. Bamber: *Observation of the spin hall effect of light via weak measurements.* Science, 319, 2008.

[29] Lundeen, J., B. Sutherland, A. Patel, C. Stewart, and C. Bamber: *Direct measurement of the quantum wavefunction.* Nature, 474:188–191, 2011.

[30] Menzel, R.: *Photonics - Linear and Nonlinear Interactions of Laser Light and Matter.* Springer-Verlag Berlin Heidelberg, Germany, 2001.

[31] Nielsen, M.A. and I.L. Chuang: *Quantum Computation and Quantum Infromation.* Cambridge University Press, Cambridge, England, 2000.

[32] Palacios-Laloy, A., F. Mallet, F. Nguyen, P. Bertet, D. Vion, D. Esteve, and A. Korotkov: *Experimental violation of a bell's inequality in time with weak measurement.* Nature Physics, 6:442–447, 2010.

[33] Pan, A.K. and A. Matzkin: *Weak values in nonideal spin measurements: An exact treatment beyond the asymptotic regime.* Physical Review A, 85:1–9, 2012.

[34] Pang, S., T. Brun, S. Wu, and Z.B. Chen: *Amplification limit of weak measurements: a variational approach.* Physical Review A, 90:1–7, 2014.

[35] Piccirillo, B., S. Slussarenko, L. Marrucci, and E. Santamato: *Directly measuring mean and variance of infinite-spectrum observables such as the photon orbital angular momentum.* Nature Communications, 6:1–7, 2015.

[36] Ricci, L., M. Weidemüller, T. Esslinger, A. Hemmerich, C. Zimmermann, V. Vuletic, W. König, and T. Hänsch: *A compact grating-stabilized diode laser system for atomic physics.* Optics Communications, 117:541–549, 1995.

[37] Ritchie, N., J. Story, and R. Hulet: *Realization of a measurement of a "weak value".* Physical Review Letters, 66(9):1107–1110, 1991.

[38] Sakurai, J.J. and J. Napolitano: *Modern Quantum Mechanics.* Pearson Education, Inc., San Francisco, USA, 2011, second edition.

[39] Saleh, B.E.A. and M.C. Teich: *Fundamentals of Photonics.* Wiley & Sons, Inc., Hoboken, New Jersey, USA, 2007.

[40] Saliba, S.D. and R.E. Scholten: *Linewidths below 100khz with external cavity diode lasers.* Optical Society of America, Applied Optics, 48(36):6961–6966, 2009.

[41] S.r.l., D.T.A.: *Diode laser tutorial - a comprehensive technical explanation of laser technology.*

[42] Svensson, B.: *Pedagogical review of quantum measurement theory with an emphasis on weak measurements.* Quanta, 2:18–49, 2013.

[43] Tamir, B. and E. Cohen: *Introduction to weak measurements and weak values.* Quanta, 2(1):7–17, 2013.

[44] TEACHSPIN, I. and K. Libbrecht: *Diode laser spectroscopy "spectroscopy and much more, using modern optics"*, 2009.

[45] Tollaksen, J.: *Robust weak measurements on finite samples.* Journal of Physics: Conference Series, 70:1–20, 2007.

[46] Torres, J. and L.J. Salazar-Serrano: *Weak value amplification: a view from quantum estimation theory that highlights what it is and what isn't.* Scientific Reports, 6:1–11, 2016.

[47] Vaidman, L., A. Ben-Israel, J. Dziewior, L. Knips, M. Weißl, J. Meinecke, C. Schwemmer, R. Ber, and H. Weinfurter: *Weak value beyond conditional expectation value of the pointer readings*, 2016.

[48] Williams, N. and A. Jordan: *Weak values and the leggett-garg inequality in solid-state qubits.* Physical Review Letters, 100(2), 2008.

[49] Wu, S. and Y. Li: *Weak measurements beyond the Aharonov-Albert-Vaidman formalism.* Physical Review A, 83:1–5, 2011.

[50] Wu, S. and K. Mølmer: *Weak measurements with a qubit meter.* Physical Letters A, 374(1):34–39, 2009.

[51] Zinth, W. und U. Zinth: *Optik - Lichtstrahlen - Wellen - Photonen.* Oldenbourg Wissenschaftsverlag GmbH, Munich, Germany, 2013, fourth edition.

Selbstständigkeitserklärung

Hiermit erkläre ich, die vorliegende Arbeit selbstständig verfasst zu haben und keine anderen als die in der Arbeit angegebenen Quellen und Hilfsmittel benutzt zu haben.

München, December 21, 2016

Ort, Datum

Unterschrift